1-1-2016

Computational Modeling Of High-Performance Nickel-Metal Hydride Battery Materials

Diana Felicia Wong
Wayne State University,

COMPUTATIONAL MODELING OF HIGH-PERFORMANCE NICKEL-METAL HYDRIDE BATTERY MATERIALS

by

DIANA F. WONG

DISSERTATION

Submitted to the Graduate School

of Wayne State University,

Detroit, Michigan

in partial fulfillment of the requirements

for the degree of

DOCTOR OF PHILOSOPHY

2016

MAJOR: CHEMICAL ENGINEERING

Approved By:

_____

Advisor Date

_____

Advisor Date

_____

_____

_____

DEDICATION

To my family and friends and their unconditional love and support.

ACKNOWLEDGMENTS

I would like to thank my advisors Dr. K.Y. Simon Ng and Dr. Kwo-Hsiung Young for their steadfast encouragement and support of not only this work, but of my academic and professional career. They have provided valuable insights and perspectives in tackling problems large and small, always reminding me to keep the big picture in mind.

I am grateful to Dr. Eranda Nikolla, Dr. Da Deng, and Dr. Mark Cheng for serving on my committee, contributing their time and expertise to help mold and strengthen the work presented in this dissertation. I would like to thank Mr. Michael Fetcenko, Vice President and Managing Director of BASF Battery Materials – Ovonic, for his kind support and encouragement towards advancing my academic and professional training. I am also grateful to Dr. Baoquan Huang, Dr. Jean Nei, Dr. Benjamin Chao, Dr. Benjamin Reichman, Dr. Lixin Wang, Mr. Taihei Ouchi, Ms. Su Cronogue, Dr. Tiejun Meng, Dr. Shuli Yan, Dr. Negar Mosavati, Mr. William Mays, Ms. Rose Bertolini, Mr. James Strebe, Ms. Sherry Hu, Mr. David Pawlik, Mr. Ryan Blankenship, Mr. Alan Chan and the rest of my colleagues at BASF Battery Materials – Ovonic and Wayne State University. They've generously shared with me their time, support, expertise, and guidance.

I would also like to thank my family for their unconditional support and understanding. My brother, Gary S. Wong, also provided a sounding ear and valuable advice for everything programming related.

Thank you.

TABLE OF CONTENTS

LIST OF TABLES

LIST OF FIGURES

CHAPTER 1. INTRODUCTION

With 10 million hybrid electric vehicles on the road worldwide powered primarily by nickel-metal hydride (NiMH) batteries, research into this battery chemistry will improve the hybrid vehicle driving experience, extending electric-only driving ranges while reducing emissions and using less gasoline. While the biggest limiting factor in the NiMH battery is its aqueous-based electrolyte – restricting the operating voltage window to ~1.2V per cell – once that voltage cap is lifted, the power and energy storage capacity of the nickel-metal hydride battery lies in the active materials' abilities to exchange protons and electrons as well as to conduct them. New research into lifting the voltage cap will go a long way into revolutionizing nickel-metal hydride batteries, and the fundamental understanding of its battery materials will improve both present and future technologies.

The transfer, storage and transport of protons and electrons depend strongly on the structural and electrical features of the active material, including multiple phases, defects, and structural and compositional disorder. Of interest on the anode side is the class of C14 and C15 AB_2 Laves phase alloys, which share similar crystallographic structures, but differ only in its stacking. Nickel hydroxide active material for the cathode is known for its layered structure, which is intrinsically insulative; but this material works in a battery due to the defects and stacking faults within the crystal structure. The contributions of such subtle defects and the difference with the bulk structure can be difficult to discern experimentally. *Ab initio* calculations such as the ones based on density functional theory have been used to calculate properties and confirm ground state phase stability in AB_2 Laves phase alloys. The crystal structure, band gap, and band structure of nickel hydroxide, the positive electrode active material, has been calculated and verified experimentally. X-ray diffraction patterns offer subtle but

valuable markers that can be correlated to structure and electrochemical performance. Electrochemical impedance spectroscopy coupled with equivalent circuit modeling probes the interactions that occur at the surface interfaces, yielding valuable electrical properties and electrochemical kinetics information. This study of defects, structural properties, and surface interfaces in battery materials can identify trends that contribute to higher capacity and higher power materials using computational and modeling methods. Understanding the trends provides better insight into how structural properties affect electrochemical processes and will help guide the design for better optimized battery materials.

1.1 Significance of Research

Much work has been invested in the anode and cathode sides of the nickel-metal hydride battery field in order to better understand and to better design battery materials. There are a number of areas in the literature review where questions and exceptions arise pertaining to the structure of materials and the electrochemical processes that the structures influence. Computational methods for battery material applications have been developed in order to screen for materials, but they are not without their challenges [1, 2]. The length scales involved with calculating quantum properties and relating them to measurable battery performance parameters, such as specific capacity or power density, requires a fundamental understanding of electrochemical systems as well as the theory and limitations that go with the computational code. On the other hand, computational techniques also allow insights into materials that may not be practical or possible to prepare or measure experimentally – especially those of highly-disordered, defected, and multi-phase materials. It is with this spirit in mind that we have four major research topics, covered by Chapters 4-6, that implement various computational and

modeling techniques to better understand the fundamentals of anodes and cathode materials for high-performance nickel-metal hydride batteries.

1. To use first-principle DFT calculations to model the stable C14/C15 ground state structures of AB_2 metal hydride alloys first calculated by semi-empirical methods. We determine the electronic contributions to energy correlate to the semi-empirical methods, but vibrational contributions play a larger role at the C14/C15 energy thresholds.

2. To use first-principle DFT calculations to model the initial lattice expansions of AB_5 and AB_2 metal hydride anode materials upon hydrogenation, which are correlated to capacity degradation performance over time through pressure-concentration-temperature isotherm hysteresis measurements, and play a role in the alloy pulverization pathway.

3. To use DIFFaX simulation to model and track the evolution of stacking faults in substituted nickel hydroxide spherical powders with respect to precipitation time and additives while maintaining temperature, flow rate and pH conditions. The peak broadening of the (101) peak is strongly correlated to electrochemical utilization in nickel hydroxide materials, and stacking faults directly interrupt the (101) plane periodicity. We determine which types of stacking faults have a stronger effect on the (101) peak, and the conditions that promote the formation of each type of stacking fault.

4. To use equivalent circuit modeling of electrochemical impedance spectra to understand the nature of the electrochemical reactions occurring on the surface of La- and Nd- doped AB_2 metal hydride alloys, which provide −40°C

performance comparable to the rare-earth-based AB_5 alloys. We determine the catalytic activity versus the surface area contributions from La and Nd to the electrochemical reactions.

CHAPTER 2. BACKGROUND AND THEORY

2.1 Nickel-Metal Hydride Battery

The nickel-metal hydride battery (NiMH) is a rechargeable battery comprising a hydrogen storage alloy-based anode, a nickel hydroxide cathode, and alkaline electrolyte. The battery chemistry is similar to nickel-cadmium batteries, which share the same cathode, and relies on the active materials' ability to exchange protons in order to store electricity.

The following half-reactions describe the redox reactions that occur in the NiMH battery in an alkaline environment:

$$M + H_2O + e^- \leftrightarrow MH + OH^-$$

$$Ni(OH)_2 + OH^- \leftrightarrow NiOOH + H_2O + e^-$$

The forward reactions in the equations describe the charging process. Water splits on the anode (negative electrode) with the applied voltage during charging, and the hydrogen storage alloy absorbs protons from the water and electrons through the current collector from the external charging circuit to form a metal hydride. Hydroxyl ions from the water splitting reaction conduct through the electrolyte to the cathode (positive electrode). The nickel hydroxide cathode oxidizes to nickel oxyhydroxide, providing electrons to the external charging circuit and reforming water. The reverse reactions describe similarly the discharging process. A schematic of both the charging and discharging process is shown in Figure 1.

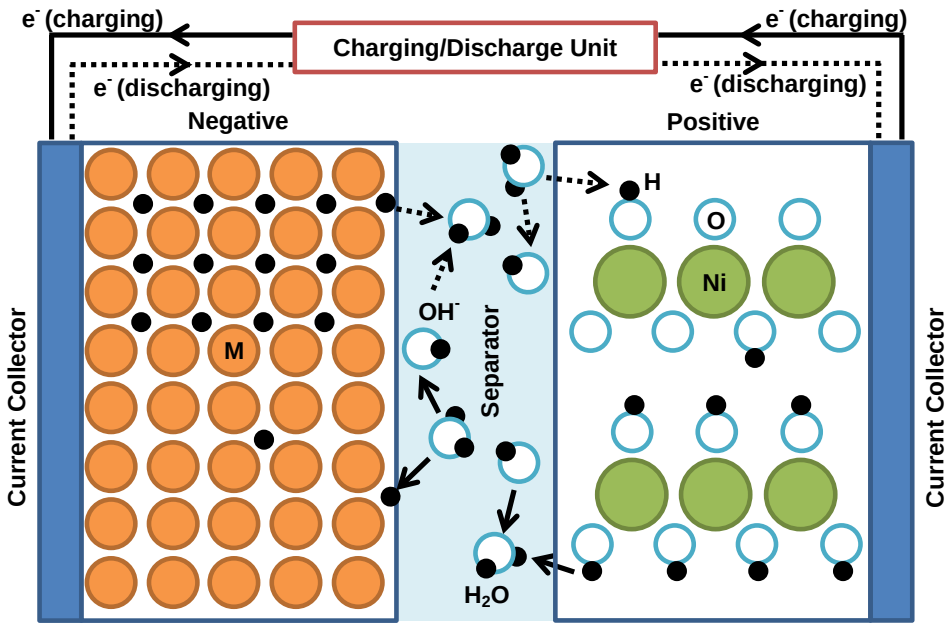

Figure 1. Schematic of NiMH battery charging and discharging processes

A NiMH battery was demonstrated by researchers at Battelle Memorial Institute in the 1976 patent using a Ti-Ni-based alloy for the anode and nickel counter-electrodes [3]. By 1989, independent NiMH battery commercialization by Ovonic Battery Company, Sanyo, and Matsushita saw consumer NiMH cylindrical cells for portable devices and later prismatic cells for electric vehicle applications [4]. These cells utilized different active anode materials designed with a set of specific properties appropriate for an individual application.

Commercially-available active anode materials for NiMH batteries can be divided into three major categories of hydrogen storage alloys based on the overall alloy stoichiometry: AB_5, AB_2, and A_2B_7. AB_5 materials such as $LaNi_5$ have been used in batteries for hybrid electric vehicles for their long life and reliability. They have lower capacity than their AB_2 and A_2B_7 counterparts and with the rise in prices of rare earth metals like La, Pr and Nd in recent years, interest in rare earth metal-free AB_2 materials has risen in NiMH battery research.

NiMH batteries share the same active cathode materials as nickel-cadmium, nickel-iron, nick-zinc, and nickel-hydrogen cells: nickel hydroxide. Nickel hydroxide has been used since 1901, when Thomas Edison patented his rechargeable nickel-zinc battery system. It has also found use as the precursor to some lithium-ion cathode materials and in pseudocapacitors, extending energy storage capacity while maintaining high power.

2.1.1 C14 and C15 Laves Phase AB_2 Anode Materials

AB_2 hydrogen storage alloys used in NiMH battery electrodes are multi-compositional, multi-phase materials typically composed of a main Laves phase or phases and other minor secondary phases [5]. Laves phases, a family of AB_2 intermetallic compounds named for Fritz Laves, share crystallographically-related structures and differ only in the stacking of a shared fundamental structure unit. They are represented by three main polytypes known as C14 (hexagonal $MgZn_2$), C15 (face-centered cubic $MgCu_2$), and C36 (hexagonal $MgNi_2$), and two or more polytypes may exist as equilibrium phases in multi-element alloy systems [6]. The polytypes or phases that are commonly observed in AB_2 hydrogen storage alloys designed for NiMH batteries are C14 and C15, and each phase has a function in electrochemical performance. Hexagonal C36 phase may exist as a small fraction but is not detectable by x-ray diffraction (XRD) spectroscopy. High-resolution transmission electron microscopy is a technique that can distinguish C36 phase from C14 phase.

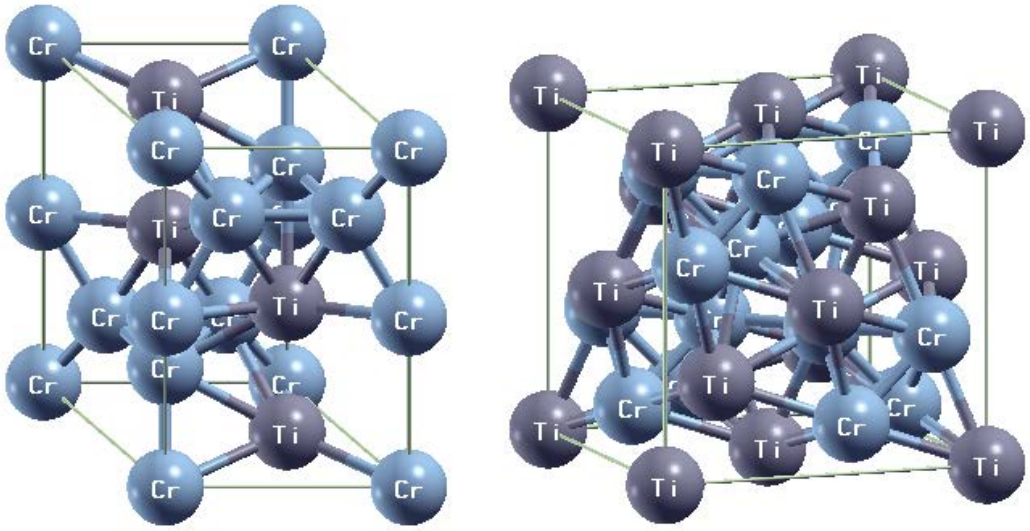

Figure 2. C14 and C15 Laves phase crystal structures for $TiCr_2$

Hexagonal C14 structure, illustrated in Figure 2 on the left, belongs to the $P6_3/mmc$ space group and contains four AB_2 formula units per unit cell [7]. A-atom sites correspond to the *4f* Wyckoff position and B-atoms occupy the *2a* and *6h* positions. Face-centered cubic C15 structure, illustrated in Figure 2 on the right, belongs to the $Fd\bar{3}m$ space group and contains eight AB_2 formula units per unit cell. A-atom sites correspond to the *8a* Wyckoff position and B-atoms occupy the 1*6d* sites. Table 1 contains additional site position information for C14 and C15 Laves phase structures.

Table 1. C14 and C15 Laves phase crystal site positions [7]

		Wyckoff Position	Site Symmetry	x	y	z
C14						
	A	4f	3m	0.333	0.667	0.062
	B1	2a	-3m	0.000	0.000	0.000
	B2	6h	mm2	0.833	0.667	0.250
C15						
	A	8a	-43m	0.000	0.000	0.000
	B	16d	-3m	0.625	0.625	0.625

Upon hydrogen absorption, hydrogen occupies tetrahedral interstitial sites within the hydrogen storage alloy [7]. In both C14 and C15 Laves phases, there are three types of possible sites for hydrogen to occupy: 4B (in which four B-atoms form the tetrahedral site), 1A3B and 2A2B. Examples of each of these sites are illustrated in C14 structure shown in Figure 3. Where in C15 phase A-atoms occupy only 8a sites and B-atoms occupy only 16d sites, A- and B-atoms are locally equivalent in the tetrahedral sites; B-atoms in C14 phase occupy both 2a and 6h sites, which further subdivides the types of interstitial sites in C14 phase, making them non-locally equivalent. In C15 phase, the 4*B*, 1*A*3*B* and 2*A*2*B* sites correspond to the 8*b*, 32*e* and 96*g* Wyckoff positions respectively. The most favorable of these sites is the *g* site, followed by the *e* site, which is favorable after three H-atoms per AB_2 formula unit are filled [8-10]. In C14 phase, the 4*B* sites correspond to the 4*e* Wyckoff position, the 1*A*3*B* sites correspond to the 4*f* and $12k_1$ positions, and the 2*A*2*B* sites correspond to the $6h_1$, $6h_2$, $12k_2$, and 24*l* positions. There are 17 tetrahedral sites that exist per AB_2 formula unit, but due to electrostatic effects only five or six hydrogen atoms maximum are ever observed [7]. In order to store hydrogen, the tetrahedral site must be large enough (r > 0.4 Å) and far away enough from adjacent occupied sites (H-H distance > 2.1 Å) [11].

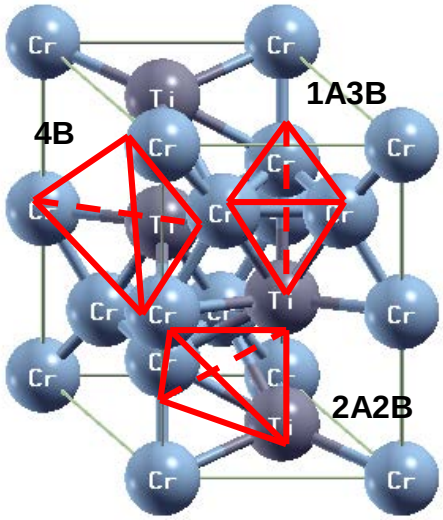

Figure 3. Examples of 4B, 1A3B, and 2A2B tetrahedral sites in C14 Laves phase structure

Zhang and et al. isolated C14 and C15 phases through annealing treatment, which homogenized the sample alloys into a single, stable phase. The stable phase depended on the electron-atom ratio in the alloy composition according to their studies. Electrochemical tests showed improvement in cycle life but difficulty in activation due to homogeneity to both stable phases, but individually, C14 phase appeared to play a large role in electrochemical activity with contributions from minor secondary phases [12-14]. Young et al. investigated the contributions of the different phases on electrochemical performance in more detail, preparing a series of multi-elemental alloys based on average electron density (*e/a* value) that yielded a range of C14 and C15 compositions from C14-rich to C14-lean. They reported a trend towards better gaseous phase storage capacity, reversibility and high rate dischargeability (HRD) in C15-rich samples, and a trend towards better electrochemical capacity and cycle life in C14-rich samples [15-17]. There is a balance between C14, C15, and secondary phases that maximizes capacity and high-rate potential without sacrificing electrochemical activity and cycle life, but there are also valuable commercial applications that require certain specifications without requiring others.

Understanding the structure and equilibrium behavior of Laves phase materials to predict phase abundances from a given alloy composition enables a more optimized design of NiMH batteries and battery materials and is one subject of this prospectus for designing high performance battery materials.

Due to their unique hydrogen-storage, structural and magnetic properties, Laves phase materials have been an area of interest for the research community since Friauf and Laves first studied them. Geometric and electronic factors and their effect on the Laves phase stable structures have long been studied, even by Laves himself [18]. The effects of these factors have been revisited over the years for specific systems [19-22]. Johnston et al. studied the structure and bonding relationships among the different polytypes/phases and used tight-binding calculations to establish a cyclical relationship between electron count and C14/C15 stable structures, with good agreement for the first row transition-metals [23]. In 2004, Stein et al. assessed the factors that control Laves phase stability, which include atomic size, electronegativity, and valence concentration in a comprehensive review paper [24]. Stein concluded that while the studies and models that he reviewed were valid for particular systems of study, none were able to give a complete and consistent description valid for all Laves phase compounds. He also noted that many *ab initio* calculations were able to predict the ground state structures of Laves phase compounds, but the stable formation phases found that real systems are also affected by off-stoichiometry compositions and temperature [25]. A 2012 review paper by Macaluso et al. re-emphasized the limited use of models and calculations conducted for Laves phases as a class of materials as a whole thus far, citing same the challenges summarized by Stein et al. in predicting intermetallic phases [26]. Since then, Nei et al. has correlated chemical

potential of electronic charge to electron density for an accurate prediction of C14/C15 threshold in stoichiometric compositions of AB_2 alloys [27].

The Johnston model uses the semi-empirical extended Hückel method to calculate the energies of C14 and C15 structures of AB_2 materials using A=Ti and B=Fe, with varying electron densities. As such, it has good agreement with first row transition metals, but not so good agreement with other transition metals such as $ZrCr_2$ ($16e^-$ per AB_2 unit, C15 structure), $NbCr_2$ ($17e^-$, C15 structure), and $NbFe_2$ ($21e^-$, C14 structure). Other known alloy formulas in literature such as $Ti_{12}Zr_{21.5}V_{10}Ni_{40.2}Co_{1.5}Cr_{8.5}Mn_{5.6}Al_{0.4}Sn_{0.3}$ report a C14-rich structure with an *e/a* value of 6.91 [16]. According to the model, the sample alloy formula has 20.73 valence electrons per AB_2 unit and would have C15 structure. *Ab initio* calculations such as density functional theory-based methods can be applied accurately to specific compositions to give us more insight in the role that electronic structure and atomic sizes have on the phase stability of C14/C15 structures.

While *ab initio* calculations reliably produce structures that agree with experiment at the ground state (0K), effects such as temperature and cooling rates are neglected. Temperatures and cooling rates are beyond the scope of this study at this point. We will focus on determining trends that will allow us to consistently predict the ground state structure of an alloy given its composition, and start from there.

2.1.2 Nickel Hydroxide Cathode Materials

Nickel hydroxide in the β-form is the main cathode active material used in NiMH batteries (the usage of the term "nickel hydroxide" in this paper refers to the β-form unless otherwise noted). As a metal oxide material, nickel hydroxide possesses a layered crystal structure in the CdI_2-type hexagonal system [28] seen in Figure 4 and is intrinsically a good

insulator. What makes the transfer of electrons possible in metal oxides — such as nickel hydroxide — is the presence of defects in the crystal structure, which specifically include cation substitutions, cation vacancies, stacking faults, and lattice strain in the case of these layered oxides [29].

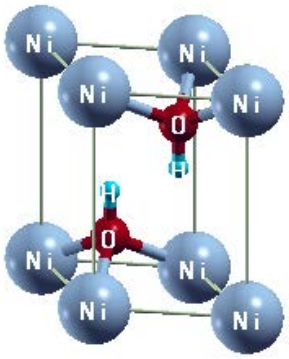

Figure 4. Nickel hydroxide crystal structure

The crystal structure of nickel hydroxide belongs to the $P\bar{3}m1$ space group with Ni occupying the *1a* Wyckoff position and O and H occupying *2d* positions [30]. Lattice constants are a = 3.13 Å and c = 4.63 Å. Table 2 contains the site position information for nickel hydroxide.

Table 2. Nickel hydroxide crystal site positions [30]

	Wyckoff Position	Site Symmetry	x	y	z
Ni	1a	-3m	0.000	0.000	0.000
O	2d	3m	0.333	0.667	0.240
H	2d	3m	0.333	0.667	0.470

Terasaka et al. disclosed the correlation of nickel hydroxide powder XRD peaks to electrochemical performance in their 1993 patent on nickel electrodes for alkaline rechargeable batteries [31]. They claimed that nickel hydroxide powder with crystallite sizes derived from the (101) peak falling within the 80-125Å range has high capacity utilization and exhibits less

swelling. Bernard et al. found that crystallite sizes calculated from the (001) and (100) peaks matched the sizes measured from transmission electron microscopy images, but the sizes calculated from the (101), (102), (103) peaks under-predicted the observed crystallite sizes [32]. In addition to an unexpected line observed in Raman spectroscopy experiments, they suggested that structural defects, particularly vacancies, were related to high electrochemical activity and broadening of the (10*l*) and (20*l*) family of peaks.

Delmas and Tessier surmised that lower values of coherence lengths along (10l) lines arose from constructive interferences that varied with the plane orientation, and they associated nickel hydroxide's high electrochemical activity and (10l) peak broadening to the presence of stacking faults [29, 33]. They used the program DIFFAX [34] to simulate XRD patterns in faulted crystal structures and then identified and quantified the type and degree of faulting. Casas-Cabanas et al. developed the FAULTS program, based on the DIFFAX code, to include Rietveld refinement [35]. In developing the FAULTS program and comparing its results to traditional Rietveld refinement, Casas-Cabanas attributed the (101) and (102) peak broadening of electrochemically-active nickel hydroxide to anisotropic size effects, with only incidental contribution from stacking faults [36-38]. Ramesh and Kamath also studied the peak broadening contributions from size effects and stacking faults and how the different contributions affect electrochemical performance [39-42]. Tripathi et al. worked with Ramesh and Kamath to conduct a first-principles study on nickel hydroxide and its stacking faults, and confirmed by DFT the possible stacking faults first proposed by Delmas and Tessier [43]. Hermet et al. conducted a first-principles study of nickel hydroxide that takes a more detailed look at electronic band structure and magnetic properties [44]. The different nickel hydroxide polytypes

are shown in Figure 5, and their stacking sequences and crystal coordinates are given in Table 3 and Table 4.

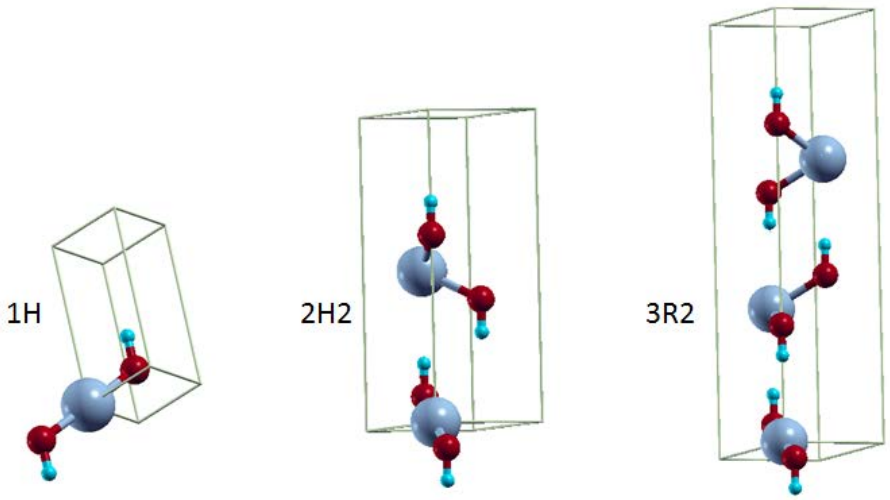

Figure 5. Nickel hydroxide polytypes 1H, 2H2, 3R2 [40]

Table 3. Nickel hydroxide polytypes and calculated energy differences [43]

	Stacking Sequence	Energy Difference (eV)
1H	*ACACACAC…*	-
2H2	*ACACABAB…*	0.006
3R2	*ACACBACB…*	0.012

Table 4. Coordinates for types of nickel hydroxide stacking

		x	y	z
AC				
	Ni	0.000	0.000	0.000
	O1	0.333	0.667	0.240
	O2	0.333	0.667	-0.240
AB				
	Ni	0.333	0.667	0.000
	O1	0.000	0.000	-0.240
	O2	0.333	0.667	0.240
BA				
	Ni	0.333	0.667	0.000
	O1	0.000	0.000	0.240
	O2	0.333	0.667	-0.240
CB				
	Ni	0.333	0.667	0.000
	O1	0.333	0.667	0.240
	O2	0.000	0.000	-0.240

It is still unclear the exact contributions of anisotropic size effects and stacking faults to (101) peak broadening, and consequently to electrochemical performance. Ramesh concluded that crystallite size has the greatest impact electrochemical performance regardless of additives, yet cobalt and zinc additives to nickel hydroxide cathode materials are an industry standard [45]. Oshitani et al. documented the effect of additives such as cobalt, zinc and magnesium to the nickel hydroxide precipitation reaction [46, 47]. Cobalt oxide has been used in nickel hydroxide electrodes to act as a conductive network [48], but co-precipitation with cobalt additives also boosts capacity utilization [49]. The co-precipitation of the additives not only adds more conductive materials into the nickel hydroxide, but also introduces compositional disorder and defects into the crystal structure. Casas-Cabanas and Ramesh recognized that stacking faults do play a role in electrochemical performance, as do anisotropic size effects – the question is to

what extent and can we predict them and extend the prediction to cathode and anode materials of various battery chemistries?

There is another aspect of the research from literature that must be considered. The nickel hydroxide samples analyzed and presented from the various research groups tend to be conducted under flooded conditions with various amounts of conductive additives that are not considered in the active material weight. While the conductive additives and flooded cell configuration provides a baseline for comparison across the various research groups by removing conductivity limitations, the reported specific capacities may not necessarily correlate with performance in a sealed battery cell. The sealed battery cell operates under semi-flooded or electrolyte-starved conditions, and any conductive additive contributes to the overall weight of the cell – all with measurable effects on cell performance with real cell design constraints. The sealed cell has its own set of considerations such as poisoning to the nickel electrode, which are beyond the scope of this study, and so a sealed cell may not necessarily be the most appropriate setup either. We are most interested in how stacking faults affect battery performance. If we surmise that stacking faults affect the inherent conductivity of nickel hydroxide, then copious amounts of conductive additives may mask the effect of the stacking faults. It is this masking effect that may have led the Casas-Cabanas and Ramesh groups to come to the conclusions that they reported.

We analyze just how important a role that conductivity plays in active material utilization. In order to store or obtain electricity from a battery, electrons and ions must flow, and any interruption or barrier in the conduction paths cuts off useable capacity. Electrons and ions must navigate through several bulk materials/phases and the interfaces that bridge them. Following the path that an electron takes on the cathode side, there is the current collector that must be

highly conductive. The current collector interfaces with the cathode material, which must have good contact for the electrons to move from substrate-to-particle, from particle-to-particle, and from the surface to the bulk. The substrate-to-particle and particle-to-particle contact is where conductive additives can boost the cathode material utilization. Figure 6 illustrates a schematic of this contact structure, and it clearly shows how the amount of conductive additive as well as the uniformity of conductive additive can affect access to usable cathode capacity [50]. Particle size and shape also play a role in the usable cathode capacity [49, 51].

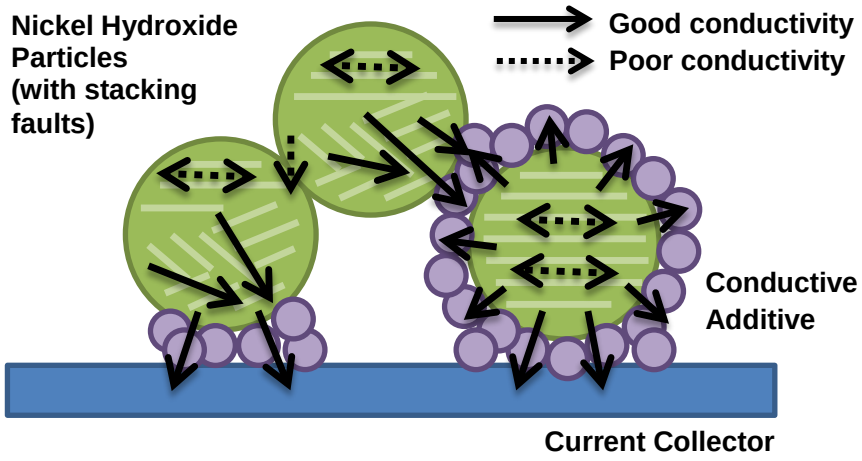

Figure 6. Schematic of cathode material contact structure

Concurrent with electronic transport across the interfaces is the ionic transport. Smaller particles have higher surface area per gram for H^+ to move to and from the electrolyte. Higher surface area means more reactivity sites for electrochemistry to occur. High-resolution transmission electron microscopy (HRTEM) images from Casas-Cabanas et al. show the "amorphous" surface of a nickel hydroxide platelet and the highly crystalline, layered structure of the bulk [37]. The surfaces contain deformations to the crystal lattice, facilitating electronic and ionic transport, and so higher surface-area-to-bulk-volume ratios are better conducive to electrochemical performance. Wetting of the electrode pores is another consideration for ionic

transport and access to usable cathode capacity. Cells tested under flooded electrolyte conditions have an advantage over semi-flooded/starved conditions.

The ease of transport of electrons and H^+ ions from the surface to the bulk also determines access to usable capacity. Electrons move within nickel layers, and the inherently poor conductivity of nickel hydroxide tends not to conduct electrons between layers unless a conductive dopant such as cobalt has been co-precipitated into the structure, or defects to the crystal structure such as stacking faults are present in the material. H^+ ions move through the channels between the $Ni(OH)_2$ layers, and shorter channels created through stacking faults allows easier access to all sites. Figure 7 shows the electronic and ionic paths possible through nickel hydroxide active material based on the crystal structure. Any deficiency in electronic transport or ion transport inside the cell at any of the levels discussed reduces its usable capacity.

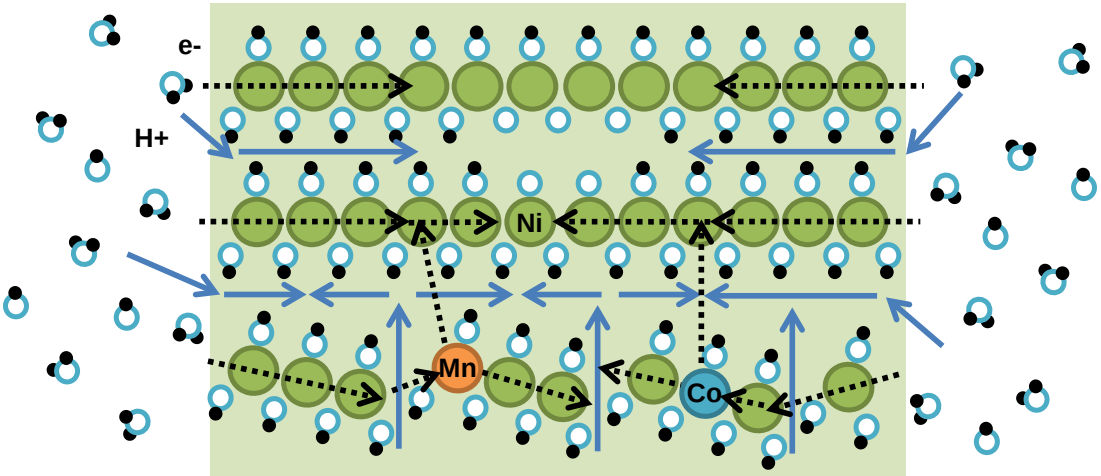

Figure 7. Schematic of electronic and ionic access paths in nickel hydroxide active material

With the methodologies reported for most research conducted in the field, it is near impossible to tell whether stacking faults and/or dopants are having their desired effect on active material samples and whether the samples will work practically in a real cell. The baseline used in the literature review may be appropriate for consistently evaluating maximum capacities, but

the baseline also compresses all data to near the maximum theoretical capacity, making it difficult to discern effects occurring within the nickel hydroxide layers. Shifting the baseline to include all inherent conductivity limitations is one way to evaluate nickel hydroxide-based cathode material (i.e. starved-electrolyte conditions and no conductive binder); however the sealed cell conditions introduce other considerations into the experimental setup. The industrial standard of 15% conductive additive in commercial cathode material is one possible baseline, and maintaining flooded cell conditions will be easier to keep consistent across test samples. Evaluating an appropriate baseline for studying stacking faults and dopants will be one aspect of this study. Electrochemical impedance spectrometry studies that characterize charge-transfer resistance of each of the materials will also be important.

Table 5 summarizes some of specific capacity and crystallite dimension data from literature. Figure 8 plots some of the trends with respect to crystallite dimensions.

Table 5. Survey of nickel hydroxide specific capacity and crystallite size

Composition	Capacity (mAh/g)	Thickness (Å)	Disc diameter (Å)	Reference
$Ni_{0.992}Co_{0.008}(OH)_2$	197	94	335	[37]
$Ni_{0.972}Co_{0.025}Zn_{0.003}(OH)_2$	230	67	201	[37]
$Ni_{0.985}Co_{0.015}(OH)_2$	220	47	165	[37]
$Ni_{0.988}Co_{0.012}(OH)_2$	198	109	346	[37]
$Ni(OH)_2$	99	119	719	[37]
$Ni(OH)_2$	127	140	476	[37]
$Ni(OH)_2$	210	53	179	[37]
$Ni(OH)_2$	241	41	138	[37]
β_{bc}-$Ni(OH)_2$	260	30	254	[45]
β_{bc}-$Ni_{0.94}Co_{0.06}(OH)_2$	188	31	149	[45]
β_{bc}-$Ni_{0.82}Co_{0.12}(OH)_2$	197	37	179	[45]
β_{bc}-$Ni_{0.74}Co_{0.26}(OH)_2$	202	39	245	[45]
β_{bc}-$Ni_{0.85}Zn_{0.15}(OH)_2$	173	51	216	[45]
β_{bc}-$Ni_{0.83}Zn_{0.17}(OH)_2$	188	32	225	[45]
β_{bc}-$Ni_{0.82}Zn_{0.18}(OH)_2$	159	51	216	[45]
β_{bc}-$Ni_{0.94}Ca_{0.06}(OH)_2$	220	30	149	[45]
β_{bc}-$Ni_{0.94}Cd_{0.06}(OH)_2$	202	39	151	[45]
β-$Ni(OH)_2$	116	674	458	[45]
β-$Ni_{0.95}Co_{0.05}(OH)_2$	116	528	679	[45]
β-$Ni_{0.83}Zn_{0.17}(OH)_2$	0	300	376	[45]
β-$Ni_{0.95}Cd_{0.05}(OH)_2$	0	498	273	[45]
$Ni(OH)_2$	207	199	415	[49]
$Ni(OH)_2$	267	102	380	[49]
$Ni_{0.933}Ca_{0.067}(OH)_2$	270	99	341	[49]
$Ni_{0.945}Co_{0.055}(OH)_2$	278	98	306	[49]
$Ni_{0.949}Zn_{0.051}(OH)_2$	272	94	277	[49]

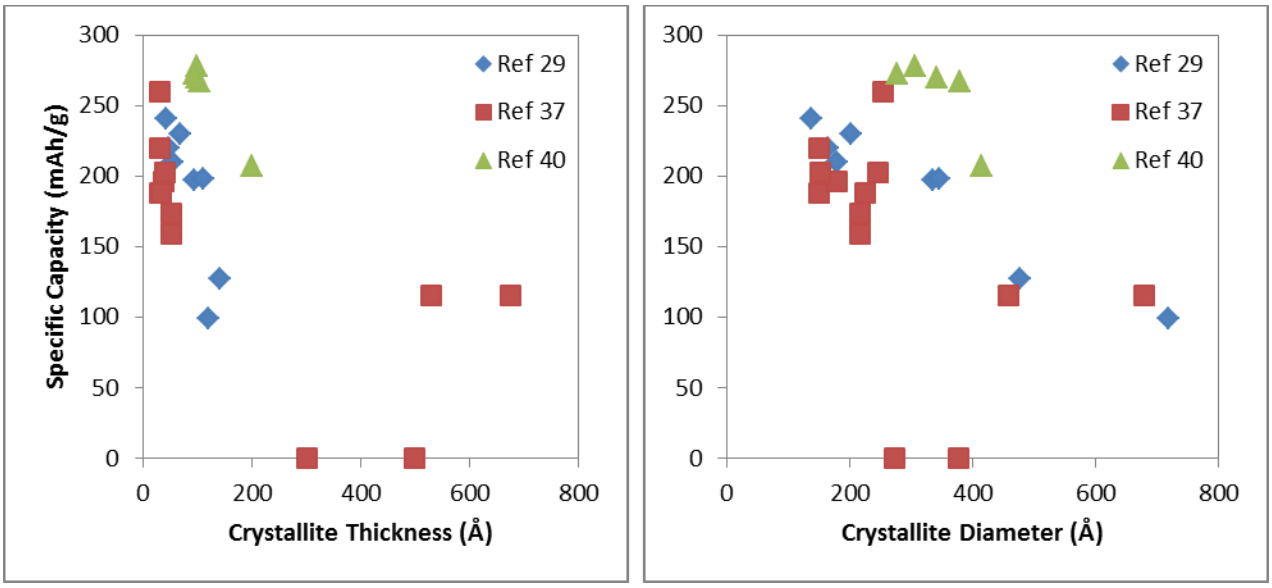

Figure 8. Survey of nickel hydroxide capacity with respect to crystallite dimensions

100% utilization of nickel hydroxide active material corresponds to one electron transfer (Ni^{2+}/Ni^{3+}) and a theoretical 289 mAh/g specific capacity. The highest capacity analyzed and reported in the literature reviewed for this study is ~240-260 mAh/g (89-95% utilization), while capacities greater than 290 mAh/g (>100% utilization) have also been reported. The groups use varying amounts of conductive additive under flooded conditions and report capacities based on the nickel hydroxide weight. The additive amounts range from 15% to almost 55% of the total electrode paste weight. In order to reach >290 mAh/g specific capacity, the electrochemical reactions will need access to a second electron transfer, which competes with the oxygen evolution reaction at +0.4 vs. SHE. Specific capacities as high as 330 mAh/g have been reported for amorphous nickel hydroxide [52]. With the lack of XRD peaks, these amorphous/nano-crystalline nickel hydroxide materials are beyond the scope of this proposed research study.

2.2 Density Functional Theory

Density functional theory (DFT) has enabled the modeling of materials and their properties using quantum mechanical calculations with reasonable accuracy and speed. DFT takes the problem of many-body systems and maps its properties to a functional of the system's ground state density. The ground state density is a scalar function of position, and an approximate solution to the Schrödinger equation can be obtained for large many-bodied systems where direct numerical solutions involving the many-bodied wavefunction would be too resource-consuming to solve. Ref. [53] and [54] are excellent resources for understanding the background and theory behind computational chemistry and DFT, and this section relies on these two resources as well as the original journal sources for the describing how DFT fits in the scope of this work.

2.2.1 Born-Oppenheimer Approximation

The Hamiltonian describes the kinetic and potential energies between interacting electrons and nuclei within a system of interest. Taking into account the kinetic energies and all Coulomb interactions (electron-nuclei, electron-electron, and nuclei-nuclei) yields

$$\hat{H} = -\frac{\hbar^2}{2m_e}\sum_i \nabla_i^2 + \sum_{i,I}\frac{Z_I e^2}{|\boldsymbol{r}_i - \boldsymbol{R}_I|} + \frac{1}{2}\sum_{i\neq j}\frac{e^2}{|\boldsymbol{r}_i - \boldsymbol{r}_j|} - \sum_I \frac{\hbar^2}{2M_I}\nabla_I^2 + \frac{1}{2}\sum_{I\neq J}\frac{Z_I Z_J e^2}{|\boldsymbol{R}_I - \boldsymbol{R}_J|},$$

where lower case symbols denote electrons and upper case symbols denote nuclei for position vector $\boldsymbol{r}$, mass m, electronic charge e, and nuclear charge Z_I [53]. The large difference in mass between electrons and the nuclei leads to the Born-Oppenheimer approximation, in which the motion of the nuclei is essentially negligible compared to the motion of the electrons and the kinetic term for the nuclei can be largely ignored [55]. This simplifies the Hamiltonian, using Hartree atomic units, to

$$\hat{H} = \hat{T} + \hat{V}_{ext} + \hat{V}_{int} + E_{II},$$

where $\hat{T}$ is the kinetic energy operator for the electrons,

$$\hat{T} = \sum_i -\frac{1}{2}\nabla_i^2 ,$$

$\hat{V}_{ext}$ is the external potential from the nuclei acting on the electrons,

$$\hat{V}_{ext} = \sum_{i,I} V_I(|\boldsymbol{r}_i - \boldsymbol{R}_I|) ,$$

$\hat{V}_{int}$ is the internal potential that arises from electron-electron interactions,

$$\hat{V}_{int} = \frac{1}{2}\sum_{i \neq j} \frac{1}{|\boldsymbol{r}_i - \boldsymbol{r}_j|} ,$$

and E_{II} is the interaction between nuclei. The Born-Oppenheimer approximation allows the electronic motion to be separated from the atomic nuclei, which can now be viewed as an external potential acting on a collection of electrons.

2.2.2 Schrödinger Equation

The time-dependent Schrödinger equation governs the quantum state of a many-bodied system with respect to time by

$$i\hbar\frac{\partial}{\partial t}\Psi = \hat{H}\Psi ,$$

where the Ψ is the wavefunction of the system [53]. Solutions of the time-independent Schrödinger equation

$$E\Psi = \hat{H}\Psi ,$$

describe the wavefunctions that form stationary states (also known as "orbitals") for the system. The proportionality constant when the Hamiltonian operator acts on one of the stationary states is the energy, *E*, of the state. The total energy of the system is the expectation value of the Hamiltonian

$$E = \frac{\langle \Psi | \hat{H} | \Psi \rangle}{\langle \Psi | \Psi \rangle} = \langle \hat{H} \rangle = \langle \hat{T} \rangle + \langle \hat{V}_{\text{int}} \rangle + \int \mathrm{d}^3 r \, V_{\text{ext}}(\boldsymbol{r}) \, n(\boldsymbol{r}) + E_{II} \, ,$$

where the expectation value of the external potential has been rewritten in terms of the electron density *n*. The total energy of the system can be minimized to find the ground state wavefunction Ψ_0 of the system. It has an associated ground state density n_0.

2.2.3 Thomas-Fermi-Dirac Approximation

Thomas and Fermi first used a functional of density to approximate the electronic kinetic energy while neglecting the electron exchange and correlation interactions. Dirac included the exchange interactions in the energy functional

$$E_{\text{TF}}[n] = C_1 \int \mathrm{d}^3 r \, n(\boldsymbol{r})^{(5/3)} + \int \mathrm{d}^3 r \, V_{\text{ext}}(\boldsymbol{r}) n(\boldsymbol{r}) + C_2 \int \mathrm{d}^3 r \, n(\boldsymbol{r})^{(4/3)}$$

$$+ \frac{1}{2} \int \mathrm{d}^3 r \mathrm{d}^3 r' \, \frac{n(\boldsymbol{r}) n(\boldsymbol{r}')}{|\boldsymbol{r} - \boldsymbol{r}'|} \, ,$$

where C_1 and C_2 are known constants [53]. Minimizing the energy gives the ground state density and energy when subject to the constraint

$$\int \mathrm{d}^3 r \, n(\boldsymbol{r}) = N.$$

The electron density can be viewed as the probability of finding electrons for a given space. For *N* indistinguishable electrons, the electron density is *N* times the probability of finding an electron in the space. Compared to the traditional 3*N* degrees of freedom for *N* electrons required to determine the ground state wavefunction to find the ground state energy, Thomas, Fermi and Dirac laid the groundwork for DFT, reducing the requirements to finding the ground state energy to *N* degrees of freedom. However, their approximation considers the homogenous electron gas and oversimplifies aspects of inhomogeneous systems such as atoms and metals

with impurities, which makes this method less useful for determining the electron structures needed to accurately model materials [56].

2.2.4 Hohenberg-Kohn Theorems

The theorems developed by Hohenberg and Kohn allow for an exact approach to density functional theory that applies to any system of interacting particles subject to an external potential, particularly the system of electrons and fixed nuclei described in Section 2.2.1 from the Born-Oppenheimer approximation. The theorems state [53, 56]:

1. Two external potentials $V_{\text{ext}}(\mathbf{r})$ and $V'_{\text{ext}}(\mathbf{r})$ with the same ground state density n_0 can only occur if $V'_{\text{ext}}(\mathbf{r}) - V_{\text{ext}}(\mathbf{r}) = \text{const}$, given that the ground states $\Psi_0 \neq \Psi'_0$.

   Corollary: This theorem leads to the inconsistency that $E + E' < E + E'$, which follows that the ground state density must uniquely determine the external potential (within a constant), thus determining all properties of the system.

2. For any system of N particles and any external potential $V_{\text{ext}}(\mathbf{r})$, there exists a universal functional $F[n]$ encompassing the kinetic and interaction energy such that $E[n] \equiv F[n] + \int \mathrm{d}^3 r\, V_{\text{ext}}(\boldsymbol{r}) n(\boldsymbol{r})$. $E[n]$ is the global energy minimum, which is also the ground state energy, when $n(\boldsymbol{r})$ is exactly $n_0(\boldsymbol{r})$, the ground state electron density.

   Corollary: This theorem shows that if $F[n]$ and the external potential are known, it is sufficient to determine the ground state energy and ground state density.

By the Hohenberg-Kohn theorems, then:

$$E_{\text{HK}}[n] = T[n] + E_{\text{int}}[n] + \int \mathrm{d}^3 r\, V_{\text{ext}}(\boldsymbol{r}) n(\boldsymbol{r}) + E_{II} \equiv F_{\text{HK}}[n] + \int \mathrm{d}^3 r\, V_{\text{ext}}(\boldsymbol{r}) n(\boldsymbol{r}) + E_{II}\,,$$

where $E_{\text{HK}} = E$, the exact energy of the system, and $F_{\text{HK}}[n]$ is the universal functional

$$F_{\text{HK}}[n] = T[n] + E_{\text{int}}[n]\,,$$

where $T[n]$ is the kinetic energy functional and $E_{\text{int}}[n]$ is the interaction energy functional. While the Hohenberg-Kohn theorems provide an exact approach to density functional theory to obtaining the ground state energy and density, the exact functionals are not known except for in certain, limiting cases that do not describe actual electronic systems.

2.2.5 Kohn-Sham Equations

The contributions that Kohn and Sham have made to density functional theory along with the advances in computing technology have enabled the widespread use of electronic structure calculations for the modeling of materials today. Their approach recasts the Hamiltonian that defines the many-bodied system into an auxiliary system that is more easily solved. The auxiliary independent particle Hamiltonian is defined as

$$\hat{H}^{\sigma}_{\text{aux}} = -\frac{1}{2}\nabla^2 + V^{\sigma}_{\text{eff}}(\boldsymbol{r}) \,,$$

which consists of a non-interacting kinetic energy term and V^{σ}_{eff}, an effective local potential acting on an electron with spin σ [53, 57]. This rewrites the Hohenberg-Kohn energy functional to

$$E_{\text{KS}}[n] = T_{\text{s}}[n] + \int \mathrm{d}^3 r \, V_{\text{ext}}(\boldsymbol{r}) n(\boldsymbol{r}) + E_{\text{Hartree}}[n] + E_{II} + E_{\text{xc}}[n] \,,$$

where T_{s} is the non-interacting kinetic energy, E_{Hartree} is the interaction energy of the electron density interacting with itself

$$E_{\text{Hartree}}[n] = \frac{1}{2}\int \mathrm{d}^3 r \mathrm{d}^3 r' \frac{n(\boldsymbol{r}) n(\boldsymbol{r}')}{|\boldsymbol{r} - \boldsymbol{r}'|} \,,$$

and E_{xc} captures the remaining exchange and correlation energy from the interacting particles. E_{xc} is thus defined as

$$E_{\text{xc}}[n] = F_{\text{HK}}[n] - (T_{\text{s}}[n] + E_{\text{Hartree}}[n]) = \langle \hat{T} \rangle - T_{\text{s}}[n] + \langle \hat{E}_{\text{int}} \rangle - E_{\text{Hartree}}[n] \,,$$

which is the difference between the true kinetic and internal interaction energies of the interacting system with the energy of the independent, non-interacting system that has substituted the Hartree energy for the internal interaction energy. The effective local Kohn-Sham potential is finally defined as

$$V_{\text{eff}}^{\sigma}(\boldsymbol{r}) = V_{\text{ext}}(\boldsymbol{r}) + V_{\text{Hartree}}(\boldsymbol{r}) + V_{\text{xc}}^{\sigma}(\boldsymbol{r}) .$$

There is a tradeoff with the Kohn-Sham approach. All of the terms are known exactly with the exception of E_{xc}, which can be approximated. However, obtaining T_{s} requires the treatment of orbitals rather than the density, which increases the degrees of freedom of the system back to $3N$. Approximation methods for E_{xc} make the tradeoff acceptable in terms of increased accuracy for the resource usage.

2.2.6 Exchange-Correlation Functionals

The functionals for approximating E_{xc} fall under three general classes: local density approximation (LDA), generalized gradient approximation (GGA) and hybrid functionals [53, 54]. The LDA method uses the density of a uniform electron gas integrated over all space to approximate the exchange-correlation energy. GGA methods improve upon the LDA method by incorporating the gradient of the density for each point in space, while requiring that the Fermi and Coulomb hole properties be preserved. Hybrid methods construct functionals from a combination of LDA/GGA exchange-correlation functionals with the exact exchange energy functional from Hartree-Fock theory. Benchmarks for LDA and GGA methods show that GGA results (average absolute error 0.3 eV) improve bulk cohesive energy calculations over LDA results (average absolute error 1.3 eV) due to the underestimation of the exchange energy in the LDA [58]. Popular and successful GGA functionals have been proposed by Becke (B88) [59], Perdew-Wang (PW86, PW91) [60, 61], and Perdew-Burke-Ernzerhof (PBE) [62]. The PBE

functional has found wide use in modeling materials, especially within the transition metal system, which makes it suitable for modeling alloy materials.

2.2.7 Ground State Structure and Energy of Formation

A known external potential fixes the locations of the atoms within a specific structure. The energy of the specific configuration of atoms is determined when the energy within the DFT framework reaches a minimum over the iterations the electron distribution and its structure. In order to find the ground state structure for a system of interest, a minimization routine, typically a quasi-Newtonian algorithm, is used to iterate over atomic positions in until a minimum energy, zero forces, and zero stresses are reached. The relative stability of the ground state structures is defined by the energy of formation

$$\Delta H_f = \frac{E(A_n B_m) - \frac{n}{l}E(A_l) - \frac{m}{k}E(B_k)}{n+m},$$

where A_a and B_b are the constituent elemental compounds of the compound of interest A_nB_m. A_l and B_k, for example, may be of the forms body-centered cubic, face-centered cubic, hexagonal, etc, and l and k are the numbers of basis atoms in the respective unit cells.

2.3 Materials Characterization Techniques and Modeling

Materials characterization techniques that involve an aspect of simulation and modeling include x-ray diffraction and electrochemical impedance spectroscopy analysis. Ref [63] contains comprehensive background and theory on x-ray diffraction practices and applications, and it is the main source for the x-ray diffraction section of this work. Ref [64] contains the background and theory on electrochemical impedance spectroscopy, and it is the source for the electrochemical impedance spectroscopy section.

2.3.1 X-Ray Diffraction

X-ray diffraction (XRD) is a powerful technique used in the structural characterization and identification of crystalline materials. It takes advantage of the wave nature of x-ray radiation and its constructive and destructive interference properties as it is aimed through materials with specific three-dimensional periodicity of dense atomic nuclei and diffracted. Most of the x-rays pass through the material, but the x-rays that encounter the nuclei can be absorbed, reflected back, or deflected at a known deflection angle. For planes of atoms showing periodicity with a separation distance *d*, x-rays traveling at an incident angle θ to the planes do not travel the same distance when they encounter nuclei within the set of planes, which causes a shift in phase in the x-rays as they are deflected. Most phase shifts cause partial or complete destructive interference of the x-rays, resulting in reduced intensity of the x-rays at the detector. However, constructive interference can occur at certain angles, when the distance that causes the phase shift is a multiple of the wavelength of the x-rays. This relationship is known as Bragg's Law, which is illustrated in Figure 9, and it is defined as

$$n\lambda = 2d \sin\theta$$

where *n* is an integer multiple and λ is the wavelength of the x-rays.

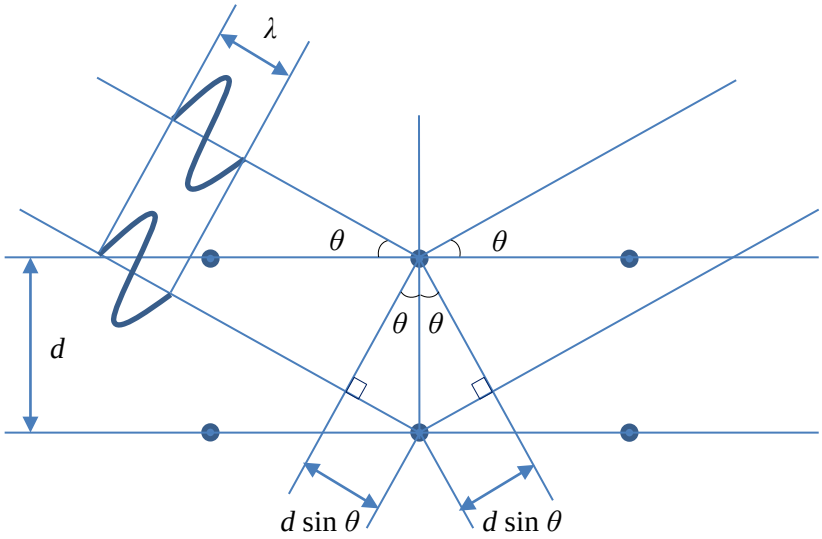

Figure 9. Illustration of Bragg's Law

Typically the x-ray radiation is fixed to a known, clean x-ray source (typically Cu-Kα for battery materials research), and the incident angles are scanned for diffraction peaks, which resolves as the x-ray diffraction pattern. It is the diffraction pattern that is used to uniquely identify materials. In powder XRD, powder samples ideally have a random distribution of the crystalline orientation.

Of the pattern matching techniques used to identify materials, which can be qualitative in nature, Rietveld refinement can provide quantitative information on the structures by fitting PXRD patterns generated though simulation and refining the fit through structural parameters until the errors are minimized. The goodness-of-fit parameters that judge the quality of the fitting include coefficient of determination, R^2, and the weighted profile R-factor, R_{wp}. Issues such as overfitting can skew the interpretation of the results and lead to erroneous conclusions, and physical evidence/measurements in conjunction with Rietveld refinement should be relied on when available.

In modeling the PXRD patterns, the intensity of the diffraction peaks is related to the structure factor by

$$I_{hkl} \propto |F_{hkl}|^2 ,$$

where *I* is the intensity of the diffraction peak and *F* is the structure factor for the (*hkl*) reflection. The structure factor is related to the atomic positions of the materials by

$$F_{hkl} = \sum_N f_N \exp[2\pi i \, (hx_N + ky_N + lz_N)] ,$$

where *f* is the atomic scattering factor and *x*, *y*, *z*, are the coordinates for the *N*th atom. Other factors affecting the intensity of the peaks include polarization, multiplicity, Lorentz, absorption, and temperature factors.

Peak broadening also arises from a number of factors, and typically indicates irregularity or defects in the materials. The Scherrer equation based on the full-width half-maximum (FWHM) of a diffraction peak gives an estimate of crystallite sizes by

$$XS_{hkl} = \frac{0.9\lambda}{\beta_{hkl} \cos \theta_{hkl}} ,$$

where *XS* is the crystallite size, λ is the wavelength of the radiation, β is the FWHM, and θ is the Bragg angle for the (*hkl*) reflection. Uniform and non-uniform strain can also affect the broadening as well as shifts in the diffraction peaks. Anisotropic size effects and stacking faults that contribute to broadening of select diffraction peaks have also been modeled and are implemented in various simulation and refinement programs [34, 38]. Effects from the instrument, the mounting, and environment of the sample are captured by instrumental broadening profiles, zero-shift, and background fitting, typically to Chebyshev polynomials. All of these factors can be refined to extract information about crystalline materials.

2.3.2 Electrochemical Impedance Spectroscopy

Electrochemical impedance spectroscopy (EIS) is a technique used to study the electrical properties of materials and kinetic mechanisms in electrochemical systems. It measures the dynamic current response to a small perturbation to the system, typically a voltage signal (±10 mV) for a specific range of frequencies. Depending on the frequency range of the signal, different phenomena that occur in electrochemical systems can be studied. Electronic and ionic transport behavior can be characterized in the high frequency range. Charge-transfer that occurs at the electrolyte and electrode interfaces can be characterized at a lower frequency range. Mass transport phenomena (diffusion) can be characterized at even lower frequency ranges. The current response, $I(t)$, changes in terms of phase shift and amplitude with respect to the applied voltage signal, $E(t)$, such that

$$E(t) = E_0 \cos(\omega t)\,,$$

$$I(t) = I_0 \cos(\omega t - \phi)\,,$$

where E_0 is the maximum amplitude of the voltage signal, I_0 is the maximum amplitude of the current response, ω is the angular frequency of the signal, t is the time, and ϕ is the phase shift in the response. Impedance, Z, is the ratio of the voltage signal to the current response, such that

$$Z = \frac{E}{I} = Z_0 \frac{\cos(\omega t)}{\cos(\omega t - \phi)}\,,$$

where Z_0 is the maximum amplitude of the impedance. Where resistance for direct current circuits only has a magnitude, impedance for alternating current circuits has a magnitude and a phase for characterizing the opposition of current flow in a circuit to an applied voltage.

Impedance can be expressed as a complex function by Euler's relationship,

$$\exp(jx) = \cos x + j \sin x\,,$$

where j is defined as $\sqrt{-1}$ and x is a real number. The voltage signal is then rewritten as

$$E(t) = E_0 \exp(j\omega t)\,,$$

and the current response is rewritten as

$$I(t) = I_0 \exp(j(\omega t - \phi))\,,$$

which gives the complex impedance

$$Z(\omega) = \frac{E}{I} = Z_0 \exp(j\phi) = Z_0(\cos\phi + j\sin\phi)\,.$$

Expressing the impedance as a complex function is useful for modeling the behavior of electrochemical systems using electrical circuit elements to form an equivalent circuit model. The simplified Randles circuit shown in Figure 10 is a common equivalent circuit for modeling the impedance response for a single electrochemical reaction. It is composed of a resistor and a capacitor complex in parallel (a Voigt element), which is in series with another resistor. Each circuit element is characterized by an impedance response, which combine for an overall impedance for the entire circuit. For circuit elements connected in series, the impedance is additive by

$$Z_{series} = Z_1 + Z_2 + \cdots\,.$$

For circuit elements connected in parallel, the inverse of the impedance is additive by

$$\frac{1}{Z_{parallel}} = \frac{1}{Z_1} + \frac{1}{Z_2} + \cdots\,.$$

The impedance response for the most common circuit elements is listed in Table 6.

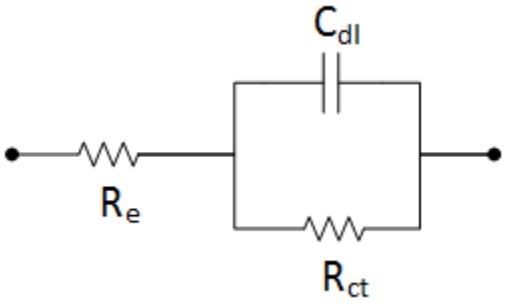

Figure 10. Simplified Randles equivalent circuit for modeling a single electrochemical reaction

Table 6. Impedance response of common circuit elements

Circuit Element	Impedance
Resistor	$Z_R = R$
Capacitor	$Z_C = \frac{1}{j\omega C}$
Inductor	$Z_L = j\omega L$
Constant Phase Element	$Z_{CPE} = \frac{1}{Y_0(j\omega)^{\alpha}}$
Warburg, Infinite	$Z_{W,inf} = \frac{1}{Y_0\sqrt{j\omega}}$

The overall impedance response for the simplified Randles circuit is given by

$$Z_{eq} = R_e + \frac{R_{ct}}{1 + j\omega R_{ct} C_{dl}},$$

where R_e represents the ohmic resistance of the electrolyte, R_{ct} represents the charge-transfer resistance for the electrochemical reaction at the electrode surface, and C_{dl} represents the double layer capacitance of the electrode. A typical Cole-Cole plot, which plots the imaginary impedance against the real impedance, for the corresponding equivalent circuit is shown in Figure 11, with real impedance decreasing with increasing angular frequency. The equivalent circuit can be used to model impedance spectra that show similar semi-circle behavior by using

regression fitting techniques to obtain the parameters for quantifying and interpreting the electrical and ionic transport phenomena.

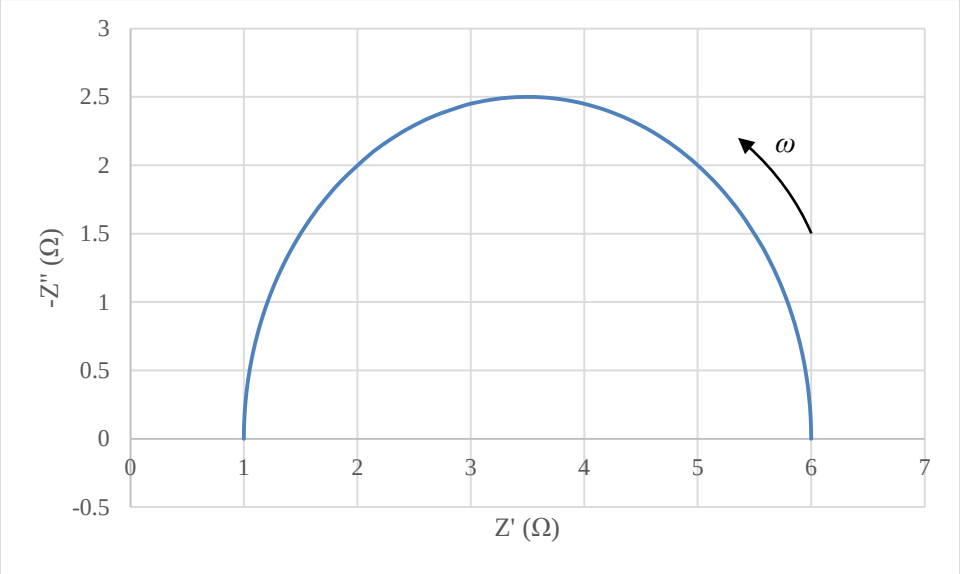

Figure 11. Cole-Cole plot for a simplified Randles circuit with R_e = 1 Ω, R_{ct} = 5 Ω, C_{dl} = 0.01 F

The transport processes that occur in a battery electrode include both kinetic and diffusion processes, and is typically represented by the Randles circuit shown in Figure 12. Z_w is the infinite Warburg impedance contribution due to diffusion through stagnant conditions. Inclusion of Z_w in the overall impedance response model yields

$$Z_{eq} = R_e + \frac{\left(R_{ct} + {}^{1}\!/_{Q_0\sqrt{j\omega}}\right)}{1 + j\omega C_{dl}\left(R_{ct} + {}^{1}\!/_{Q_0\sqrt{j\omega}}\right)},$$

where Q_0 is the magnitude of the admittance due to the Warburg diffusion at ω = 1 s^{-1}. Q_0 is related to the diffusion coefficient of the reactive species by the expression

$$Q_0 = \frac{1}{\frac{RT}{n^2F^2A}\left(\frac{1}{D_O^{1/2}c_O^b} + \frac{1}{D_R^{1/2}c_R^b}\right)},$$

where R is the gas constant, T is the temperature, n is the number of electrons involved in the electrochemical half reactions, F is Faraday's number, A is the surface area of the electrodes, D is the diffusion coefficient of the species, and c^b is the bulk concentration of the species, where the subscripts O denotes the oxidized form of the species and R denotes the reduced form.

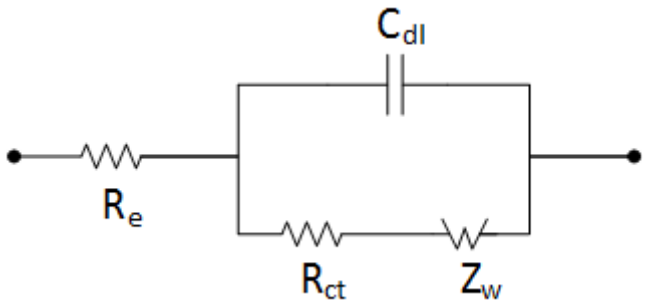

Figure 12. Randles circuit for modeling electrochemical behavior with diffusion

The Cole-Cole plot of the impedance spectra for a Randles-type cell is shown in Figure 13. The plot shows three distinct regions that correspond to the different types of transport phenomena: ion and electron transport (ohmic/electrolyte), charge transfer at the electrochemical interfaces, and mass transport (diffusion). Ohmic resistance is characterized in the high frequency range, and it consists mainly of losses due to electrical contact resistance and ionic resistance of the electrolyte. The contribution from the electrolyte in most cases dominates the ohmic resistance. The ohmic resistance behavior is modeled by a simple resistor following Ohm's law, such that

$$Z = R_e \, .$$

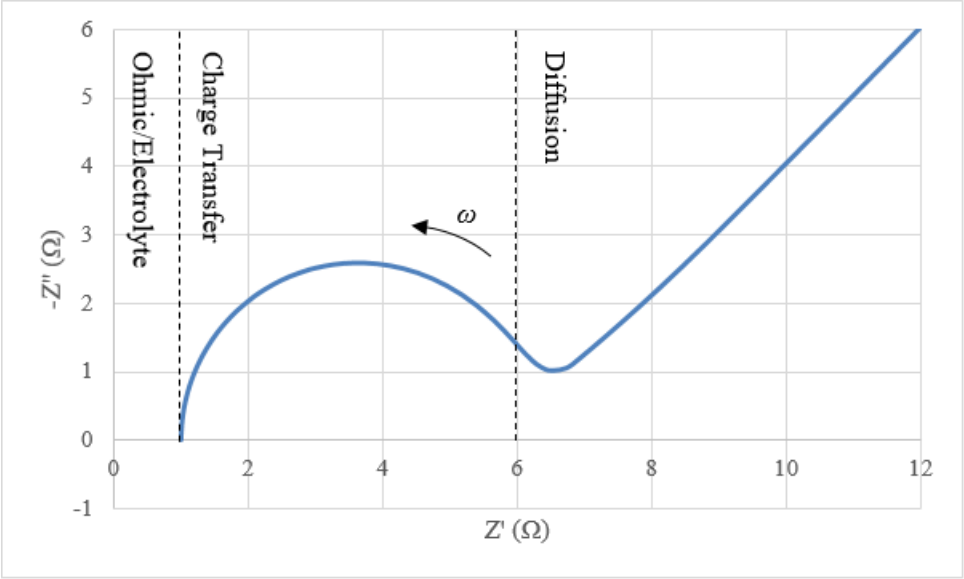

Figure 13. Cole-Cole plot for a Randles circuit with R_e = 1 Ω, R_{ct} = 5 Ω, C_{dl} = 0.01 F, and Q_0 = 1 F/s$^{1/2}$

The charge-transfer resistance can be extracted from fitting the impedance spectra in EIS measurements to an equivalent circuit, but it can also be measured experimentally. The Butler-Volmer equation describes the relationship between the current and the overpotential of the electrode,

$$i = i_0 \left[\exp\left(\frac{\alpha_a nF\eta}{RT}\right) - \exp\left(-\frac{\alpha_c nF\eta}{RT}\right) \right],$$

where i is the current, i_0 is the exchange current, α_a is the anodic charge-transfer coefficient, α_c is the cathodic charge-transfer coefficient, n is the number of electrons in the reaction, F is the Faraday constant, η is the overpotential, R is the gas constant, and T is the temperature. Within a small overpotential range of ±10 mV, the polarization measurements are linear and follow the relationship

$$i = \frac{i_0 F\eta}{RT}.$$

The exchange current i_0 is related to the charge-transfer resistance by

$$R_{ct} = \frac{RT}{nFi_0}.$$

Discrepancies between the two methods can depend on the linearity of the polarization regime.

Diffusion coefficients can similarly be modeled and measured. Potentiostatic discharge experiments discharge an electrode at a constant overpotential, tracking the current response with respect to time, typically over 3 or more hours. The current-time response can be fit to a semi-logarithmic curve following the equation

$$\log i = \log\left(\frac{6FD}{da^2}(C_0 - C_s)\right) - \frac{\pi^2}{2.303}\frac{D}{a^2}t\,,$$

where *i* is the specific diffusion current, C_0 is the initial hydrogen concentration in the bulk of the alloy, *Cs* is the hydrogen concentration on the surface of the alloy particles, *a* is the alloy particle radius, *d* is the density of the hydrogen storage alloy, *D* is the bulk diffusion coefficient, and *t* is the discharge time.

The double layer capacitance extracted from the equivalent circuit model is related to the surface area of the electrode following the equation

$$C_{dl} = \frac{\varepsilon A}{d},$$

where ε is the dielectric constant of the electrolyte, *A* is the surface area of the electrode, and *d* is the distance between the electrodes. Because they are proportional, C_{dl} gives a relative indication of the surface area of the electrode.

CHAPTER 3. COMPUTATIONAL STUDY OF C14/C15 LAVES PHASE $Mg(Cu_{1-x}Zn_x)_2$ ALLOYS

Semi-empirical tight-binding calculations have been used to model the stable C14/C15 ground state structures of AB_2 metal hydride alloys based on the calculated energies of the C14/C15 structures of $TiFe_2$ and changing the number of electrons per AB_2 unit. Our initial DFT calculations to model the C14 and C15 ground state structures of various known AB_2 alloys and show a good correlation to the semi-empirical model. However, industrial applications of AB_2 alloys consist of multi-element compositions, and refining the average electron concentration requires more complex structures with multiple calculations. We use the $Mg(Cu_{1-x}Zn_x)_2$ alloy system to refine the C14/C15 stability model, and determine the necessary calculations and computational accuracy required to extend the model.

3.1 Background

Laves phases are a family of intermetallic compounds that share AB_2 stoichiometry and crystallographically-related structures that differ only in the stacking of a shared fundamental structure unit [6]. They are represented by three main polytypes known as C14 (hexagonal $MgZn_2$), C15 (face-centered cubic $MgCu_2$), and C36 (hexagonal $MgNi_2$), and two or more polytypes may exist as equilibrium phases in multi-element alloy systems. Laves phases are important materials in hydrogen storage applications as well as electrochemical applications. C14 and C15 in particular contribute to specific properties in nickel-metal hydride (NiMH) battery applications. C15 phase appears to contribute to capacity, while C14 phase appears to extend cycle life [16]. The ability to determine C14/C15 structures from multi-element alloy compositions will aid in the design of hydrogen storage alloys for NiMH battery applications.

The alloy formulae for NiMH battery applications are of course much more complicated than the systems of study. As an example, the alloy $Ti_{12}Zr_{21.5}V_{10}Ni_{40.2}Co_{1.5}Cr_{8.5}Mn_{5.6}Al_{0.4}Sn_{0.3}$ is proposed to give a good balance of electrochemical performance [16]. Other parameters such as cooling rates and casting techniques can also affect the phase composition of alloys compounds, but we need a starting point for our studies. Research groups have attempted to correlate parameters such as the radii ratio between A and B elements. Johnston and Hoffman proposed a model based on the average electron concentration (*e/a*), which shows good correlation for AB_2 alloys based on the first-row transition metals [23]. The sample alloy formula has an *e/a* value of 6.91 and is experimentally shown to be C14 rich. According to the model, the sample alloy formula has 20.73 valence electrons per AB_2 unit and would have C15 structure. The Zr from the second row transition metals tends to break this particular model, which uses a semi-empirical method based on A=Ti and B=Fe and predicts the structure with the lowest energy to be the stable ground state structure. Calculations using density functional theory (DFT) have been shown to predict the ground state stable structures for Laves phase alloys reliably [24], and we have some initial data that builds upon the reported model shown in Figure 14.

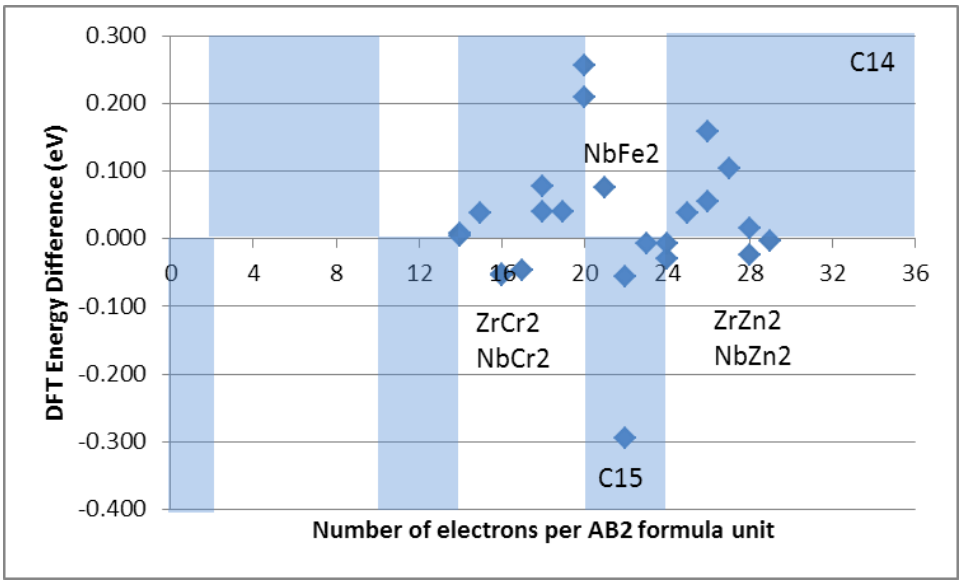

Figure 14. Preliminary DFT C14/C15 structure model for Laves phase AB2 alloys compared to semi-empirical model

The initial DFT results correctly calculate the second row transition metal-based alloys such as $ZrCr_2$, $NbCr_2$, and $NbFe_2$. It also correctly predicts the stable structure of the sample alloy formula from above. The shaded regions in the plot show the predictions from the Johnston and Hoffman semi-empirical model. Note that not all compositions in AB_2 stoichiometry form C14 or C15 structures. For example, TiV_2 forms body-centered cubic (BCC) structure and $MgNi_2$ forms C36 structure. We choose to include even the theoretical binary C14/C15 structures in the model in case there are multi-element compositions that may fall in the same *e/a* range. Using a binary, single AB_2 unit only allows an *e/a* step size resolution of 0.33. In order to get a smaller step size, we will need to calculate stable structures for A_2B_3X compositions (0.17 step size) or eventually A_4B_7X compositions (0.083 step size). These calculations will become more and more computationally expensive. In order to build upon our DFT model, we are interested in following the C14/C15 structure evolution of the $Mg(Cu_{1-x}Zn_x)_2$ system for x=0, 0.25, 0.5, 0.75, and 1. The stable ground state structures for $MgCu_2$ (C15) and $MgZn_2$ (C14) are shown below in Figure 15.

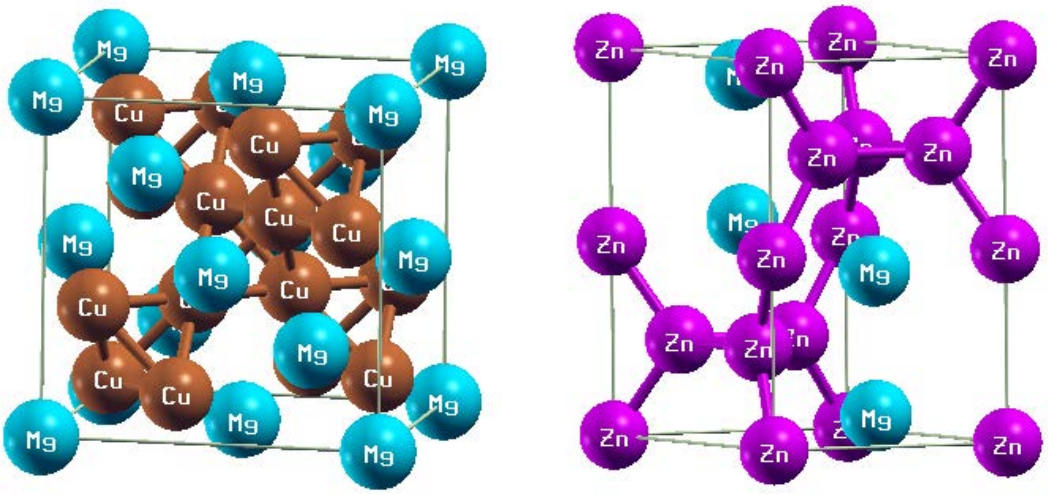

Figure 15. $MgCu_2$ (C15) and $MgZn_2$ (C14) crystal structures

The number of valence electrons in our Mg-Cu-Zn system corresponds to 24, 24.5, 25, 25.5, and 26 electrons per AB2 unit. Note that this corresponds to C14 structures in our DFT model, but the alloys in the 24-26 electron range are based on alloy compositions such as $TiNi_2$ and $ZrNi_2$ that do not thermodynamically form C14/C15 phases. We expect to refine the C14/C15 transition point so that we can apply the method to extend our DFT model.

3.2 Computational Methods

We used Quantum Espresso, a pseudopotential-based plane-wave DFT code, for our calculations [65]. The plane-wave basis set is useful for periodic systems like alloys and other solid-state systems where electrons are described using band structures. We used XcrySDen to view and confirm the crystal structures [66]. The Perdew-Burke-Ernzerhof (PBE) parameterization of the generalized gradient approximation (GGA) is used to evaluate the exchange-correlation energy. The PBE functional is shown to be reliable for transition metal systems [62]. The alloy and bulk structures are known to be non-magnetic so spin correlation was not included in the calculations.

The pseudopotentials used in the calculations are downloaded from the open-source GBRV ultra-soft pseudopotential library that has been tested for high throughput and good transferability [67]. We only report energy differences so that the "frozen core" approximation using the same energy cutoff cancels out.

Convergence studies were conducted to determine the energy cutoff level of the plane-waves used in the basis set. We varied the energy cutoff from 20 Ry to 60 Ry and calculated the energy for each bulk element. The ground state energy difference between C14 and C15 structures can differ by only 0.01eV/AB_2 unit, and so we chose a cutoff parameter for an energy convergence of at least 0.001eV/AB_2. The convergence in the difference in energy should be better.

The kinetic energy cutoff for the charge density was determined in a similar manner. These energy cutoffs are typically a function of the pseudopotentials, and the energy cutoffs for the alloys are chosen as the highest cutoff values of the constituent elements.

Convergence studies with respect to the number of k-points and smearing width is also necessary to ensure the accuracy requirements of the calculations. We varied the Monkhorst-Pack k-point grid from 9x9x9 to 21x21x21 with an artificial electronic temperature (Methfessel-Paxton smearing) range from 0.008 to 0.05 Ry [68, 69]. K-point convergence is specific to each system and does not necessarily carry over from bulk systems to alloy systems.

Once the convergence criteria were fixed, geometry optimizations were conducted on each structure using the Broyden–Fletcher–Goldfarb–Shanno algorithm with a force convergence threshold of 1.0d-6 Ry/Bohr [70]. We optimize C14 and C15 structures for each composition (and each composition configuration) and compare the energies. The structure with the lowest free energy will be the stable state structure for the composition at a given temperature

and pressure. We assume that as a solid state structure, the volumetric and entropic contributions will be small, allowing us to look at the ground state energies to determine the stable structures. We will also assume that the electronic contributions will dominate the vibrational contributions. Vibrational contribution calculations are more computationally expensive in solid state structures than in molecular structures, and due to limited computational resources, they are neglected in this study.

3.3 Results and Discussion

3.3.1 Convergence

Convergence studies of bulk Mg (hexagonal close packed), Cu (face centered cubic), and Zn (hexagonal close packed) with respect to the plane-wave energy cutoff (ecut) are shown below in Figure 16. Mg and Zn were able to reach the 0.001 eV/atom convergence at 45 Ry and 55 Ry, respectively, but Cu was not able to meet the convergence with tests up to 60 Ry. We have chosen an energy cutoff of 55 Ry for Cu to further test for convergence. The other convergence parameters are shown in Table 7. They converge to at least the ecut convergence or better.

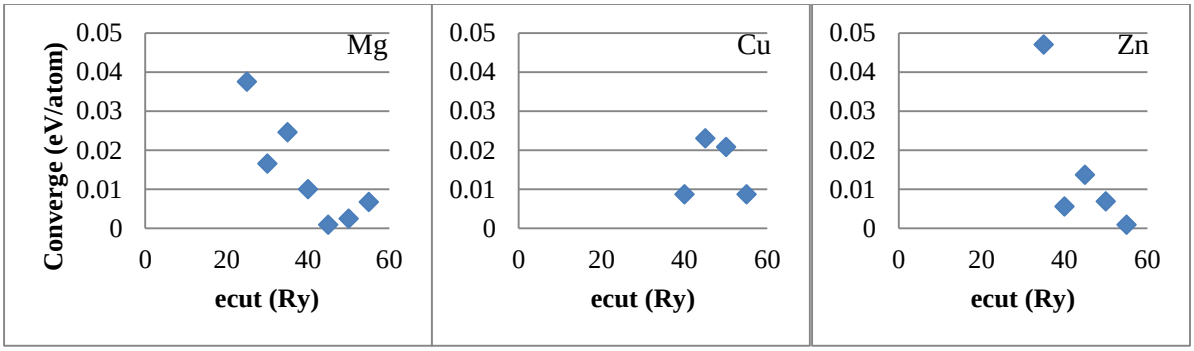

Figure 16. Convergence studies with respect to plane-wave energy cutoff (ecut) for Mg, Cu, and Zn

Table 7. Convergence parameters for Mg, Cu, and Zn

	Mg_{hcp}	Cu_{fcc}	Zn_{hcp}
ecut (Ry)	45	55	55
ecutrho (Ry)	540	660	660
nkpt	12	12	15
smearing (Ry)	0.03	0.05	0.05

3.3.2 Bulk Parameters

In order to determine the suitability of our calculations for the Mg-Cu-Zn system, we have calculated the equilibrium lattice constants, cohesive energy (E_{co}), and bulk modulus (B_o) for bulk Mg, Cu and Zn and compare to experiment. We have used the convergence criteria in Table 7. The energy calculations do not include the zero point energy correction, but it should be sufficient for gauging the suitability of our convergence criteria and calculation setup. Equilibrium lattice constants are taken from geometry optimization calculations. Cohesive energy is the energy difference between the bulk and its constituent atoms on a per atom basis in a unit cell. In order to calculate single atom energies, the atoms were placed in a sufficiently large box (10x10x10 $Å^3$) so that the periodic images do not interact. Spin-polarization was also accounted for. The bulk modulus is a measure of a material's response to uniform compression, and is given by the equation:

$$B = -V\left(\frac{\partial^2 E}{\partial V^2}\right)_T$$

We calculate energies for a range of volumes around the equilibrium point, and fit the data to the second order Birch Equation of State to obtain the bulk modulus. These calculations and the reported experimental values are provided in Table 8.

Table 8. Calculated and experimental bulk parameters for Mg, Cu and Zn

	Mg_{hcp}		Cu_{fcc}		Zn_{hcp}	
	Calc	Exp.	Calc	Exp.	Calc	Exp.
a (Å)	3.20	3.21[a]	3.63	3.60[b]	2.63	2.66[d]
c (Å)	5.14	5.21[a]	-	-	5.11	4.95[d]
E_{co} (eV)	1.51	1.51[a]	3.56	3.49[c]	1.11	1.35[c]
B_o (GPa)	36.0	35.4[a]	139.9	142[b]	74.7	75[d]

[a] Reference [71]
[b] Reference [72]
[c] Reference [58]
[d] Reference [73]

The lattice parameters are within 0.3-3% of the experimental values. The cohesive energy ranges from <0.01% to 18%, and bulk moduli are within 2%. This is expected for GGA methods. Our maximum absolute error in cohesive energy is 0.24 eV, which is within the average 0.3 eV reported for GGA [58].

3.3.3 $MgCu_2$ and $MgZn_2$ Binary Alloys

Convergence studies for the binary alloys $MgCu_2$ and $MgZn_2$ with respect to energy cutoff are shown in Figure 17. The best convergence is 0.01 eV/AB_2, which is on the same order as the energy difference of C14/C15 structures. We proceed with the structure optimization calculations because the convergence in the energy difference should be better. Our convergence studies specify an energy cutoff of 60 Ry, a kinetic energy cutoff of 720 Ry, and 12x12x12 k-point grid with 0.02 Ry width smearing. C14 and C15 structure optimizations were conducted for each composition.

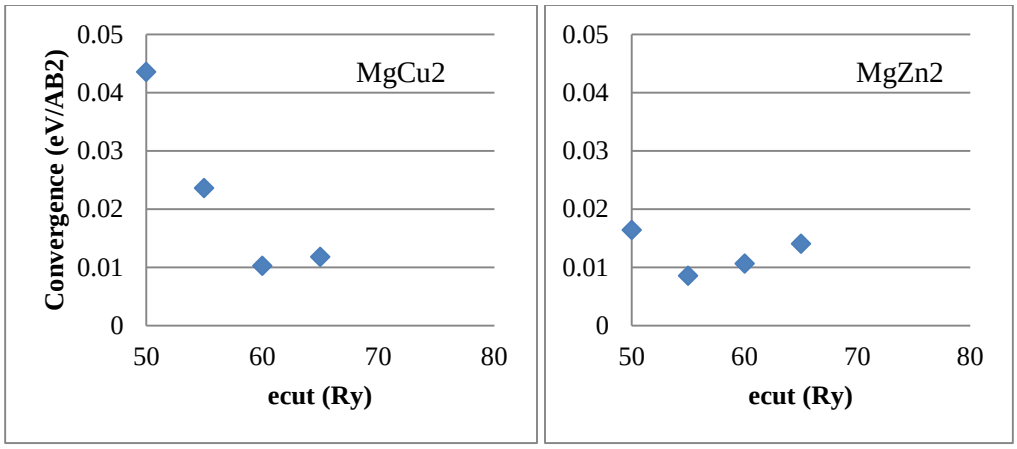

Figure 17. Convergence studies with respect to plane-wave energy cutoff (ecut) for $MgCu_2$ and $MgZn_2$ alloys

The optimized structure parameters for $MgCu_2$ and $MgZn_2$ and the data are compiled in Table 9. The energy difference between C14/C15 structures at each composition is defined as $\Delta E = E_{C15} - E_{C14}$ per AB2 unit. A positive ΔE indicates a stable C14 structure, and a negative ΔE indicates a stable C15 structure. The calculations correctly calculate the ground state structure for both compositions. The differences in energy are -0.0130 eV/AB_2 for $MgCu_2$ and 0.0270 eV/AB_2 for $MgZn_2$.

Table 9. Optimized structure calculations for $MgCu_2$ and $MgZn_2$ alloys

	$MgCu_2$	$MgZn_2$
a (Å)	7.032	5.178
c (Å)	-	8.415
ΔE (eV/AB_2)	-0.0130	0.0270
Structure	C15	C14

In order to obtain higher confidence in the cutoff parameters, we conducted a convergence study for the *energy difference* in C14/C15 structures. The convergence data are shown in Figure 18, and the data show better convergence in the energy difference than in absolute energy (9e-6 eV/AB_2 at 40 Ry). We choose 40 Ry for the plane-wave energy cutoff and 480 Ry for kinetic energy cutoff for charge density for the $Mg(Cu_{1-x}Zn_x)_2$ system studies. In the

interest of time and limited computing resources, we choose a k-point grid of 8x8x8 and 0.02 Ry smearing for the studies, which converges the energy difference to 0.001 eV/AB_2.

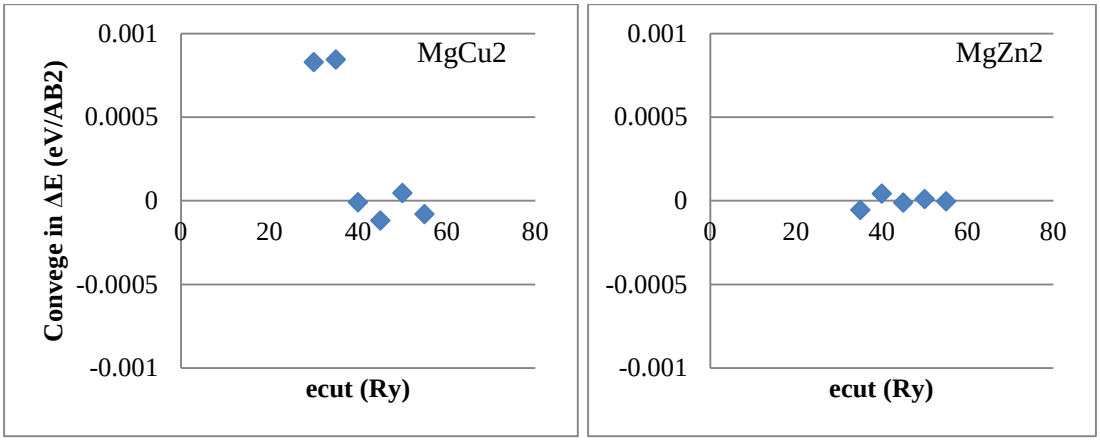

Figure 18. Convergence studies for C14/C15 energy difference with respect to plane-wave energy cutoff (ecut) for $MgCu_2$ and $MgZn_2$ alloys

3.3.4 $Mg(Cu_{1-x}Zn_x)_2$ Structures

The ternary alloy studies are not as straight forward as the binary alloy studies. There are four AB_2 units in the C14 primitive cell and two AB_2 units in the C15 primitive unit cell. In order to optimize the Mg_2Cu_3Zn composition, we will need to substitute two Cu atoms for Zn atoms in the C14 primitive unit cell. Due to its $P6_3/mmc$ space group symmetry, there are two distinct B sites, which we will denote as B1 and B2. The Zn atoms can occupy two B1 sites, one B1 and B2 site each, or two B2 sites. We will need to optimize each configuration for each composition. For the C15 primitive unit cell, we only need to substitute one Cu atom for Zn, and all B sites are equivalent. The lowest energy configuration for a specific composition will be the stable ground state structure. We have repeated this procedure in a similar manner for each composition and obtained the optimized structure parameters in Table 10.

Table 10. Optimized structure calculations for $Mg(Cu_{1-x}Zn_x)_2$ alloys

	$MgCu_2$	Mg_2Cu_3Zn	MgCuZn	Mg_2CuZn_3	$MgZn_2$
a (Å)	7.032	7.108	5.096	5.084	5.178
c (Å)	-	-	8.131	8.405	8.415
ΔE (eV/AB_2)	-0.0130	-0.0036	0.0132	0.0080	0.0270
# e^- per AB_2	24.0	24.5	25.0	25.5	26.0
Structure	C15	C15	C14	C14	C14

Shannette and Smith provide a phase diagram for the $MgCu_2$-$MgZn_2$ system based on work from Klee and Witte [74, 75]. There is a very narrow solubility range for C14 phase (~99-100% mol. $MgZn_2$) that is nearly pure $MgZn_2$. In order to model the transition, it would require constructing supercells for the calculation. The phase diagram also denotes a composition range that forms C36 structure (~73-88% mol. $MgZn_2$), and according to the diagram Mg_2CuZn_3 forms C36 structure, not C15 (~0-63% mol. $MgZn_2$). If we are to include the C36 structure into our calculations, we should see that the C36 structure is lower energy than C15 for the Mg_2CuZn_3 composition. Overall we see good agreement where the electronic energies of the C14/C15 structures have a large energy difference. We get discrepancies once the electronic energies become more equal, suggesting that vibrational contributions play a larger role in the C14/C15 transition point. C15 has higher symmetry than C14 structure. C15 structure therefore has less degrees of freedom and less vibrational energy than C14 structure. When the electronic energies are equal, then C15 should be predicted as the stable ground state structure as indicated in the $MgCu_2$-$MgZn_2$ phase diagram.

3.4 Summary

This study examines the necessary calculations and computational accuracies required for C14/C15 Laves phase structure determination. Due to the computational expense in performing vibrational energy contributions for solid state structures, we have made the assumption to neglect vibrational energy contributions. While this assumption holds for compositions with

large electronic energy differences, it does not hold for compositions where the electronic energies are very close. The vibrational contributions become more important in these cases around the C14/C15 transition point. Future resource expansion can allow investigation into the vibrational contributions. The number of k-points in this study was reduced in order to compute all of the necessary structures in the interest of time, so increasing the k-points is also of interest. Supercells that allow investigation of other configurations of a composition also allows a more rigorous study of the system.

CHAPTER 4. STRUCTURE AND PCT HYSTERESIS IN $LaNi_5$ AND $TiMn_2$ ALLOYS

Most metal hydride (MH) alloys used in commercial nickel/metal hydride (NiMH) battery negative electrodes are of the AB_5 and A_2B_7-based superlattice alloy varieties, both containing rare-earth (RE) elements such as La, Ce, Pr, Nd, etc. In 2010, there was a sharp price spike in RE metals due to the global supply falling under much of China's control. The RE market, and therefore the NiMH battery materials cost, continues to be prone to price volatility. Laves phase-based AB_2 metal hydride (MH) alloys avoid this market volatility issue by eliminating RE elements from the composition. On one hand, AB_2 alloys offer relatively higher energy density at lower cost in NiMH batteries [76, 77]. However, on the other hand, they also present a different set of challenges for researchers: the alloys are multi-phase in nature composed of the main Laves phases with C14, C15, and C36 structures and non-Laves secondary phases, such as Zr_7Ni_{10}, Zr_9Ni_{11}, ZrNi, TiNi, etc. [78, 79]. The main Laves phases are crystallographically similar, but are functionally different in negative electrode materials [16, 17]. Modern AB_2 alloys used in NiMH batteries are mainly C14-predominant, and they are optimized around multiple series of compositions based on electrochemical performance [80, 81]. It is of interest for researchers to investigate the correlation between composition, structure, and electrochemical performance of C14 MH alloys. Calculations from first principles allow us to isolate and study the C14 phase in an accelerated manner: in particular, the relationship between structure, pressure-concentration-temperature (PCT) isotherm hysteresis, and the cycle stability of electrodes.

4.1 Background

Factors that affect the cycle stability of the negative electrode active materials for NiMH batteries include corrosion, oxidation and pulverization [82]. It has been studied in $MmNi_5$-based

alloys (Mm = misch-metal) that an oxide layer forms on the surface of the alloy particles during cycling as the charge-discharge cycles reduce the alloy particles below the crystal grain size [83-86]. Additives that promote the formation of a more protective oxide layer can reduce the exposure of fresh surfaces that contribute to gradual capacity loss. Increasing the toughness of the alloys in order to reduce pulverization can also increase the cycle stability. The cycle stability of the alloys can be correlated to measurements such as pure volume expansion-contraction and the relative average particle size after cycling [83, 87]. The average particle size after cycling has also been correlated to the hardness of the alloy [87], as well as the hysteresis of hydrogen absorption-desorption isotherms [88], a measure of irreversible energy losses in the process. Provided that the surface layer forms a protective barrier against corrosion and oxidation to the KOH electrolyte while maintaining good electrochemical reaction, the gaseous-phase properties such as PCT isotherm hysteresis can give an indication of the cycle stability and possibly the degree of pulverization. Additives such as Al [83, 87], Co [83, 87], Si [83, 89, 90], Ti [89] and Zr [91] have been documented to improve cycle stability in AB_5-based NiMH batteries, but they also have effects on the formation of the protective surface layer as well as on the electrochemical capacity. Gaseous-phase studies isolate the materials from electrolyte effects, and show that Al [92-94], Si [95], and Sn [96, 97] specifically improve hydrogen storage capacity degradation in $LaNi_5$-type alloys. All three additives show little to no hysteresis and no lattice defects in initial gaseous-phase cycling [98, 99]. Hysteresis in $MmNi_5$ alloy is much higher than in $LaNi_5$, and a single additive such as Al lowers the hysteresis in both types of AB_5 alloys. Al-addition to $MmNi_5$ does not bring the hysteresis below the level measured in pure $LaNi_5$, but a combination of additives in $MmNi_5$ can essentially eliminate the hysteresis [100].

According to a study correlating structural properties with the electrode performance, $MmNi_5$-based alloys with a larger *c/a* ratio tend to show smaller hysteresis [101, 102].

In addition to the research on AB_5 MH alloys, there is also research activity looking at the relationship between structure, PCT hysteresis and the degree of alloy pulverization in C14 Laves phase-based AB_2 alloys. A three-part series of papers investigating PCT hysteresis in $ZrCr_2$ and $(Ti,Zr)(V,Mn,Cr,Ni)_2$-based alloys is available [103-105]. Part 1 of the series of papers showed a correlation between mechanical stability of the alloys to both PCT hysteresis and the ratio of the lattice parameters measured for the AB_2 alloys [103]. Alloys with a smaller *c/a* ratio tended to have smaller hysteresis between absorption and desorption isotherms and showed less pulverization with gaseous-phase cycling. Part 2 of the papers related the gaseous-phase results of C14 Laves phase alloys in Part 1 to cycle life performance in the electrochemical environment of NiMH batteries [104]. Part 3 of the papers developed an empirical formula predicting *a/c* ratio from a C14 Laves phase alloy formula composition through a modified average valence electron concentration (*e/a*) that then can be correlated to the PCT hysteresis [105].

This paper takes a computational approach to studying alloy structure in substituted AB_5 and C14 AB_2 metal hydride alloys. Computationally, we can look at volume and lattice parameter changes with hydrogen insertion, specifically of the host alloy and a near dilute solid solution α-phase hydride. The $LaNi_5$ system is well studied experimentally and computationally [106-112], and it serves as a benchmark for our current study. Structural benchmarks are also available for the $TiMn_2$ system [113-115]. We present the alloy structures and near α-phase hydride lattice expansion calculated for substituted $LaNi_5$ and $TiMn_2$ alloy systems, analyze the relationship between the host structure and the initial hydrogen absorption lattice expansion, and compare the calculated results to experiments reported in literature.

4.2 Crystal Structure

Both the AB_5 alloy family ($LaNi_5$ and $MmNi_5$) and AB_2-C14 Laves phase alloy family share hexagonal unit cell structures. $LaNi_5$ ($CaCu_5$-type structure) belongs to the *P6/mmm* space group with La occupying *1a* sites and Ni occupying *2c* (on the same basal plane as 1a) and *3g* (on the half-plane between two basal plane) sites. There is one formula unit per unit cell, and experimental lattice parameters are reported to be a = 5.017Å and c = 3.986Å (c/a ratio=0.794) [116]. Initial preferential hydrogen sites are the *6i* sites [111, 112]. C14 structure belongs to the $P6_3/mmc$ space group with A atoms occupying *4f* sites and B atoms occupying *2a* (on the basal plane) and *6h* (on the half plane) sites. There are 4 formula units per unit cell in C14, and experimental lattice parameters for $TiMn_2$ are reported to be a = 4.820Å and c = 7.915Å (c/a ratio = 1.642) [117]. The initial preferential hydrogen sites are the *12k* or 6*h* sites [113, 118, 119]. Unit cells for $LaNi_4Cr$ and Ti_4Mn_7Cr are shown in Figure 19, respectively, illustrated using VESTA software [120].

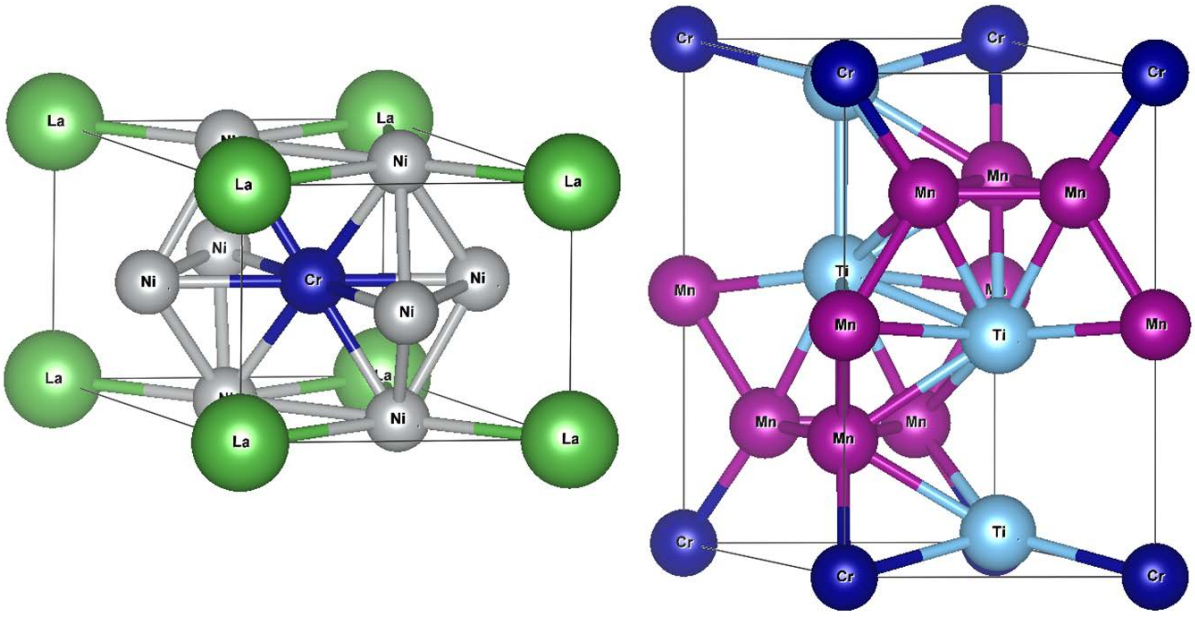

Figure 19. Unit-cell crystal structures for LaNi4Cr and Ti4Mn7Cr

4.3 Computational Methods

Electronic structure calculations were performed using the plane-wave-based density functional theory code implemented in Quantum Espresso [121] and ultra-soft pseudopotentials from the GBRV pseudopotential library [122]. The exchange-correlation potential applied the Perdew-Burke-Ernzerhof (PBE) version of the generalized gradient approximation [123]. The recommended plane-wave cutoff energy of 40 Ry and charge-density cutoff energy of 120 Ry allowed convergence within 1×10^{-5} Ry/atom of the energy. A Methfessel-Paxton smearing width of 0.02 Ry with a Monkhorst-Pack k-point grid of at least 12×12×12 also met convergence criteria with reasonable speed [68, 69]. Spin-polarization was taken into account for $LaNi_5$-based compositions.

Cell structural optimizations for a given composition and structure were conducted by first performing an ion relaxation calculation on a fixed cell shape, fixing the nuclear coordinates and relaxing the cell volume, and then fixing the volume and relaxing the *c/a* ratio. The procedure was iterated until forces were minimized to below 1×10^{-3} Ry/Å and the minimum energy was converged to below 1×10^{-5} Ry/atom. The optimized lattice parameters for each composition and structure at the ground state were taken to be at the minimized energy.

4.4 Results and Discussion

Structures were optimized for alloy systems $LaNi_4X$ and Ti_4Mn_7X and their partial hydrides $LaNi_4XH$ and Ti_4Mn_7XH in a 1×1×1 cell, where *X* = Al, Si, Sc, Ti, V, Cr, Mn, Fe, Co, Ni, Cu, Zn, Zr, and Sn. Substitution elements in the same row, such as the first-row transition metals, allow us to study the effects of atomic size and *e/a*. Ti, Zr, Si, and Sn elements allow us to fix the *e/a* and examine size effects. We calculate all of the structures assuming *X* substitutes in one of two possible B sites and compare their relative energies, but it is possible that the

calculated structure may not be the most stable thermodynamically. For example, $ScNi_5$ exists in the $CaCu_5$ structure, and Zr and Ti have some solubility for La in $LaNi_5$ [89, 124]. We may infer by size that Sc, Zr, and Ti substitute for La rather than Ni, but we include the calculations for completeness. Similarly, Si and Sn have reported solubilities for average compositions up to approximately $LaNi_{4.5}X_{0.5}$ [125, 126], but the calculations for $LaNi_4Si$ and $LaNi_4Sn$ are included. For Ti_4Mn_7X, $ZrMn_2$ also exists in the C14 structure, but Ti shows some solubility for Mn [119]. Of the two possible substitution sites *2c* and *3g* for $LaNi_5$, the *3g* site is the most stable for all substitution elements except for Cu, which slightly prefers the *2c* site. This is in agreement with other experimental and computation studies. Of the *2a* and *6h* substitution sites for $TiMn_2$, the *2a* site is the most preferable for all elements except for V and Cr. The optimized lattice parameters and *c/a* ratio for all $LaNi_4X$ and Ti_4Mn_7X structures are listed in Table 11. There is a good agreement with experiment for the base structures $LaNi_5$ and $TiMn_2$ [116, 117]. There is also a good agreement with experiments that are available for substituted elements where X = Co, Cu, Fe, Mn, and Al for $LaNi_4X$ [110].

Table 11. Average valence electron concentration and structural parameters calculated for $LaNi_4X$ and Ti_4Mn_7X host alloys

	$LaNi_4X$				Ti_4Mn_7X			
X	*e/a*	*a* (Å)	*c* (Å)	*c/a*	*e/a*	*a* (Å)	*c* (Å)	*c/a*
Al	7.667	5.061	4.071	0.804	5.667	4.748	7.949	1.674
Si	7.833	5.032	3.981	0.791	5.750	4.742	7.809	1.647
Sc	7.667	5.204	4.163	0.800	5.667	4.815	8.077	1.677
Ti	7.833	5.123	4.095	0.799	5.750	4.804	7.900	1.644
V	8.000	5.085	4.029	0.792	5.833	4.788	7.806	1.630
Cr	8.167	5.070	4.048	0.798	5.917	4.766	7.782	1.633
Mn	8.333	5.063	4.062	0.802	**6.000**	**4.734**	**7.814**	**1.651**
Fe	8.500	5.041	4.016	0.797	6.083	4.707	7.866	1.671
Co	8.667	5.018	3.981	0.793	6.167	4.693	7.907	1.685
Ni	**8.833**	**5.004**	**3.985**	**0.796**	6.250	4.686	7.962	1.699
Cu	9.000	5.023	4.021	0.800	6.333	4.693	8.010	1.707
Zn	9.167	5.052	4.060	0.804	6.417	4.718	8.018	1.700
Zr	7.833	5.257	4.146	0.789	5.750	4.855	8.058	1.660
Sn	7.833	5.213	4.158	0.798	5.750	4.796	8.148	1.699

A single hydrogen atom was inserted into the unit cell for each composition and then optimized for structure. While the α-phase solid solution has reported a solubility limit up to $LaNi_5H_{0.5}$ [127], the lattice parameters calculated for $LaNi_5H$ is comparable to experimental values reported for the α-phase [128, 129], and we apply the same assumption for the $LaNi_4XH$ and Ti_4Mn_7XH systems. The preferential hydrogen sites are the *6i* site for $LaNi_5$ and the *12k* site for $TiMn_2$, but the preferential sites may change with the substitutions in $LaNi_4X$ and Ti_4Mn_7X. In addition, the positions of each type of site (e.g. the 6 positions of the 6*i* site) are no longer all identical due to the introduction of a third element into the composition. To study each of the possible sites for each composition requires optimizations of 300+ structures; instead we have opted to perform a full study of the hydrogen sites on some representative compositions, and we will assume that similar substitution elements will have similar preferential hydrogen sites. We have calculated the hydrogen insertion energy, E_{ins}, defined as

$$E_{ins} = E(A_mB_nXH) - [\ E(A_mB_nX) + 0.5E(H_2)\ ],$$

where $E(A_mB_nXH)$, $E(A_mB_nX)$, and $E(H_2)$ are the total energies calculated for each respective compound. A 10×10×10 $Å^3$ cell was used to calculate the total energy of the hydrogen molecule. The types of hydrogen sites and the E_{ins} for $LaNi_4Al$, $LaNi_4Co$, $LaNi_4Cr$, $LaNi_4V$, and $LaNi_4Zr$ are listed in Table 12. Most initial preferential hydrogen sites are 6*i*(1), 6*i*(2), or 3*f*(2), except for $LaNi_4V$ which has an initial preferential site of 6*m*(1). Where 3*f*(2) is the lowest energy site, there is no energy minimum at the 6*i*(2) site. There are no energy minima at the 12*n* sites. We have performed full optimizations on the 6*i*(1) and 6*i*(2) hydrogen sites for all $LaNi_4X$ compositions and performed an additional optimization for the 6*m*(1) site for less electronegative substitution elements such as Sc and Ti. For $LaNi_4X$ compositions, the 6*i*(1) site is the initial preferential hydrogen site when *X* = Al, Cu, Fe, Mn, Ni, Si, Sn or Zn. The 6*i*(2) site is the initial preferential hydrogen site when *X* = Co. The 3*f*(2) site is the initial preferential hydrogen site for *X* = Sc, Ti, Cr or Zr, and the 6*m*(1) site is the initial preferential hydrogen site for *X* = V.

Table 12. Hydrogen insertion site and insertion energies for selected $LaNi_4X$ host alloys

Hydrogen Site			E_{ins} (eV)				
Site	Environment	Nearest Plane	$LaNi_4Al$	$LaNi_4Co$	$LaNi_4Cr$	$LaNi_4V$	$LaNi_4Zr$
3*f*(1)	La_2Ni_4	z = 0	-0.14	-0.02	-0.09	-0.04	-0.06
3*f*(2)	$La_2Ni_2X_2$	z = 0	0.22	-0.03	**-0.25**	-0.17	**-0.38**
6*i*(1)	La_2Ni_3	z = 0	**-0.17**	-0.05	-0.15	-0.08	-0.14
6*i*(2)	La_2Ni_2X	z = 0	-	**-0.07**	-	-0.07	-
12*n*(1)	$LaNi_3$	z = 0	-	-	-	-	-
12*n*(2)	$LaNi_2X$	z = 0	-	-	-	-	-
4*h*	Ni_3X	z = 1/2	-0.06	0.02	-0.01	-	-
6*m*(1)	La_2Ni_2	z = 1/2	0.09	-0.02	-0.14	**-0.22**	-0.26
6*m*(2)	$LaNi_2X$	z = 1/2	-0.13	0.03	-0.08	-0.07	-0.19
12*o*(1)	$LaNi_3$	z = 1/2	-	-0.01	-0.04	0.02	-0.03
12*o*(2)	$LaNi_2X$	z = 1/2	-	0.01	-0.06	-0.02	-0.09

The hydrogen preferential site determination for Ti_4Mn_7X compositions were separated into two groups based on the 2*a* or 6*h* substitution site for *X*. The types of hydrogen sites and the E_{ins} for 2*a*-site substitutions such as Ti_4Mn_7Al, Ti_4Mn_7Ni, Ti_4Mn_7Ti, and Ti_4Mn_7Zn are listed in Table 13. The types of hydrogen sites and the E_{ins} for 6*h*-site substitutions such as Ti_4Mn_7Cr are listed in Table 14. Hydrogen preferential sites are $12k_1(1)$ or $6h_1$. We have performed full optimizations on the $12k_1(1)$ and $12k_1(2)$ hydrogen sites for all Ti_4Mn_7X compositions and performed an additional optimization for the $6h_1$ site for substitution elements such as V, Fe, Co and Cu. For Ti_4Mn_7X compositions, the $12k_1(1)$ site is the preferential hydrogen site when *X* = Al, Cu, Si, Sn, Ti, Zr or Zn, while the $6h_1$ site is preferential when *X* = Co, Fe, Mn, or Ni. For *X* = Cr or V, which substitute on the 6*h*-site, the hydrogen preferential site is $6h_1(1)$. While the local environment for the initial preferential hydrogen site can change in $LaNi_4X$ alloys, the Ti_4Mn_7X alloys all have a tetrahedral Ti_2Mn_2 local environment for the initial preferential hydrogen site.

Based on the hydrogen preferential sites for each of the compositions, the relative changes in the lattice parameters and unit cell volume are listed in Table 15.

Table 13. Hydrogen insertion site and insertion energies for selected Ti_4Mn_7X host alloys

Hydrogen Site			E_{ins} (eV)			
Site	Environment	Nearest Plane	Ti_4Mn_7Al	Ti_4Mn_7Ni	Ti_4Mn_7Ti	Ti_4Mn_7Zn
12k_1(1)	Ti_2Mn_2	z = 0	**-0.14**	0.04	**-0.13**	**-0.17**
12k_1(2)	Ti_2Mn_2	z = 1/2	0.25	0.23	0.18	0.25
12k_2(1)	$TiMn_2X$	z = 0	-	0.28	0.09	-
12k_2(2)	$TiMn_3$	z = 1/2	0.23	0.28	0.16	0.24
24l(1)	Ti_2Mn_2	z = 0	-	0.12	-0.09	-
24l(2)	Ti_2MnX	z = 1/2	0.16	0.12	0.10	0.15
6h_1	Ti_2Mn_2	z = 1/4, 3/4	-0.01	**0.03**	-0.01	-0.02
6h_2	Ti_2Mn_2	z = 1/4, 3/4	0.04	0.08	0.01	0.03

Table 14. Hydrogen insertion site and insertion energies for Ti_4Mn_7Cr host alloy

Hydrogen Site			E_{ins} (eV)
Site	Environment	Nearest Plane	Ti_4Mn_7Cr
12k_1(1)	Ti_2Mn_2	z = 1/4	0.15
12k_1(2)	Ti_2MnX	z = 1/4	0.12
12k_1(3)	Ti_2Mn_2	z = 3/4	0.18
12k_2(1)	$TiMn_3$	z = 1/4	0.21
12k_2(2)	$TiMn_2X$	z = 1/4	0.23
12k_2(3)	$TiMn_3$	z = 3/4	0.24
24l(1)	Ti_2Mn_2	z = 1/4	0.08
24l(2)	Ti_2MnX	z = 1/4	0.07
24l(3)	Ti_2Mn_2	z = 3/4	0.10
6h_1(1)	Ti_2Mn_2	z = 1/4	**0.02**
6h_1(2)	Ti_2MnX	z = 1/4	0.02
6h_1(3)	Ti_2Mn_2	z = 3/4	0.08
6h_2(1)	Ti_2Mn_2	z = 1/4	0.04
6h_2(2)	Ti_2MnX	z = 1/4	0.06
6h_2(3)	Ti_2Mn_2	z = 3/4	0.10

Table 15. Lattice parameter and volumetric expansions calculated for $LaNi_4XH$ and Ti_4Mn_7XH α-phase hydrides

	$LaNi_4XH$				Ti_4Mn_7XH			
X	H-site	Δ*a*/*a*	Δ*c*/*c*	Δv/v	H-site	Δ*a*/*a*	Δ*c*/*c*	Δv/v
Al	6*i*(1)	1.96%	-0.18%	3.78%	12k_1(1)	0.62%	0.33%	1.59%
Si	6*i*(1)	2.31%	-0.99%	3.63%	12k_1(1)	0.74%	0.27%	1.77%
Sc	3*f*(2)	-0.19%	2.15%	1.77%	12k_1(1)	0.49%	0.41%	1.40%
Ti	3*f*(2)	0.80%	0.97%	2.59%	12k_1(1)	0.55%	0.43%	1.53%
V	6*m*(1)	0.89%	1.08%	2.89%	6h_1(1)	0.41%	0.65%	1.47%
Cr	3*f*(2)	1.41%	0.32%	3.17%	6h_1(1)	0.45%	0.64%	1.54%
Mn	6*i*(1)	1.58%	0.46%	3.65%	6*h*	**0.48%**	**0.65%**	**1.63%**
Fe	6*i*(1)	1.67%	0.23%	3.61%	6h_1	0.50%	0.64%	1.64%
Co	6*i*(2)	1.10%	0.77%	3.01%	6h_1	0.54%	0.60%	1.69%
Ni	6*i*	**1.48%**	**0.53%**	**3.54%**	6h_1	0.63%	0.43%	1.69%
Cu	6*i*(1)	1.42%	0.79%	3.68%	12k_1(1)	0.60%	0.51%	1.73%
Zn	6*i*(1)	1.73%	0.29%	3.78%	12k_1(1)	0.61%	0.47%	1.70%
Zr	3*f*(2)	-0.31%	2.73%	2.09%	12k_1(1)	0.26%	0.79%	1.32%
Sn	6*i*(1)	1.60%	0.20%	3.43%	12k_1(1)	0.52%	0.36%	1.41%

It is difficult to directly compare the two types of unit cells due to the differences in symmetry and number of atoms. $LaNi_5$ absorbs up to 7 H per unit cell, and $TiMn_2$ absorbs up to 3 H per formula unit with 4 formula units per unit cell. The *a* parameter for $LaNi_4X$ is ~1.1 times larger than Ti_4Mn_7X, and the *c* parameter is ~0.5 times smaller. It is useful to look at both relative changes (e.g. *Δv/v*) as well as the absolute changes (e.g. Δ*v*) in the unit cell parameters to quantify lattice expansion. As we are only considering the insertion of a single H atom per unit cell, the absolute changes represent normalized displacements in the unit-cell lattice incurred by that single H atom. We systematically analyze the changes in structure and how they evolve in dilute $LaNi_4X$ and Ti_4Mn_7X hydride systems.

4.4.1 Relative Lattice Expansion vs. c/a Ratio

The absolute values of the calculated relative lattice expansion |Δ*a*/*a*|, |Δ*c*/*c*|, and |Δ*v*/*v*| for $LaNi_4XH$ and Ti_4Mn_7XH compositions are plotted against the calculated *c*/*a* ratio before

hydrogen insertion in Figure 20, respectively. General linear trends with large outliers are observed for the $LaNi_4X$ system, while general parabolic trends are observed for the Ti_4Mn_7XH system. In both systems, the trend in $|\Delta v/v|$ follows the trend in $|\Delta a/a|$ ($v = a^2c \cdot \sin\frac{\pi}{3}$), while the trend in $|\Delta c/c|$ appears to follow a trend in the opposite.

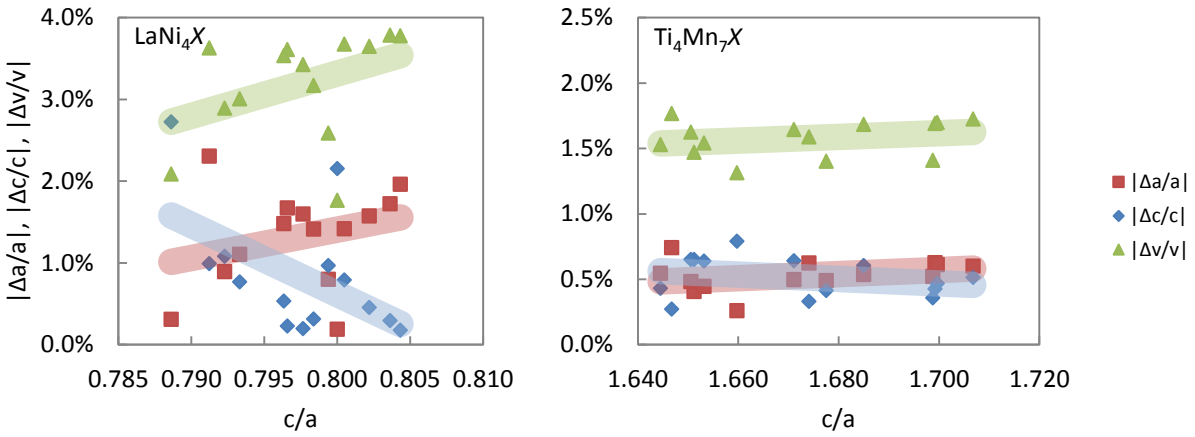

Figure 20. Calculated relative lattice expansion |Δa/a|, |Δc/c|, and |Δv/v| for $LaNi_4X$ and Ti_4Mn_7X systems

Experimental PCT hysteresis data is available for comparison to the relative lattice expansions that we have calculated. The AB_5 data set is based on $MmNi_{4.7}Al_{0.3}X_{0.1}$ compositions (by Osumi et al. [101]), and the AB_2 data set uses $ZrCr_{1.8}X_{0.2}$ compositions (by Young et al. [103]), where the X are elements from rows 2−5 of the periodic table but do not necessarily contain the same set of elements as in the calculations performed in this study. PCT hysteresis arises from irreversible energy losses in the hydrogen absorption-desorption process, and it is defined as $\ln(P_a/P_d)$, where P_a and P_d are the absorption and desorption mid-point equilibrium pressures, respectively [103]. High hysteresis has been correlated to higher degrees of pulverization, which shortens cycle life [102, 103]. Higher *c/a* ratios in AB_5-type alloys tend to exhibit lower hysteresis [101, 102], whereas AB_2-type alloys tend to prefer lower *c/a* ratios [103]. Models relating to plastic deformation, defect formation, and elasticity have been proposed by

research groups over the years to explain the source of the hysteresis [103]. If the hysteresis can be correlated to the initial lattice expansion calculated for the two alloy systems, examining the hysteresis trends shows that the AB_5 hysteresis more closely resembles the behavior for the initial $|\Delta c/c|$ lattice expansion rather than for $|\Delta a/a|$ or $|\Delta v/v|$. On the other hand, the AB_2 hysteresis weakly resembles the behavior for $|\Delta a/a|$ or $|\Delta v/v|$ lattice expansions rather than for $|\Delta c/c|$. Lattice expansion has been shown to introduce microstrain into the crystal lattice of $LaNi_5$-type alloys, particularly between the α- and β-hydride phases, with the lattice expansion along the *c*-axis in particular showing a correlation with gaseous-phase degradation behavior [130].

4.4.2 Effect of Anisotropy

Anisotropy associated with the initial lattice expansion of the two MH systems may explain the apparent directional dependence of its correlation to PCT hysteresis. Δc is plotted against Δa for $LaNi_4XH$ and Ti_4Mn_7XH compositions in Figure 21, representing the displacements of the unit-cell lattice after the insertion of a single hydrogen atom. The dotted $\Delta c=\Delta a$ line represents isotropic displacements that accommodate the hydrogen insertion. It is clear that for most $LaNi_4XH$ compositions, the unit cell expands more in the *a* direction than the *c* direction, while the opposite is true for most Ti_4Mn_7XH compositions. In general, $LaNi_4XH$ compositions also expand more in volume to accommodate a single hydrogen atom than Ti_4Mn_7XH compositions.

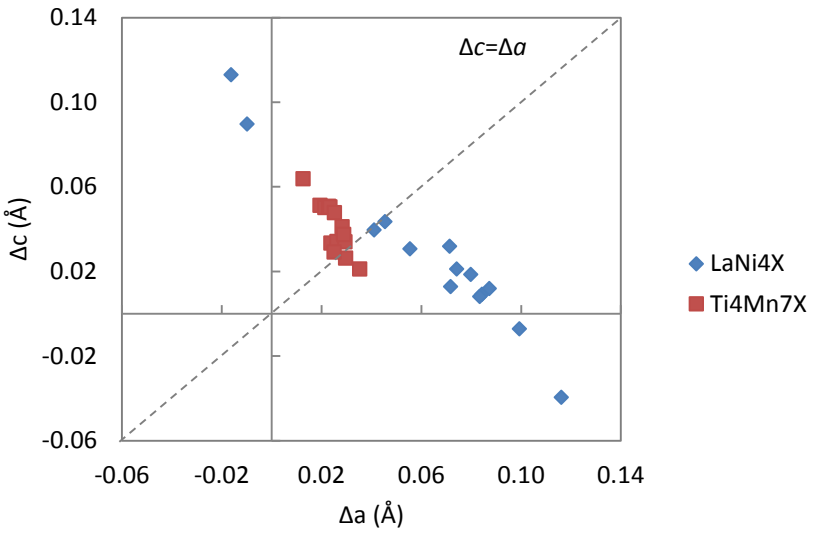

Figure 21. Anisotropy of lattice displacements for $LaNi_4X$ and Ti_4Mn_7X host alloys

Experimental and calculated elastic constants for $LaNi_5$ show $C_{33}/C_{11} \approx 1.2$, and the literature notes that this indicates that elastic deformation is easier normal to the *c*-axis than along it [106, 131, 132]. Conversely, we can interpret this to mean there is higher resistance to elastic deformation in the *c* direction. Calculated elastic constants for C14 AB_2 compositions in literature range from C_{33}/C_{11} = 0.9 to 1.2 [115, 133-135], and Δc vs. Δa data for Ti_4Mn_7XH compositions in Figure 21 cluster around the $\Delta c=\Delta a$. However, highly anisotropic materials such as layered metal oxides have very low C_{33}/C_{11} values while showing a correlation between capacity fade and $\Delta c/c$ strain [136]. Lithium cobalt oxide has C_{33}/C_{11} values ranging from 0.05 to 0.57 depending on the lithium content [137] despite the higher resistance to deform in the *a* direction. It appears that the anisotropy indicated by the ratio of elastic constants (ie. resistance to deformation) and the correlation to the anisotropy of the lattice expansion depends on the nature of the structure of the material. For non-layered materials such as AB_5 and AB_2 intermetallics, the lattice expansion in the direction where there is higher resistance to deformation appears to correlate to indicators of degradation, both calculated and measured.

To account for the anisotropy between the $LaNi_4XH$ and Ti_4Mn_7XH systems, we have defined $|\Delta c/\Delta a|$ as a measure of anisotropy, where a value of 1 indicates equal deformation in *a* and *c*, a value >1 indicates easier deformation in *c* than *a*, and a value <1 indicates easier deformation in *a* than *c*. The limiting lattice expansion $|\Delta d/d|$ is then defined to be equal to $|\Delta c/c|$ where $|\Delta c/\Delta a| < 1$ and equal to $|\Delta a/a|$ where $|\Delta c/\Delta a| \geq 1$. The experimental hysteresis and the calculated $|\Delta d/d|$ are plotted against normalized *c/a* ratios for the AB_5 and AB_2 systems in Figure 22. There is better correlation (and fewer outliers) between hysteresis and the limiting lattice expansion for both systems.

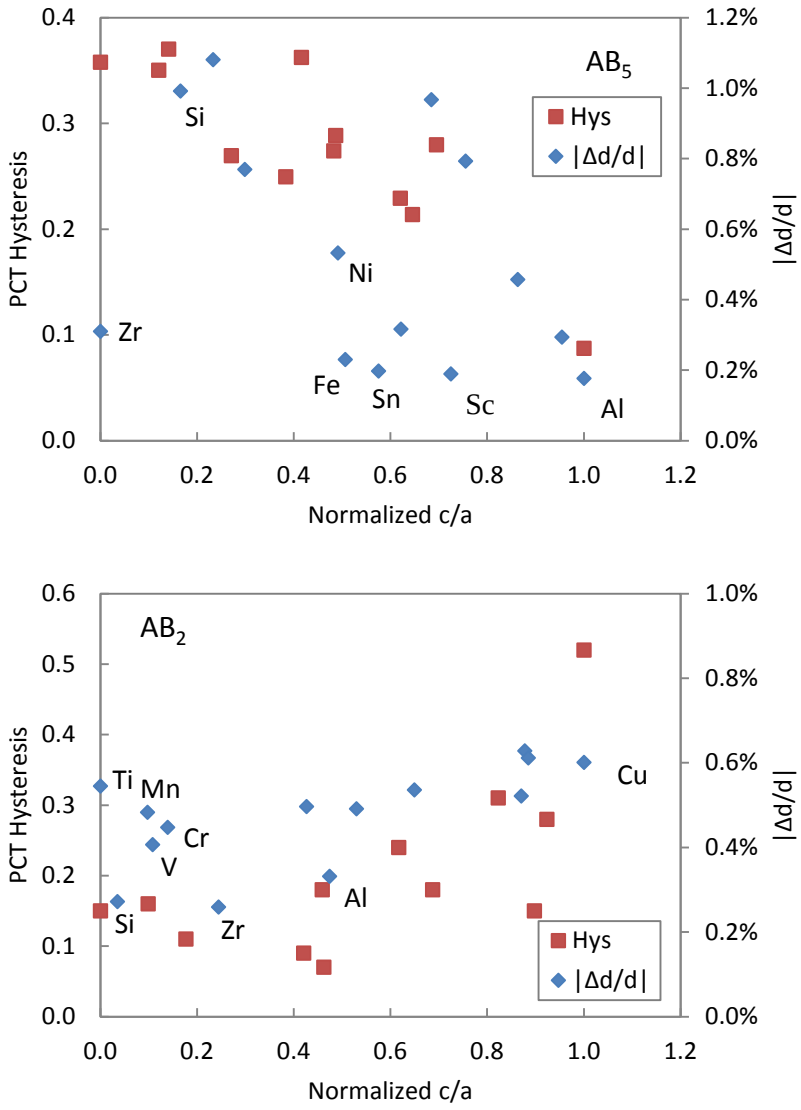

Figure 22. PCT Hysteresis and calculated lattice expansion as functions of normalized c/a ratios for AB_5 and AB_2 systems

The substitution elements that are calculated to have the lowest $|\Delta d/d|$ for $LaNi_4XH$ are Al, Sc, and Sn. Additives that are documented to improve the cycle stability and/or the hydrogen storage capacity degradation of AB_5-type alloys include Al, Si, and Sn [83, 87, 90-97]. Zr appears as a strong outlier, likely due to the solubility of Zr for La in $LaNi_5$ phase (similarly for Sc). Zr in combination with Al, however, has been reported to help pulverization resistance and reduce PCT hysteresis [101]. Si and Al are the few modifiers that show a directional lattice

compression (negative $\Delta d/d$, particularly in the c direction). The literature only provides studies up to $LaNi_{4.5}Si_{0.5}$ due to the solubility of Si, which is a possible explanation for the discrepancy, and they report that only small amounts of Si are needed for improved performance degradation. The Al, Si, and Sn additives are noted to have greatly reduced the concentration of defects induced in LaNi5-based alloys after hydrogenation, and the PCT isotherms for the first hydrogenation also reflect a dramatic decrease in the hysteresis [92, 98, 138]. While these materials show excellent cycling characteristics in the gaseous phase, they also appear to pulverize more severely [88, 92, 97, 138]. The research groups have proposed theories related to increased hardness in the material and higher defect formation energies associated with additives account for the increased pulverization. Indeed, the dislocation density has been correlated more strongly to the PCT hysteresis for a wider range of compositions [92].

The substitution elements that are calculated to have the lowest $|\Delta d/d|$ for Ti_4Mn_7X are Al, Si and Zr, while the $ZrCr_{1.8}X_{0.2}$ data shows the lowest hysteresis for V, Cu and Cr. Experimental data for $TiMn_2$-based alloys also show V and Cr promoting lower hysteresis [139], as well as Al [140]. We should note that $ZrMn_2$ exists in the C14 phase, and so the Zr addition calculated may not be reflected experimentally. The calculated $|\Delta d/d|$ is lower for Cr and V compared to the $TiMn_2$ composition, which is consistent with the experimental hysteresis. However, it is also interesting to note that Cr and V prefer to substitute on the 6*h* site, whereas the other additives prefer to substitute on the 2*a* site. Also we note that in Table 4, energy is required to insert hydrogen in each of the sites investigated, and so further study incorporating magnetic effects or examining the difference between the two substitution sites may be of interest.

4.4.3 Effect of Hydrogen Insertion Site

The lowest energy hydrogen insertion site depends on the substitution element in the $LaNi_4XH$ and Ti_4Mn_7XH systems, but we also examine the effect of a single insertion site on the correlation between the limiting lattice expansion $|\Delta d/d|$ and c/a ratio. We have chosen the $6i(1)$ site for the $LaNi_4XH$ system and the $12k_1(1)$ site for the Ti_4Mn_7XH system to study, and the calculated $|\Delta d/d|$ are plotted against normalized c/a ratios for the two systems in Figure 23, respectively. A better degree of correlation appears to emerge for both systems. $LaNi_4XH$ with $6i(1)$ site all have $|\Delta c/\Delta a|$ ratios <1, indicating that the lattice expansion in c direction correlates to hysteresis for all compositions. Ti_4Mn_7XH with the $12k_1(1)$ site converts some of the $|\Delta c/\Delta a|$ ratios that are >1 to values that are <1 (for X = V, Cr, Mn, Fe, Co). When the lowest energy hydrogen insertion site is considered, differences that arise from the interactions with the additive can become more prominent. This effect is noticeably apparent when examining experimental hysteresis trends between compositions with varying degrees of substitution (in terms of the number of elements and the amount of substitution), and a trend is harder to discern compared to more controlled experiments [92].

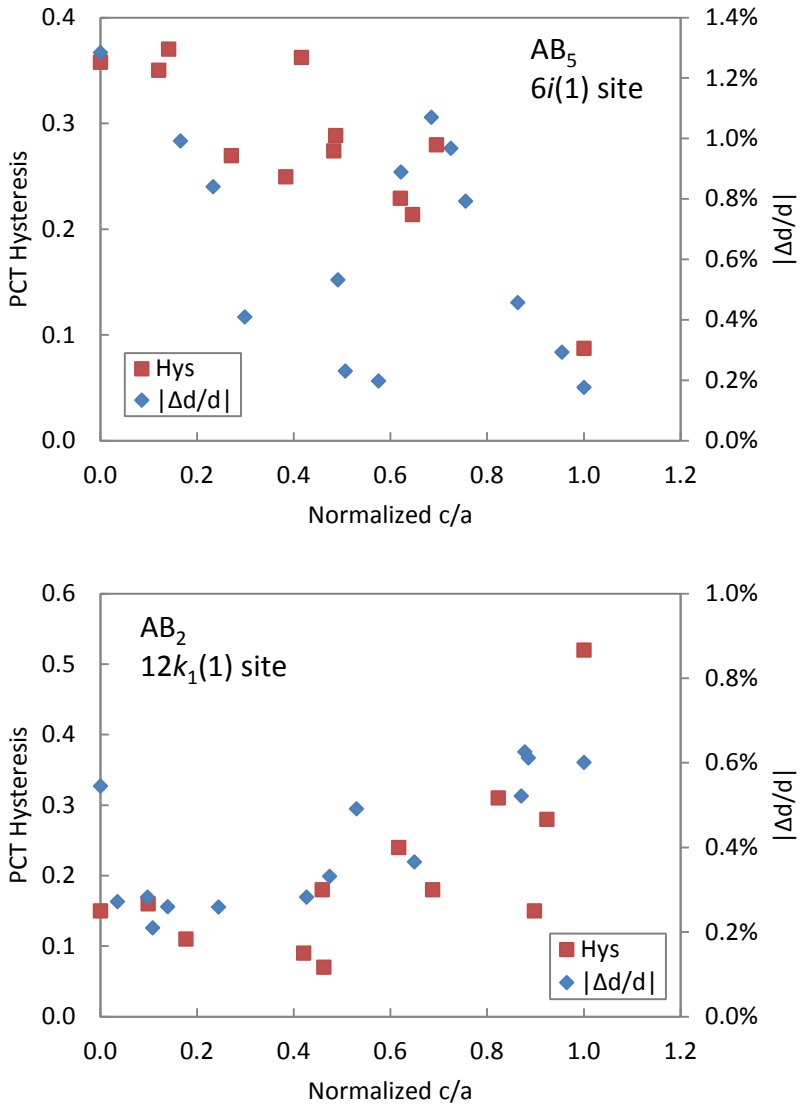

Figure 23. PCT hysteresis and calculated lattice expansion as functions of normalized c/a ratios for AB_5 in the 6i(1) site and AB_2 in the $12k_1$(1) site

4.4.4 Average Electron Concentration

A parabolic trend between the PCT hysteresis and a modified average electron concentration *e/a* has been shown in AB_2-based alloys, which follows the correlations observed between the *c/a* ratio for hexagonal close-packed crystals and the number of *d*-band electrons for transition metals [105]. We also calculate the *e/a* using the equivalent number of outer shell electrons method and plot the limiting lattice expansion $|\Delta d/d|$ with respect to the normalized *e/a*

value in Figure 24, which is also compared against the experimental $ZrCr_{1.8}X_{0.2}$ hysteresis data. A parabolic trend can be seen from the calculated data, but a second band of data can also be seen. The upper band consists of elements at the beginning and end of the first row *d*-band transition metals, while the lower band consists the middle first row *d*-band transition metals as well as Zr, Al, Si, and Sn. Zr, Al, Si and Sn have larger atomic radii compared to the other elements for compositions with similar *e/a* values (calculated on a per atom basis), and a spatial density may also have an influence on the hysteresis trends that we have discussed.

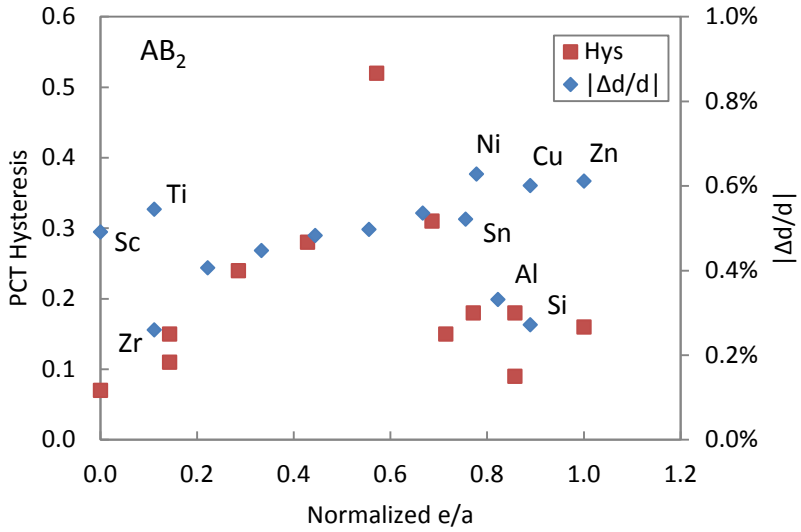

Figure 24. PCT hysteresis and calculated lattice expansion as functions of normalized e/a

4.4.5 Initial Factors vs. Dynamic Factors

Degradation, whether respect to hydrogen storage capacity, discharge capacity or particle size, is a dynamic process that involves numerous factors that may also interact. While the calculations reported here more closely simulates the initial hydrogenation behavior of the first hydrogen absorption cycle, it is interesting that these calculations for the initial structures appear to correlate to hysteresis, which involves processes that propagate under numerous full hydriding-dehydriding cycles. Initial hydrogenation studies using TEM techniques show

significant development of defects even at hydrogen concentrations as low as [H]/[$LaNi_5$] = 0.17 [141]. The development of defects grows as the hydride transforms from α-phase to β-phase, but little change is detected with further hydriding-dehydriding cycles. In-situ x-ray diffraction studies show the development of the broadening of certain diffraction peaks and the strain induced in the crystal lattice of the β-phase rather than the α-phase hydride upon hydrogen absorption in $LaNi_5$ whereas in $LaNi_{4.75}Al_{0.25}$ the two hydride phase domains are suggested to exert a reversible anisotropic strain upon desorption [142, 143]. Often it is the discrete lattice expansion between the α-phase and the β-phase that are correlated to degradation indicators [130, 144]. Further calculations involving the β-phase hydrides could offer insight to the degradation processes.

4.5 Summary

The structures of substituted $LaNi_4X$ and C14 Ti_4Mn_7X compositions and their near α-phase hydrides were calculated by first principles. $LaNi_4X$ host alloys are calculated to expand more in the *a* direction than the *c* direction, while Ti_4Mn_7X host alloys are calculated to expand more in the *c* direction. The lattice and volumetric expansions in the near α-phase hydrides are analyzed with respect to the host alloy *c/a* ratios and *e/a* values, and there is a general trend in lattice expansion in the direction with higher resistance to elastic deformation that reflects the trends observed with hysteresis measured in AB_5 and C14 AB_2 type alloys. Experimental data in the gaseous phase and calculations from literature note that lattice expansion induces microstrains into the crystal lattice and that lattice expansion in the *c* direction for $LaNi_5$-based alloys more strongly correlates to degradation, while observing significantly lower degrees of hysteresis and dislocation density. The *c* direction for $LaNi_5$-based alloys tends to have higher resistance to elastic deformation, and depending on the defect formation energies for the

compound, may form defects upon hydrogenation, which can be linked to as irreversible energy losses that manifest as hysteresis in PCT isotherms in metal hydride materials. The hydrogenation site for the two systems also have an effect, indicting the interactions with the additives start to play a larger role as more substitutions are made. Lattice expansion in the direction with higher resistance to elastic deformation for C14 AB_2 type alloys additionally shows a similar trend to experimental hysteresis with respect to the average electron concentration with some variation depending on the spatial electron density. Given these observations, the computational method used in this study can help to predict the hysteresis trends associated with the structure of AB_5 and C14 AB_2 MH alloys. The complex, multi-phase nature of the many MH alloys used in NiMH batteries holds multiple pathways possible for performance deterioration – such as corrosion and oxidation effects – which are all inextricably linked, but computational methods can allow insights into these alloys with regards to minimizing lattice expansion.

CHAPTER 5. STACKING FAULTS IN NICKEL HYDROXIDE SPHERICAL POWDERS

Nickel hydroxide spherical powders are characterized by high tap densities (> 1.8 g/cc) and small crystallite sizes (full width half maximum (FWHM) > 0.8° for the (101) diffraction peak) [49]. Perfect crystals of the layered nickel hydroxide materials have poor electrochemical activity, but defects and stacking faults within the crystal structure facilitate the transport of electrons and protons required for the electrochemical reduction-oxidation reactions to occur. The (101) and (102) peak broadenings observed in the nickel hydroxide powder x-ray diffraction (PXRD) patterns are theorized to be related to the degree of stacking faults within the crystal structure [29, 33] and the broadening of those specific peaks are noted to correlate to electrochemical performance [31].

Substituted nickel hydroxide spherical powders have small crystallite sizes and stacking faults that are necessary for electrochemical activity. SEM images depicting the spherical particle morphology and the hexagonal platelets that make up the particles are shown in Figure 25. Additives, precipitation conditions and precipitation time can greatly affect the morphology and defect structures of the powders, and the differences in the diffraction lines can be discerned in the PXRD patterns. Better understanding of how stacking faults evolve with respect to the preparation conditions can help researchers to optimize the structures that promotes high electrochemical activity. We have tracked substituted nickel hydroxide spherical powder samples under precipitation to study how the different types of stacking faults may change with precipitation time and composition via Rietveld refinement and DIFFaX simulation.

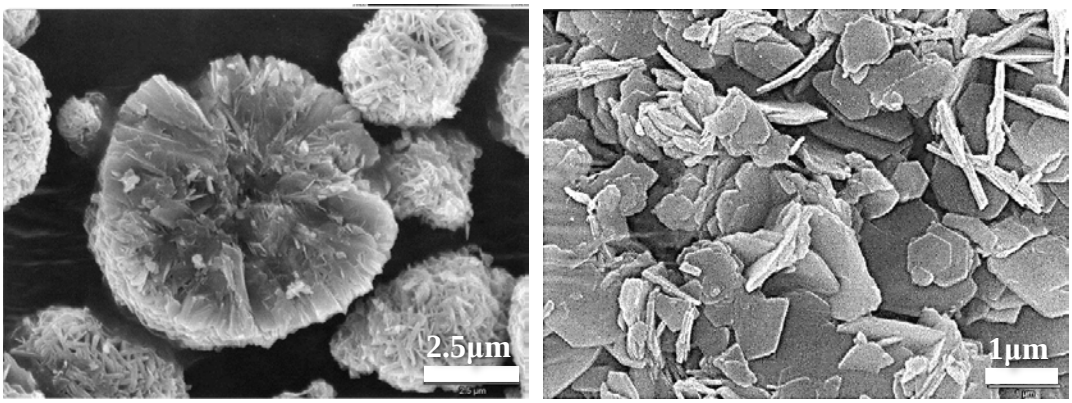

Figure 25. SEM images of nickel hydroxide spherical powders

5.1 Background

A method for simulating PXRD patterns for crystal structures that contain stacking faults has been developed by Treacy et al. and is implemented in a program called DIFFaX [34]. Several research groups have leveraged the DIFFaX program to study the stacking fault structure of nickel hydroxides and its effect on electrochemical properties. Delmas and Tessier were the first to correlate changes in the (101) and (102) peak widths through pattern matching of faulted structures generated by DIFFaX to two types of stacking faults: growth faults and deformation faults [29, 33]. Ramesh and Kamath systematically analyzed the type of stacking faults to their effects on PXRD patterns [39-41] and they have also looked at the effects of crystallinity and disorder on electrochemical performance [42, 45]. Casas-Cabanas et al. compared anisotropic size effects to the stacking fault models and found that anisotropic crystallite sizes can also affect the peak broadening of the (101) and (102) peaks, but shifts in the peaks were solely correlated to stacking faults [35-38]. Stacking faults were found to be significant for smaller crystallite sizes (less than 350 Å diameter, 100 Å height), and the materials with the peak shift signatures showed higher electrochemical capacity. An illustration depicting how stacking faults preserve

periodicity for (001) and (100) planes and disrupt periodicity for (101) planes leading to the selective broadening of (*h*0*l*) type planes is shown in Figure 26.

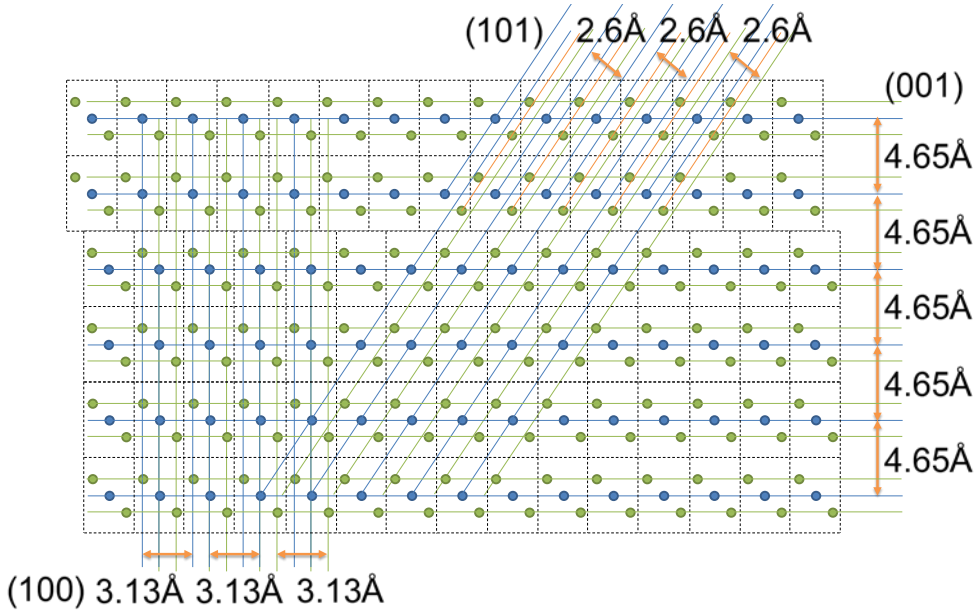

Figure 26. Illustration showing stacking faults preserving periodicity for (001) and (100) planes and disrupting periodicity for (101) planes.

5.2 Experimental Setup

Substituted nickel hydroxide spherical powders were synthesized through the continuous precipitation of metal sulfates (Ni, Co, and/or Zn) with sodium hydroxide and ammonium hydroxide under strong stirring while maintaining constant temperature, flow rate, and pH. Product is collected as the overflow effluent from the top of the reactor. The precipitation process requires an initial "start-up" period, in which the particles in the precipitation process stabilize, and thereafter the product is considered to be "in spec". Samples were taken at different intervals during the initial precipitation process. Due to the scale of the reactor, the samples were taken from the accumulation of a single collection container, which was mixed to ensure uniformity before sampling. The powder samples were washed and then dried overnight

in an oven. A Rigaku Miniflex x-ray diffractometer was used to obtain PXRD patterns for pattern matching to DIFFaX simulation patterns.

5.3 Structure Refinement

β-$Ni(OH)_2$ has a hexagonal crystal structure belonging to space group $P\bar{3}m1$ with lattice parameters a = 3.13 Å and c = 4.65 Å [30]. Ni, O, and H occupy the 1a, 2d_1, and 2d_2 sites, respectively, forming slabs composed of H, O, Ni, O, H layers. Structural disorder in the stacking of the slabs results in interstatification and stacking faults within the material, and the stacking faults fall under two major categories termed "deformation faults" and "growth faults" by Delmas and Tessier [29]. A detailed discussion of the different $Ni(OH)_2$ polytypes and their stacking is discussed by Ramesh et al. [40] A first-principles study modeling the different stacking types found that deformation faults had the lowest energy of the stacking faults, indicating a higher probability for the stacking fault to occur [43]. Growth faults had the next lowest energy for a smaller probability of prevalence.

Structural disorder in $Ni(OH)_2$ crystal structure is constructed out repeating slabs stacked according to a defined stacking vector (x, y, z). Ideal stacking along the c-axis has a stacking vector of (0, 0, 1). The deformation fault has a stacking vector of (1/3, 2/3, 1). The growth fault uses a slab with mirror symmetry to the original slab and has a stacking vector of (1/3, 2/3, 1). Interstratification occurs when water is trapped between slabs, and a stacking vector of (x, y, 1.65) yields an interplanar spacing of 7.6 Å to accommodate the water molecules [39]. The x and y are assigned random values in the simulation.

The Rietveld refinement technique was used to match the PXRD patterns generated by the DIFFaX program to the patterns obtained from the samples. We calculated R^2 and R_{wp} factors to judge the quality of the refinement, and used the Nelder-Mead simplex algorithm to minimize

1-R^2 and R_{wp} values. Refinement parameters such as the pseudo-Voigt instrument parameters *u*, *v*, *w*, σ, the lattice parameters *a*, *c*, the atomic positions, the stacking fault composition (ideal stacking, deformation faults, growth faults, and interstratification), the *z*-spacing for each type of fault, and the Debye temperature factors were adjustable in the original DIFFaX program, but we also implemented additional refinement parameters to account for the zero shift, scaling factor, $K_{\alpha 1 \alpha 2}$ and background. We neglect the anisotropic crystallite size effects because at the small crystallite sizes, the peak shift signatures associated with stacking faults can be discerned and modeled. Due to the large number of refinement parameters, we designated a set of parameters to refine at a time, and iterated through the different sets multiple times until $R^2 > 98\%$ and $R_{wp} < 5\%$. For example, we first removed the diffraction peaks to fit the background parameters for the refinement, then fixed the background parameters to refine the lattice structure parameters, and so on. We were able to improve some poor refinements by using the refinement parameters from neighboring samples as initial input parameters.

5.4 Results and Discussion

Eight compositions of the general formula $Ni_{1-x-y}Co_xZn_y(OH)_2$ were prepared, where *x* and *y* = 0, 0.03, 0.06, or 0.09 and $x + y \leq 0.09$. Each composition run was sampled nine times (*t* = 1, 2, 3, 4, 6, 8, 24, 28, 32 hours) during the precipitation process for a total of 72 different samples. A list of the samples and some of their refined parameters are provided in Table 16. Crystallite sizes (XS) are estimated from the Scherrer equation based on the FWHM of selected peaks. The patterns for the $Ni(OH)_2$ composition sampled at each of the sampling times and the PXRD patterns for each composition sampled after 8 hours are shown in Figure 27 and Figure 28. The pattern refinements of $Ni(OH)_2$ after 32 hours of precipitation and of $Ni_{0.94}Co_{0.03}Zn_{0.03}(OH)_2$ after 8 hours of precipitation are shown in Figure 29 and Figure 30, to illustrate the goodness-of-

fit. The $Ni(OH)_2$ refinement is an example showing the typical fit of the refinement, while the $Ni_{0.94}Co_{0.03}Zn_{0.03}(OH)_2$ refinement is an example showing poorer fit. The $Ni_{0.94}Co_{0.03}Zn_{0.03}(OH)_2$ compositions show the most scatter in the refinement parameters due to the presence of a second peak near the (001) reflection. This second peak appears to be a second phase with a different *c* lattice parameter because the intensity of the peaks shift with precipitation time. However, segregation in terms of composition was not detected in electron dispersive spectroscopy (EDS) analysis. With the exception of some $Ni_{0.94}Co_{0.03}Zn_{0.03}(OH)_2$ samples, refinement parameters appeared consistent, falling within reasonable values, with small variation, due to the aggregation of the powder samples over time.

Table 16. Summary of select refinements parameters for substituted nickel hydroxide spherical powders

Composition	Time (h)	*a* (Å)	*c* (Å)	Ideal Stacking	Deform. Faults	Growth Faults	Interstrat.	$XS_{(100)}$ (Å)	$XS_{(001)}$ (Å)	$XS_{(101)}$ (Å)
$Ni(OH)_2$	1	3.122	4.645	0.781	0.140	0.044	0.035	218.3	112.0	89.6
	2	3.122	4.644	0.784	0.141	0.040	0.035	218.3	112.0	91.5
	3	3.122	4.648	0.792	0.130	0.043	0.035	218.3	108.9	91.5
	4	3.122	4.650	0.781	0.139	0.044	0.036	218.3	112.0	89.6
	6	3.122	4.649	0.783	0.140	0.040	0.037	218.3	109.0	87.7
	8	3.122	4.650	0.790	0.128	0.047	0.035	218.3	108.9	85.9
	24	3.122	4.655	0.784	0.132	0.053	0.030	207.4	106.1	81.0
	28	3.123	4.655	0.789	0.126	0.057	0.027	207.4	103.4	78.0
	32	3.122	4.654	0.779	0.138	0.058	0.026	207.4	103.4	76.6
$Ni_{0.97}Co_{0.03}(OH)_2$	1	3.124	4.651	0.902	0.049	0.002	0.047	244.0	118.6	145.2
	2	3.124	4.649	0.907	0.045	0.000	0.048	259.2	115.2	150.4
	3	3.126	4.652	0.906	0.048	0.000	0.046	244.0	118.6	145.2
	4	3.124	4.649	0.906	0.047	0.000	0.047	244.0	115.2	145.2
	6	3.124	4.650	0.906	0.046	0.000	0.048	259.2	115.2	145.2
	8	3.124	4.651	0.904	0.046	0.000	0.049	244.0	115.2	145.2
	24	3.122	4.656	0.892	0.054	0.001	0.053	244.0	109.0	140.4
	28	3.123	4.656	0.892	0.052	0.004	0.052	244.0	109.0	140.4
	32	3.124	4.658	0.893	0.053	0.003	0.051	244.0	112.0	145.2
$Ni_{0.94}Co_{0.06}(OH)_2$	1	3.122	4.657	0.880	0.059	0.003	0.058	244.0	100.8	135.8
	2	3.122	4.657	0.883	0.059	0.000	0.058	243.9	100.8	135.8
	3	3.122	4.658	0.883	0.058	0.001	0.057	244.0	103.4	135.9
	4	3.122	4.657	0.885	0.057	0.001	0.057	243.9	103.4	135.8
	6	3.122	4.657	0.884	0.057	0.002	0.057	244.0	103.4	135.8
	8	3.122	4.657	0.883	0.058	0.002	0.057	243.9	106.1	140.4
	24	3.122	4.657	0.884	0.058	0.001	0.057	244.0	103.4	135.8
	28	3.122	4.658	0.883	0.057	0.001	0.059	244.0	106.1	145.2
	32	3.122	4.657	0.883	0.056	0.002	0.059	244.0	106.1	145.2

Composition	Time (h)	*a* (Å)	*c* (Å)	Ideal Stacking	Deform. Faults	Growth Faults	Interstrat.	$XS_{(100)}$ (Å)	$XS_{(001)}$ (Å)	$XS_{(101)}$ (Å)
$Ni_{0.91}Co_{0.09}(OH)_2$	1	3.126	4.647	0.888	0.056	0.002	0.053	243.9	139.0	145.2
	2	3.126	4.645	0.886	0.060	0.002	0.052	243.9	139.0	145.2
	3	3.126	4.650	0.880	0.058	0.003	0.058	230.4	134.4	145.2
	4	3.126	4.648	0.887	0.057	0.002	0.055	230.4	139.0	145.2
	6	3.126	4.651	0.867	0.064	0.005	0.064	243.9	134.4	140.4
	8	3.126	4.648	0.892	0.053	0.005	0.050	243.9	139.0	145.2
	24	3.126	4.638	0.849	0.092	0.020	0.040	218.3	98.3	105.3
	28	3.126	4.639	0.850	0.086	0.021	0.044	244.0	93.8	108.0
	32	3.126	4.636	0.859	0.079	0.022	0.040	230.4	93.8	117.0
$Ni_{0.97}Zn_{0.03}(OH)_2$	1	3.128	4.648	0.857	0.069	0.021	0.053	243.9	118.6	117.0
	2	3.128	4.648	0.855	0.073	0.011	0.061	243.9	115.2	120.3
	3	3.128	4.647	0.856	0.072	0.014	0.058	243.9	118.6	127.6
	4	3.129	4.646	0.859	0.066	0.018	0.056	230.4	122.2	123.9
	6	3.129	4.646	0.869	0.063	0.013	0.055	243.9	126.0	127.6
	8	3.130	4.646	0.875	0.059	0.008	0.058	243.9	126.0	131.6
	24	3.130	4.644	0.897	0.051	0.002	0.051	259.2	144.0	145.2
	28	3.130	4.644	0.896	0.052	0.001	0.051	244.0	139.0	145.3
	32	3.129	4.644	0.893	0.052	0.001	0.053	244.0	144.0	150.4
$Ni_{0.94}Zn_{0.06}(OH)_2$	1	3.124	4.648	0.857	0.077	0.005	0.061	230.4	118.6	131.6
	2	3.124	4.646	0.855	0.080	0.007	0.058	244.0	122.2	127.6
	3	3.124	4.644	0.868	0.073	0.005	0.053	244.0	122.2	131.6
	4	3.122	4.645	0.861	0.075	0.008	0.056	244.0	122.2	131.6
	6	3.124	4.639	0.867	0.083	0.015	0.035	244.0	126.0	127.6
	8	3.124	4.636	0.872	0.085	0.014	0.029	244.0	130.1	135.8
	24	3.124	4.639	0.897	0.057	0.004	0.042	244.0	134.4	140.4
	28	3.124	4.638	0.899	0.056	0.003	0.041	244.0	134.4	140.4
	32	3.124	4.636	0.900	0.060	0.003	0.037	243.9	134.4	145.2

Composition	Time (h)	*a* (Å)	*c* (Å)	Ideal Stacking	Deform. Faults	Growth Faults	Interstrat.	$XS_{(100)}$ (Å)	$XS_{(001)}$ (Å)	$XS_{(101)}$ (Å)
$Ni_{0.91}Zn_{0.09}(OH)_2$	1	3.132	4.654	0.911	0.029	0.000	0.060	276.4	144.0	183.1
	2	3.130	4.655	0.898	0.031	0.002	0.069	259.2	144.0	175.5
	3	3.132	4.655	0.906	0.030	0.000	0.064	259.2	139.0	183.1
	4	3.132	4.657	0.899	0.032	0.001	0.067	276.5	134.4	175.5
	6	3.134	4.660	0.902	0.027	0.001	0.070	259.4	139.1	175.6
	8	3.134	4.656	0.911	0.028	0.000	0.061	276.6	144.0	183.2
	24	3.133	4.653	0.913	0.024	0.001	0.063	276.5	155.1	200.5
	28	3.132	4.654	0.909	0.025	0.000	0.066	276.4	155.1	200.5
	32	3.132	4.653	0.912	0.025	0.000	0.063	276.4	155.1	191.4
$Ni_{0.94}Co_{0.03}Zn_{0.03}(OH)_2$	1	3.126	4.674	0.848	0.075	0.005	0.072	243.9	87.6	123.8
	2	3.126	4.676	0.845	0.078	0.004	0.073	244.0	80.6	123.9
	3	3.126	4.674	0.850	0.074	0.005	0.071	259.2	85.8	123.8
	4	3.126	4.672	0.851	0.075	0.006	0.068	259.2	85.8	123.9
	6	3.126	4.663	0.858	0.076	0.025	0.041	243.9	73.3	117.0
	8	3.126	4.677	0.845	0.079	0.006	0.071	244.0	84.0	120.3
	24	3.124	4.673	0.853	0.077	0.020	0.049	244.0	87.6	117.0
	28	3.124	4.668	0.846	0.086	0.028	0.040	244.0	68.3	105.3
	32	3.129	4.644	0.893	0.052	0.001	0.053	244.0	144.0	150.4

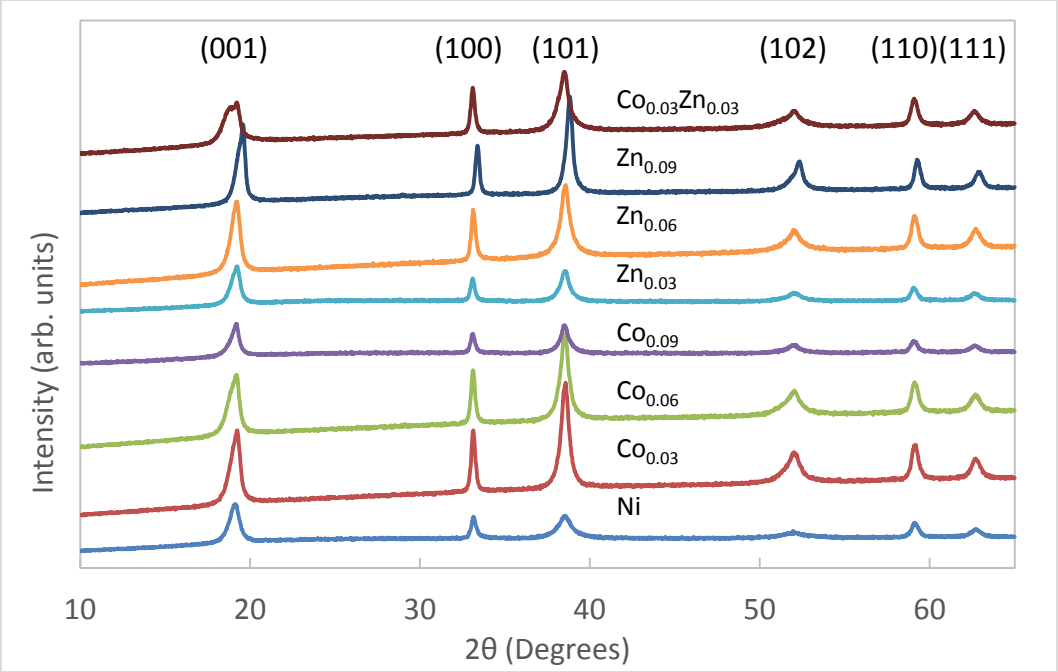

Figure 27. PXRD patterns of the substituted nickel hydroxide spherical powders after 8 h of precipitation time

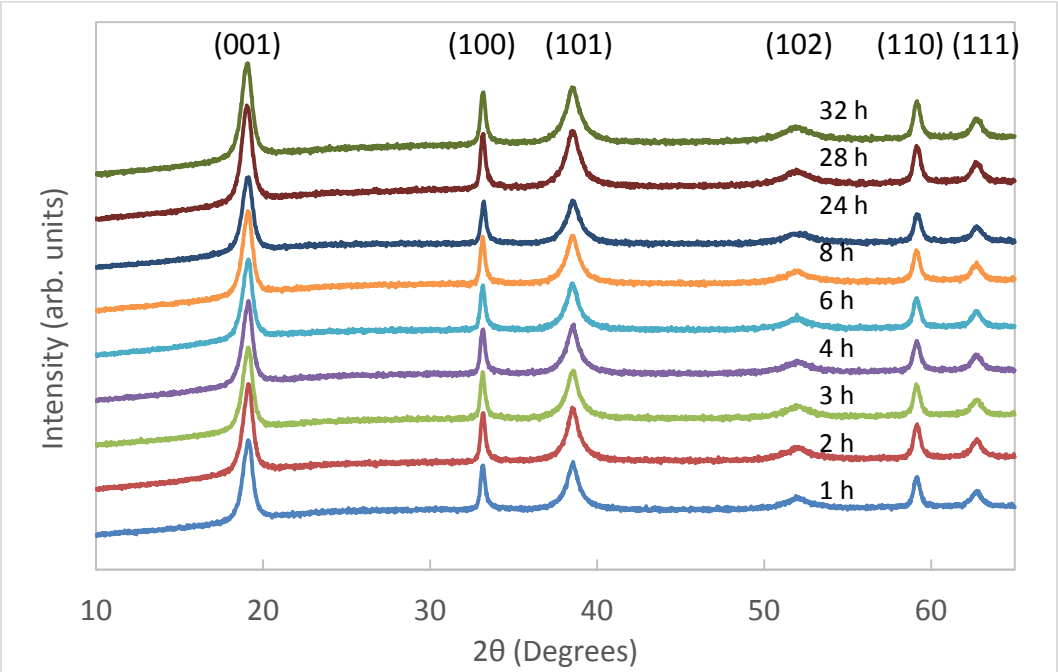

Figure 28. PXRD patterns of the $Ni(OH)_2$ composition for different sampling times up to 32 h of precipitation

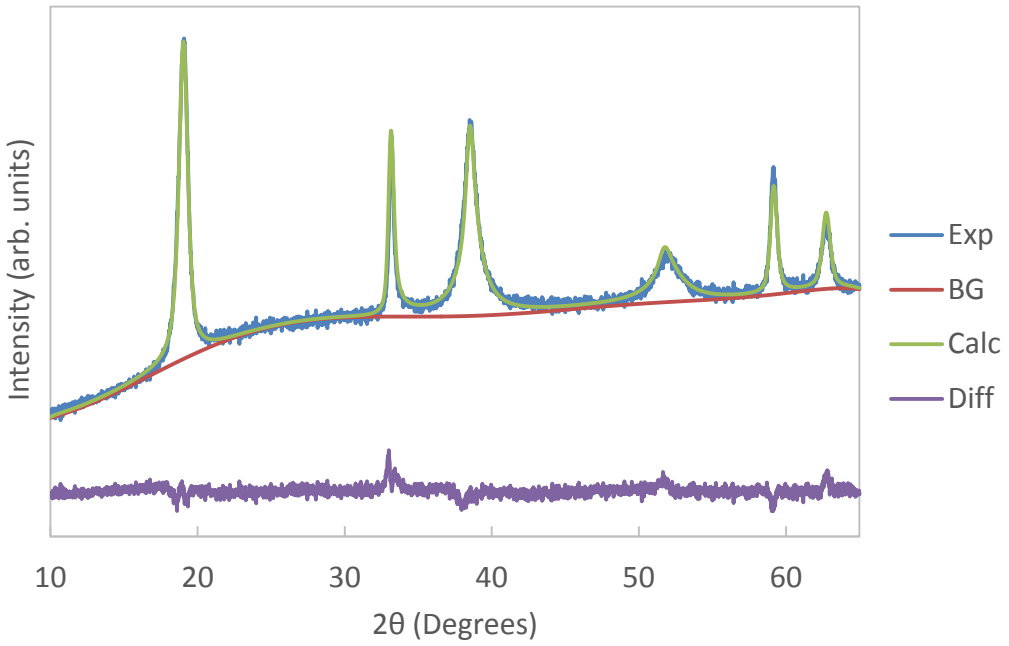

Figure 29. Experimental PXRD pattern, fitted background, calculated pattern, and refinement difference for $Ni(OH)_2$ after 32 h of precipitation

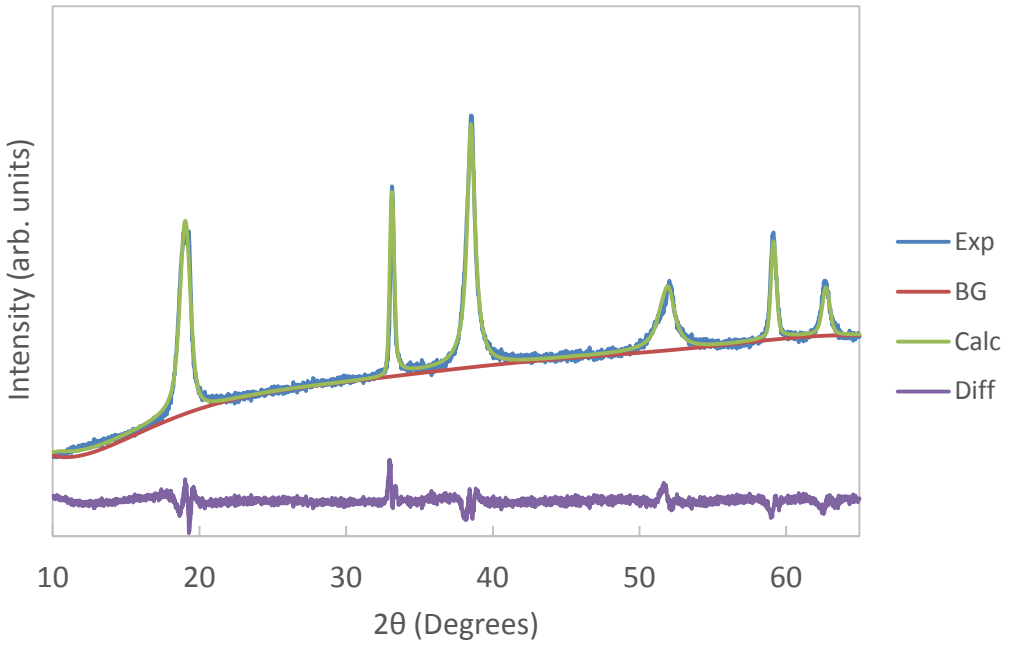

Figure 30. Experimental PXRD pattern, fitted background, calculated pattern, and refinement difference for $Ni_{0.94}Co_{0.03}Zn_{0.03}(OH)_2$ after 8 h of precipitation

5.4.1 Effect of Structural Disorder on the (101) Crystallite Size

The crystallite size estimated from the Scherrer equation based on the FWHM of the (101) diffraction peak is correlated strongly to the utilization of the theoretical electrochemical capacity of β-$Ni(OH)_2$ (289 mAh g^{-1}) [31]. The utilization increases as the (101) crystallite size decreases, and it plateaus when the crystallite size falls below ~100 Å. We use the (101) crystallite size as a metric to gauge the electrochemical utilization of the $Ni(OH)_2$ samples in lieu of electrochemical experiments. We plot the (101) crystallite size against the percentage of total structural disorder, as well as against the individual types of faults/disorder (deformation, growth, and interstratification) in Figure 31 to visualize the contributions of the stacking faults against a metric for electrochemical utilization. The smallest crystallite sizes, which is correlated to higher utilization, occurs when total structural disorder is largest, particularly of deformation and growth faults but not of interstratification. The trends for deformation faults and growth faults largely follow the trend for total structural disorder, but deformation faults make up a larger proportion of the total disorder (maximum of ~14% deformation faults, ~6% growth faults, ~7% interstratification). The largest crystallite sizes occur when structural disorder is low but interstratification makes up the largest proportion of the disorder. Interstratification shows a large degree of scatter with respect to the (101) crystallite size.

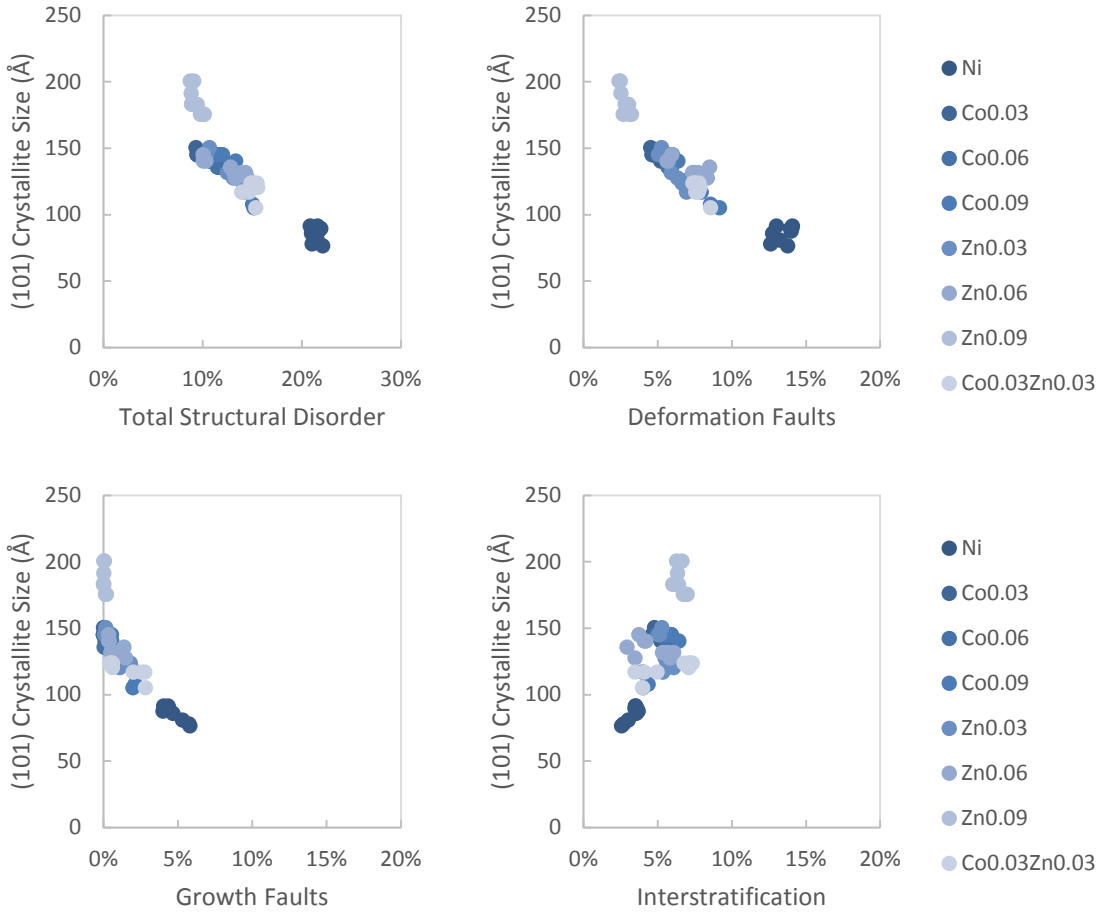

Figure 31. Effects of total disorder and individual faulting/disorder on (101) crystallite size

5.4.2 Deformation Faults vs. Growth Faults

First principle calculations indicate that pure nickel hydroxide is expected to form deformation faults at a higher probability to growth faults [43]. Our refinements are consistent with this finding. Figure 32 shows a plot of the percentage of growth faults with respect to the percentage of deformation faults, which illustrates this correlation, but there is also a wide band allowing a degree of variability that depends on precipitation time. To see the relative contributions of growth faults and deformation faults, we plot the (101) crystallite size metric with respect to the ratio of growth faults to deformation faults in Figure 33. For (101) crystallite sizes below 150 Å, there is a clear linear trend showing a higher proportion of growth faults

correlating to smaller crystallite sizes, which indicates a higher likelihood for higher electrochemical utilization. Ramesh et al. have also observed higher electrochemical utilization for samples that are modeled to have higher degrees of growth faults (called $2H_2$ faults in the paper) [145]. They point out that the structural differences in the $[HO_4]$ tetrahedra provide instability to both types of faulted structures, which in turn facilitate the proton transfer needed for electrochemical activity. However, because there is a relationship between growth faults and deformation faults in terms of relative defect formation energies, we need to control for the total percentage of stacking faults to extricate the effect of growth faults from the total increase in stacking faults. Controlling for the total percentage of stacking faults shows that deformation faults have a stronger negative correlation to the (101) crystallite size when growth faults are low. When growth faults are high, the growth faults have a stronger negative correlation than the deformation faults. This further supports that growth faults are a strong indicator for electrochemical utilization. Additional first-principles calculations that investigate how additives affect the stacking fault formation energies can be of interest, but it appears that the common Co and Zn additives do not lower the formation energies of growth faults below the energies for deformation faults.

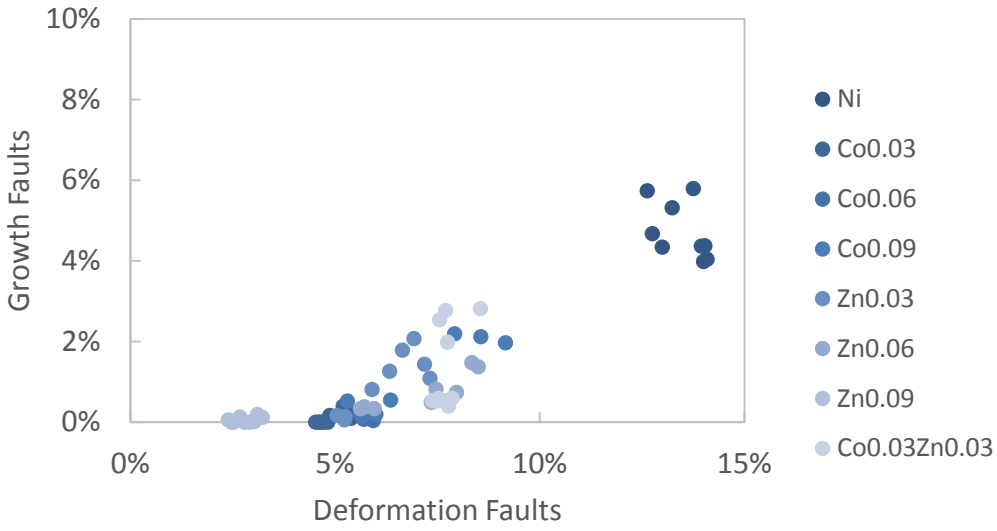

Figure 32. Plot of growth faults as a function of deformation faults

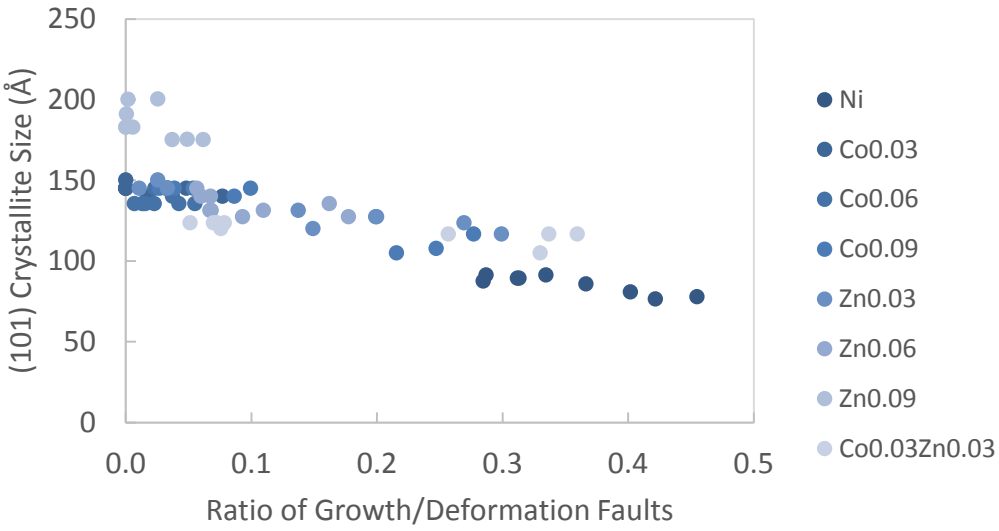

Figure 33. Plot of (101) crystallite size as a function of ratio of growth-to-deformation faults

5.4.3 Evolution of Stacking Faults over Precipitation Time

There is a clear effect of the initial precipitation time on the distribution of the stacking faults. The strong stirring during the precipitation process appears to impart enough energy at the precipitation conditions (temperature and pH) for a distribution of stacking faults to form a meta-stable state. The evolution of deformation faults over precipitation time is plotted in Figure 34,

grouped by Co additives, Zn additives, and 0.06 level substitution, respectively. The evolution of growth faults over precipitation time is plotted in Figure 35. The refinements show very limited outliers, with the exception of $Ni_{0.94}Co_{0.03}Zn_{0.03}(OH)_2$, which is previously noted to show a second phase.

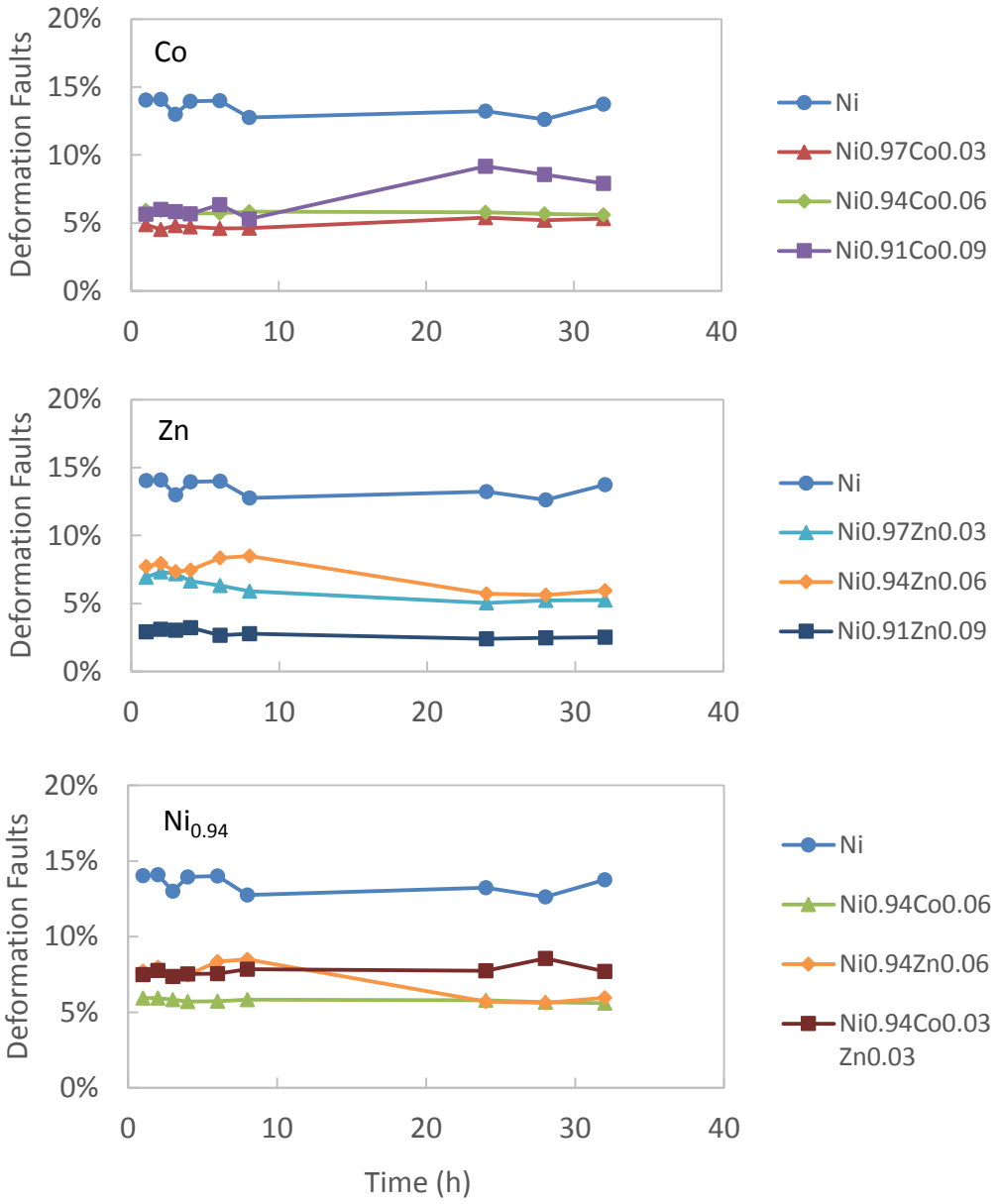

Figure 34. Evolution of deformation faults over precipitation time

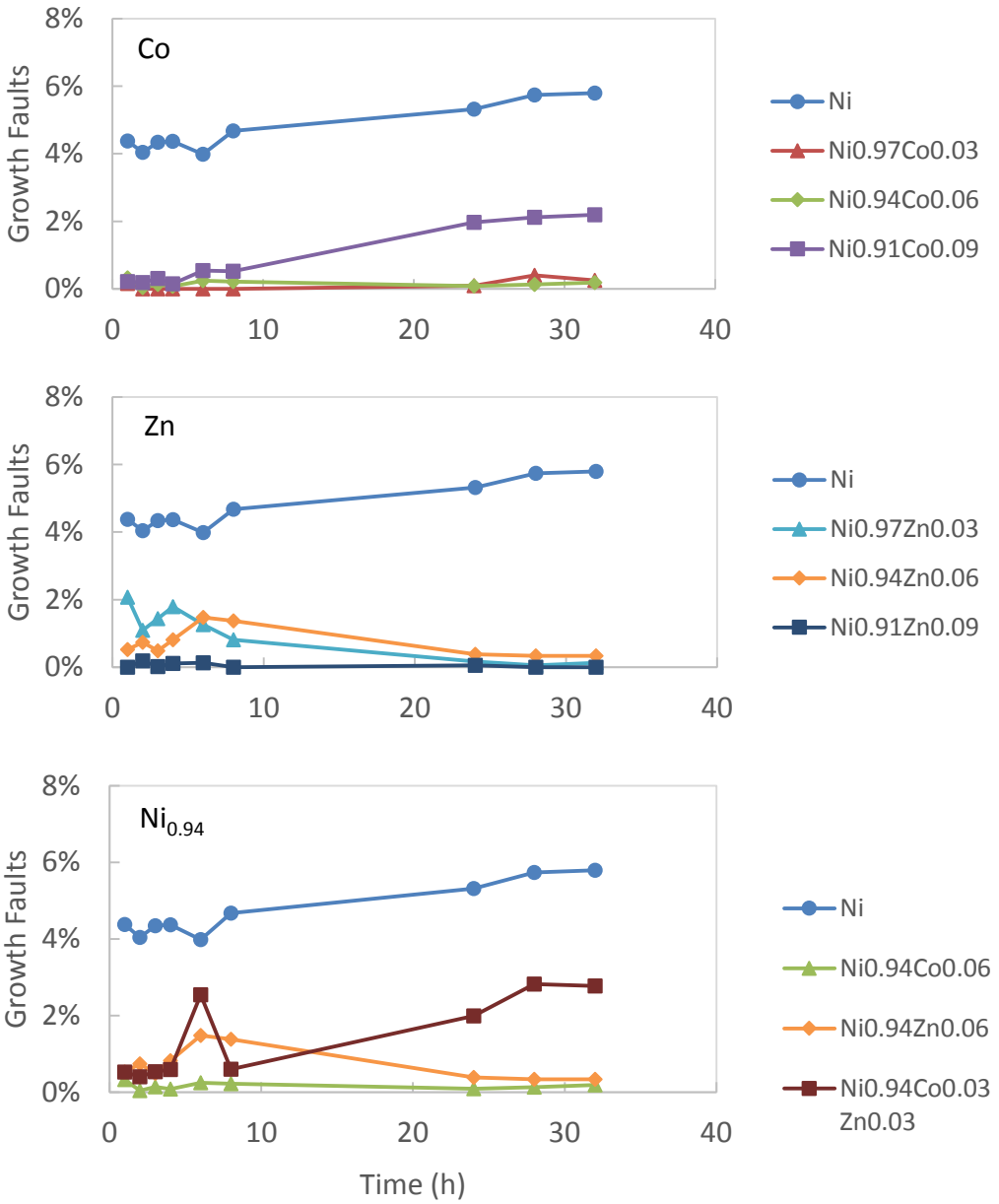

Figure 35. Evolution of growth faults over precipitation time

For the pure nickel hydroxide composition, generally there is little change in the percentage of deformation faults, and the increase in faulting arises from an increase of growth faults with precipitation time. Co additives appear to have a suppressive effect on both types of stacking faults, but a smaller suppressive effect is seen at a higher level of Co doping. Although the stacking faults levels are suppressed, in contrast to pure nickel hydroxide, the

$Ni_{0.91}Co_{0.09}(OH)_2$ composition shows both deformation and growth faults increasing with precipitation time, corresponding to the decrease in the (101) crystallite size. Zn additives show a suppressive effect at all levels of substitution, with both types of stacking faults decreasing with precipitation time. It suggests that Zn is also able to modify the energy barriers so that the energy from the precipitation process overshoots the meta-stable states to fall to the stable, more highly crystalline state. The combination of Co and Zn additives at the 0.06 substitution level shows a small suppressive effect on the stacking faults similar to Co. However, there is little change to the percentage of deformation faults with respect to precipitation time, but growth faults increase with longer precipitation times, contributing to the smaller (101) crystallite sizes seen over time. At the given experimental precipitation conditions, Co and Zn do not appear to promote the stacking faults needed for good electrochemical utilization; however, Co and Zn play other roles, in providing needed conductivity and suppressing the formation of γ-NiOOH [49]. Also, temperature and pH have an effect on the precipitation process, and further investigation into these conditions and how they affect the evolution of the stacking fault distribution for the various additives would be of interest.

5.5 Summary

Stacking faults in substituted nickel hydroxide spherical powders were studied using Rietveld refinement of PXRD patterns. Deformation and growth faults are noted to have strong correlations to the peak broadening of (101) and (102) diffraction peaks, which are also strongly correlated to electrochemical utilization for nickel hydroxide materials. Higher proportions of growth faults compared to deformation faults are shown to be correlated to smaller (101) crystallite sizes, even after controlling for total percentage of stacking faults. Depending on the additives, stacking faults tend to increase with precipitation time, but additives such as Zn can

affect the energy barriers so that precipitation conditions favor less stacking faults with precipitation time. Both Co and Zn suppress the percentage of stacking faults that occur in nickel hydroxide spherical powders, but a combination of Co and Zn allows the stacking faults to increase with precipitation time. We have shown through modeling of stacking faults how they may evolve with additives and precipitation time, which can be optimized to yield better electrochemical utilization in substituted nickel hydroxide spherical powders.

CHAPTER 6. EFFECTS OF LA AND ND ON SURFACE REACTIONS IN LAVES PHASE AB_2 ALLOYS

Nickel-metal hydride (NiMH) batteries are limited to −20°C operation, and therefore, it is a continuing effort to improve the ultra-low temperature performance [146]. The adoption of advanced start-stop technology in the automobile industry reduces fuel consumption and emissions in vehicles through the reduction of engine idling time; however, stand-alone battery systems require high cranking power at low temperature for this application. Panasonic has launched its 12V Energy Recovery System using NiMH battery cells [147], and system works in parallel with a start-stop lead-acid battery for multiple purposes: reclaiming braking energy, maintaining the spinning of engine and operation of auxiliary systems when the engine is shut down during idling, and restarting the engine when the driver lifts their foot from the brake pedal. Current NiMH battery technology does not have the cold cranking power that conventional lead-acid does [148], but the improved cycling performance of NiMH at elevated temperatures helps extend the service life of the lead-acid battery. Eliminating the need for the lead-acid battery reduces the complexity of the system while maintaining the extended service life and improvement to fuel economy. It is therefore highly attractive to improve the high-current, low-temperature performance of NiMH batteries for this application.

6.1 Background

NiCd rechargeable alkaline and NiMH batteries share similar electrolyte and positive electrodes, but NiCd has better low-temperature, high-power drain capability than NiMH [149]. The two negative electrode discharge half-cell reactions are very different:

$$\text{NiCd: } Cd + 2OH^- \rightarrow Cd(OH)_2 + 2e^-$$

$$\text{NiMH: } MH + OH^- \rightarrow M + H_2O + e^-$$

The creation of H_2O at the surface of the NiMH electrode dilutes the OH^- concentration and locally increases the freezing temperature of the electrolyte. A highly catalytic surface with channels to facilitate the movement of electrolyte becomes an important feature in negative electrode materials when considering a low-temperature operation [150, 151].

Transition metals, such as Cu [152], Mo [153], and Fe [154] modifiers improve the low-temperature performance of misch-metal-based AB_5 metal hydride (MH) alloys showing positive results, but sacrifices to properties such as cycle stability were also observed. AB_2 MH alloys, which are high-energy alternatives to AB_5 alloys, have shown lower −40°C charge-transfer resistance with additives such as Si [155], La [156], Y [146, 157], and Nd [158]. La and Nd additives in particular promote a secondary AB phase (where A is a rare earth element and B is mainly Ni) rather than entering and dissolving into the main phase, and this secondary phase has a great impact on the low-temperature performance of the alloys. In this study, we examine the surface reaction characteristics of La and Nd additives in AB_2 alloys at room temperature and −40°C in order to understand the catalytic activity and surface area contributions to the electrochemical reactions.

6.2 Experimental Setup

Alloy samples were prepared by arc melting using a tungsten electrode under continuous argon gas flow. EIS measurements were conducted using a Solartron 1250 Frequency Response Analyzer with sine wave of amplitude 10 mV and frequency range of 0.5 mHz to 10 kHz. Prior to the measurements, the electrodes were subjected to one full charge/discharge cycle at 0.1C rate using a Solartron 1470 Cell Test galvanostat, discharged to 80% state-of-charge, and then cooled to −40ºC.

6.3 Results and Discussion

Alloys of the compositions $Ti_{12}Zr_{22.8-x}V_{10}Cr_{7.5}Mn_{8.1}Co_{7.0}Ni_{32.2}Al_{0.4}La_x$, x = 0 to 5, where La substitutes for Zr, and $Ti_{12}Zr_{22.8-x}V_{10}Cr_{7.5}Mn_{8.1}Co_{7.0}Ni_{32.2}Al_{0.4}Nd_x$, x = 1 to 5, where Nd substitutes for Zr, were studied for their surface reaction characteristics using EIS measurements conducted at room temperature and −40°C. Structural characteristics, morphology, gaseous-phase properties and electrochemical performance properties for the two series of alloys are detailed in two previously published papers [156, 158]. In general, La-addition appears to promote a new LaNi phase, which improved the activation of the capacity and high-rate dischargeability (HRD) through a dramatic increase in surface area, which is also observed in scanning electron microscopy (SEM) images. Nd-addition also promotes a new NdNi phase as well as catalytic Zr_7Ni_{10} phase to improve capacity and HRD despite showing poor diffusion coefficient and exchange current density values. We use EIS measurements to examine the surface catalytic activity and the surface area contributions at room temperature and −40°C.

6.3.1 La Addition

Cole-Cole plots for the La-containing alloys obtained at room temperature are shown in Figure 36. Two semi-circles appear to emerge with increasing La-content, an indication of two distinct phases that participate in the electrochemistry. The charge-transfer resistance (R2 and R4) and double-layer capacitance (C1 and C2 respectively) of each phase were calculated from the Cole-Cole plots using the equivalent circuitry shown in Figure 37Figure 37. Equivalent circuit for La additive alloy samples. The values are listed in Table 17.

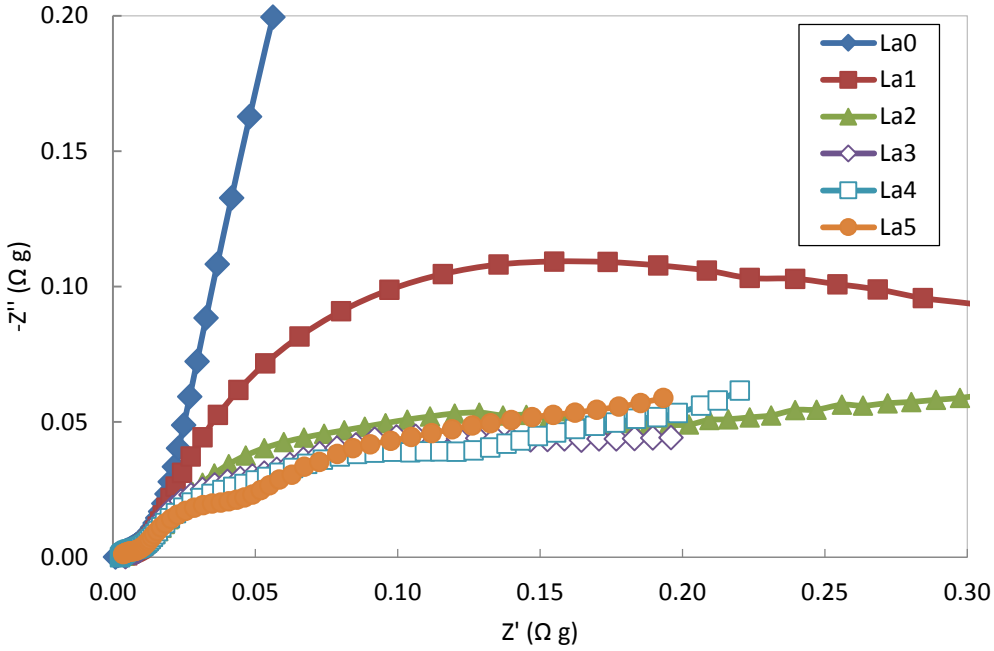

Figure 36. Cole-Cole plots for La additive alloy samples at room temperature

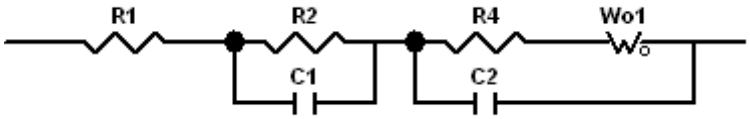

Figure 37. Equivalent circuit for La additive alloy samples

Table 17. Charge-transfer resistances and double layer capacitances calculated from equivalent circuitry for La additive alloys at room temperature and −40°C

Alloy	Room Temperature					−40°C				
	R1 (Ω g)	R2 (Ω g)	R4 (Ω g)	C1 (F g^{-1})	C2 (F g^{-1})	R1 (Ω g)	R2 (Ω g)	R4 (Ω g)	C1 (F g^{-1})	C2 (F g^{-1})
La0	0.03		4.87		0.36	0.57		158.55		0.18
La1	0.02	0.17	0.18	3.24	0.25	0.76	4.07	154.88	1.69	1.02
La2	0.02	0.10	0.08	4.14	0.31	0.41	9.64	5.62	2.59	0.31
La3	0.01	0.07	0.04	5.03	0.43	0.28	10.40	4.43	4.20	0.48
La4	0.02	0.06	0.04	6.18	0.51	0.28	9.45	3.25	7.12	0.53
La5	0.01	0.06	0.03	10.62	0.53	0.27	7.31	3.69	6.75	0.57

The base alloy La0 exhibits only a single semi-circle in the Cole-Cole plot, indicating one mostly uniform phase, and therefore only R4 and C2 are calculated for La0. With the exception

of La1 at −40°C, which has very large impedance in the data and unable to measure down to the diffusion region of the spectrum, the charge-transfer resistance of both phases generally decreases with the addition of La-content for each of the temperatures measured. The drop in charge-transfer resistance is most dramatically seen in the second phase associated with R4. The double-layer capacitance on the other hand increases at a rate one order of magnitude larger for the first phase than for the second phase, and this observation is consistently reflected at both −40°C and room temperature. SEM images of the alloy samples clearly show pulverization of the LaNi phase [156], and since the double-layer capacitance is proportional to the reactive surface area in electrochemistry, it is likely that the R2 and C1 are associated with the LaNi phase and the R4 and C2 are associated with the main C14 phase. The series circuit elements R2 and R4 are added together to obtain the overall charge-transfer resistance of each alloy. The overall charge-transfer resistance drops with increasing La-content, which is in agreement with improved HRD performance. The lowest overall charge-transfer resistance measured at −40°C was from the alloy with the highest La-content (La5) with a resistance of 11 Ω g. Compared to the charge-transfer resistance from commercial AB_5 material (5.4 Ω g) [153], the resistance of the alloys is high, but individually the R4 of the C14 phase was able to drop its resistance down to 3.25 Ω g. Overall, La5 has one of the lowest charge transfer resistances for AB_2 alloys that we have tested thus far at −40°C, followed by Si-doped AB_2 alloy with a charge-transfer resistance of 12 Ω g [155].

The sum of the product of the charge-transfer resistance and double-layer capacitance for each phase is plotted against La-content in Figure 38. The product removes the surface area contribution from the catalytic activity, and the sum of the product reflects the series behavior of each phase. The overall product does not show improvement in surface catalytic capability at

−40°C with La-addition, but the sum is dominated by the LaNi phase contribution, which displays high pulverization. The C14 phase contribution, however, is greatly reduced with La-addition. The surface catalytic ability in the main C14 phase appears to contribute to the improvement of the overall charge-transfer resistance.

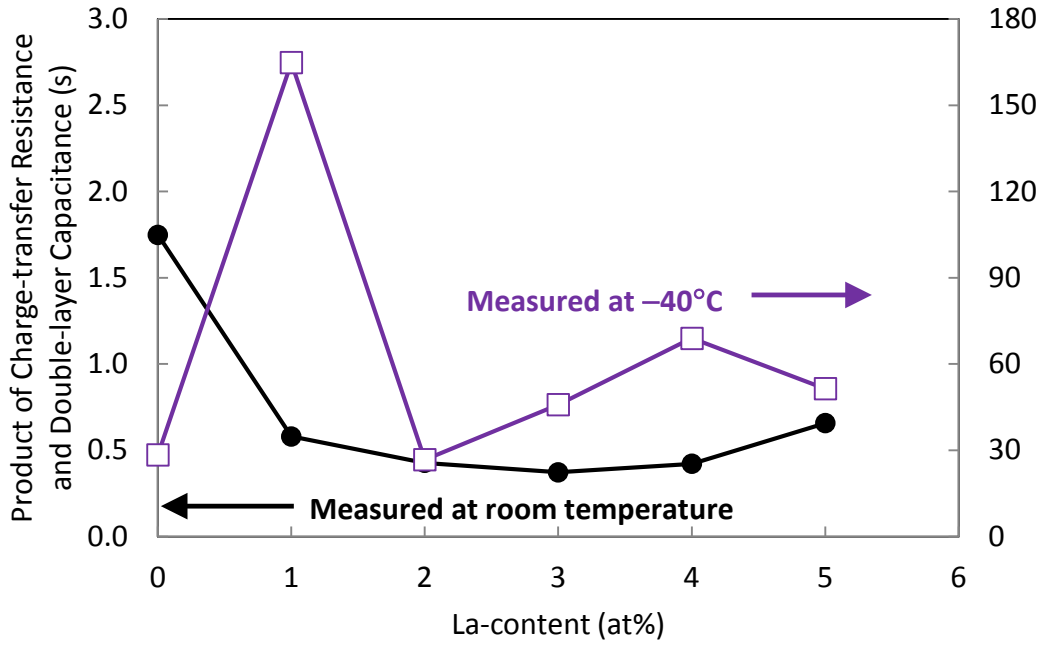

Figure 38. Product of charge-transfer resistance and double-layer capacitance for La additive alloys measured at room temperature and −40°C

6.3.2 Nd Addition

Cole-Cole plots obtained at −40°C are shown in Figure 39. In contrast to the La-additive alloy, the Nd-additive alloys only show a single semi-circle, indicating that the phases behave similarly. The Nd-additive alloys also show less pulverization than the La-additive alloys [158]. The charge-transfer resistance and double-layer capacitance calculated from the impedance spectra based on the Randles circuit are listed in Table 18. The charge-transfer resistances drop dramatically with Nd incorporated into the alloys, and this is reflected in the improvement in HRD. However, there is a more gradual improvement in HRD with Nd-content, while the charge-transfer resistances appear to change comparatively little after the initial introduction.

The Nd-containing alloys have similar overall charge-transfer resistance values to the La-containing alloys. The lowest overall charge-transfer resistance measured at −40°C is 8.9 Ω g for the Nd4 sample, and this value is the lowest we have measured for AB_2-based alloys, however, the value is still higher than 5.4 Ω g obtained from a commercially available AB_5 alloy [153]. The double-layer capacitance, which is proportional to the reactive surface area, shows an initial decrease with Nd-content at room temperature, increases with additional Nd-content, and finally drops again when the Nd-content reaches 5 at%. At −40°C, the double-layer capacitance starts low and increases until the Nd-content reaches 4 at%, and then drops at 5 at%. The charge-transfer resistance and double-layer capacitance values are obtained from equivalent circuit fitting, and impedance spectra for room temperature experiments are able to capture a more complete picture of frequency response behavior for the same frequency range. Thus, the room temperature trends for double-layer capacitance would better reflect the trends in reactive surface area for the alloys.

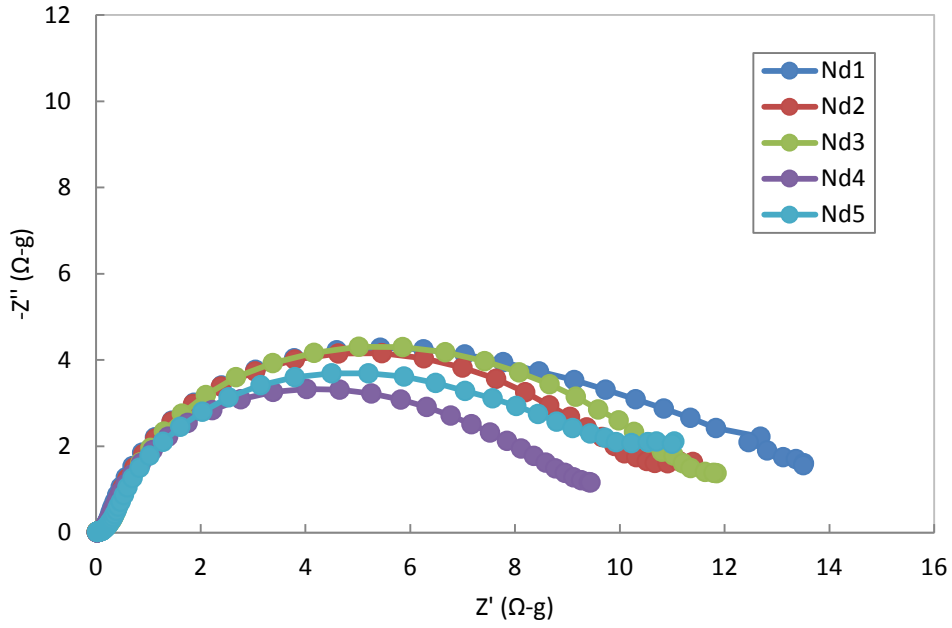

Figure 39. Cole-Cole plots for Nd additive alloy samples at −40°C

Table 18. Charge-transfer resistances and double layer capacitances calculated from equivalent circuitry for Nd additive alloys at room temperature and −40°C

	Charge-transfer resistance @ RT (Ω g)	Double-layer capacitance @ RT (F g^{-1})	Charge-transfer resistance @ –40°C (Ω g)	Double-layer capacitance @ –40°C (F g^{-1})
Nd1	0.12	0.31	12.33	0.36
Nd2	0.12	0.21	10.55	0.42
Nd3	0.11	0.18	11.14	0.48
Nd4	0.10	0.28	8.90	0.53
Nd5	0.12	0.04	10.30	0.27

The product of the charge-transfer resistance and the double layer capacitance is also plotted against the Nd-content in Figure 40. This product removes the contribution from the surface area and shows a marked improvement in surface catalytic capability at −40°C with the incorporation of Nd-content. It appears that the surface catalytic capability helps improve the charge-transfer resistance of the Nd-containing alloys. The reason we do not observe a stepwise increase in HRD is likely due to the higher resistance to diffusion in the Nd-containing alloys combined with the proportion of highly catalytic NdNi phase at the surface. There is a small proportion of NdNi phase in Nd1 alloy that is likely insufficient to overcome the increased diffusion resistance, but as the Nd-content increases, higher proportions of NdNi phase in the other alloy samples promotes more low resistance paths to the surface for the electrochemical reaction to take place more quickly, which is reflected in the incremental increase in HRD. While TiNi and Zr_7Ni_{10} secondary phases are also present in the study, they do not appear to play as large of a role regarding surface catalytic capability as the NdNi phase. TiNi phase appears in the base Nd-free alloy, which shows poorer surface catalytic capability and HRD performance. TiNi and Zr_7Ni_{10} phases both appear in Cu- and Y-modifier AB_2 alloy studies without the dramatic increase in surface catalytic capability [80, 152], and the increase in Zr_7Ni_{10} phase appeared to lower the surface catalytic capability. La-modified AB_2 alloys with LaNi phase

(perhaps similar to NdNi phase) in smaller proportions show a similar dramatic increase in surface catalytic capability without observable Zr_7Ni_{10} phase [156]. This suggests that the NdNi phase in this study, in sufficient quantities, is responsible for overcoming the increased diffusion resistance and improving the HRD performance.

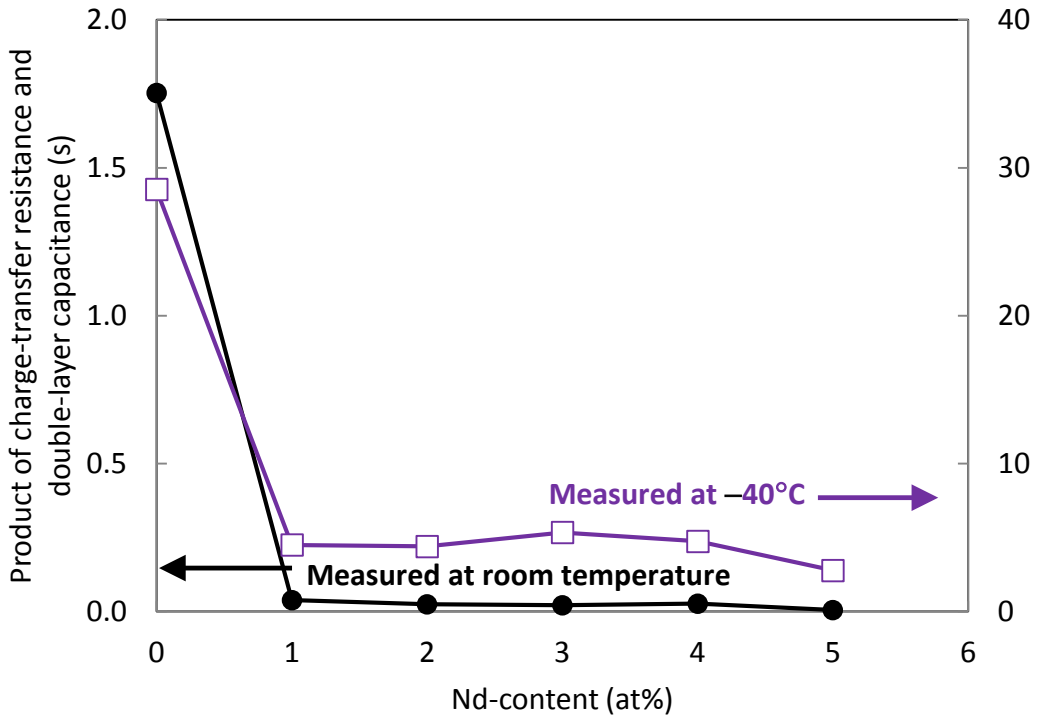

Figure 40. Product of charge-transfer resistance and double-layer capacitance for Nd additive alloys measured at room temperature and −40°C

6.4 Summary

The surface reaction characteristics of La and Nd additives in AB_2 alloys at room temperature and –40°C were studied using EIS measurements and analysis in order to understand the catalytic activity and surface area contributions to the electrochemical reactions. EIS studies show the behavior of two distinct phases in La-containing alloys, attributed to main phase and the pulverization-prone LaNi phase. At −40°C, the charge-transfer resistance of the La-containing alloys decreases as a result of increased catalytic ability in the main phase, but

overall catalytic ability is overshadowed by the high surface area of the LaNi phase. Nd-containing alloys show very low charge-transfer resistance with high catalytic capability in the Nd-containing alloys without the pulverization issues. The highly catalytic nature of NdNi-phase appears to dominate the HRD performance. Small amounts of rare-earth additives appear promising for improving low temperature performance by introducing highly catalytic phases.

CHAPTER 7. CONCLUSIONS

7.1 Conclusions

The electrochemical system of the NiMH battery is a complex, yet elegant system that is dynamic collection of disordered, multi-compositional phases that interact to store and release electrical energy. This body of work has highlighted various computational methods and simulation techniques and the ways they can be used to better understand and characterize high-performance nickel-metal hydride battery materials to address important energy storage needs such as storage capacity, high-rate dischargeability, low temperature performance, cycle stability, and electrochemical efficiency.

C14/C15 Laves phase structure determination is important for the design of NiMH battery anode materials, as each phase can play a role in different aspects of battery performance. We were able to use first-principle DFT calculations to confirm a semi-empirical model for C14/C15 Laves phase structure determination for simple binary compounds, and extended the model for more ternary compounds, using the $Mg(Cu_{1-x}Zn_x)_2$ system, improving the resolution of the model. We determined that the electronic contributions to energy correlate to the semi-empirical methods, but vibrational contributions play a larger role at the C14/C15 energy thresholds.

Cycle stability of NiMH anode materials is strongly correlated to pressure-concentration-temperature isotherm hysteresis measurements, a measure of irreversible losses such as plastic deformation upon hydrogenation and dehydrogenation, and alloy pulverization plays a key pathway for the degradation. We used first-principle DFT calculations to model the initial hydrogenation of AB_5-type and AB_2-type alloys, yielding the initial lattice expansions upon hydrogenation, and correlating to the hysteresis trends. Lattice expansion and phase

transformation induces microstrains at the phase interfaces, which can plasticly shear or create microcracks, depending on the nature of the alloy, initiating the pulverization process. Understanding this dynamic process more fully allows researchers to design materials that cycle longer while maintaining other aspects of its performance.

The electrochemical utilization of nickel hydroxide materials is a measure of the electrochemical efficiency, which is directly correlated to structural defects observed through the broadening of (*h*0*l*) diffraction peaks. Stacking faults direct interrupt (*h*0*l*) plane periodicity, and through Rietveld refinement and DIFFaX modeling of the different types of stacking faults, we tracked the evolution of the stacking faults over precipitation time for different compositions. We determined which types of stacking faults have a stronger effect on the (101) peak, and the conditions that promote the formation of each type of stacking fault.

Low-temperature performance of NiMH batteries can be improved by dopants to AB_2 anode materials, and La and Nd are particularly promising additives that improve both the storage capacity and high-rate dischargeability. We used equivalent circuit modeling of electrochemical impedance spectra to understand the nature of the electrochemical reactions occurring on the surface the alloys. The charge-transfer resistance of the La-containing alloys decreases as a result of increased catalytic ability in the main phase, but overall catalytic ability is overshadowed by the high surface area of the LaNi phase. Nd-containing alloys show very low charge-transfer resistance with high catalytic capability without the pulverization issues. The highly catalytic nature of NdNi-phase appears to dominate the high-rate dischargeability performance. Small amounts of rare-earth additives such as La and Nd appear promising for improving low temperature performance by introducing highly catalytic phases.

7.2 Future Work

This work highlights various ways computer modeling and simulation can be used to study and improve NiMH battery materials, and the field is rife with opportunity to leverage computing power to accelerate much needed research and development. Future work can expand to include the modeling of a third class of NiMH anode materials, A_2B_7 MH alloys, which exhibit excellent storage, power, and cycling abilities. Understanding the lattice expansion behavior of these materials can offer additional insight to improving pulverization resistance and cycle stability. Ground work for modeling hydrogen diffusion behavior of $LaNi_5$ materials using nudged elastic band DFT calculations is available in literature, and investigating the effect of additives on the diffusion activation energy pathways offer insight to improve high-rate discharge characteristics, which can extend to AB_2 and A_2B_7 materials as well. Computational and modeling methods are powerful tools that can assist researchers in developing materials to meet energy storage needs.

REFERENCES

[1] G. Ceder, Y.M. Chiang, D.R. Sadoway, M.K. Aydinol, Y.I. Jang, B. Huang, Nature 392 (1998) 694-696.

[2] G. Ceder, MRS Bulletin 35 (2010) 693-701.

[3] R. Schmitt, U.S. Patent 3972726, 1976.

[4] K. Young, J. Nei, Materials 6 (2013) 4574-4608.

[5] S.R. Ovshinsky, M.A. Fetcenko, J. Ross, Science 260 (1993) 176-181.

[6] F. Stein, MRS Online Proceedings Library 1295 (2011).

[7] D.P. Shoemaker, C.B. Shoemaker, Journal of the Less-Common Metals 68 (1979) 43-58.

[8] S. Hong, C.L. Fu, Physical Review B 66 (2002) 094109.

[9] F. Li, J. Zhao, D. Tian, H. Zhang, X. Ke, B. Johansson, Journal of Applied Physics 105 (2009) 043707.

[10] J. Radaković, J. Belošević-Čavor, V. Koteski, International Journal of Hydrogen Energy 38 (2013) 9229-9235.

[11] D.G. Westlake, Journal of the Less-Common Metals 90 (1983) 251-273.

[12] Q. Zhang, Y. Lei, X. Yang, K. Ren, Q. Wang, J. Alloy. Compd. 292 (1999) 236-240.

[13] Q.A. Zhang, Y.Q. Lei, X.G. Yang, K. Ren, Q.D. Wang, J. Alloy. Compd. 292 (1999) 241-246.

[14] W.K. Zhang, C.A. Ma, X.G. Yang, Y.Q. Lei, Q.D. Wang, G.L. Lu, J. Alloy. Compd. 293 (1999) 691-697.

[15] K. Young, M.A. Fetcenko, J. Koch, K. Morii, T. Shimizu, J. Alloy. Compd. 486 (2009) 559-569.

[16] K. Young, T. Ouchi, B. Huang, B. Chao, M.A. Fetcenko, L.A. Bendersky, K. Wang, C. Chiu, J. Alloy. Compd. 506 (2010) 841-848.

[17] K. Young, J. Nei, T. Ouchi, M.A. Fetcenko, J. Alloy. Compd. 509 (2011) 2277-2284.

[18] R.L. Berry, G.V. Raynor, Acta Crystallographica 6 (1953) 178-186.

[19] J.H. Zhu, P.K. Liaw, C.T. Liu, Materials Science and Engineering a-Structural Materials Properties Microstructure and Processing 240 (1997) 260-264.

[20] J.H. Zhu, C.T. Liu, P.K. Liaw, Intermetallics 7 (1999) 1011-1016.

[21] J.H. Zhu, C.T. Liu, L.M. Pike, P.K. Liaw, Metallurgical and Materials Transactions a-Physical Metallurgy and Materials Science 30 (1999) 1449-1452.

[22] J.H. Zhu, C.T. Liu, L.M. Pike, P.K. Liaw, Intermetallics 10 (2002) 579-595.

[23] R.L. Johnston, R. Hoffmann, Zeitschrift für anorganische und allgemeine Chemie 616 (1992) 105-120.

[24] F. Stein, M. Palm, G. Sauthoff, Intermetallics 12 (2004) 713-720.

[25] F. Stein, M. Palm, G. Sauthoff, Intermetallics 13 (2005) 1056-1074.

[26] R.T. Macaluso, B.K. Greve, Dalton Transactions 41 (2012) 14225-14235.

[27] J. Nei, K. Young, S.O. Salley, K.Y.S. Ng, Mater. Chem. Phys. 136 (2012) 520-527.

[28] P. Oliva, J. Leonardi, J. Laurent, C. Delmas, J. Braconnier, M. Figlarz, F. Fievet, A.d. Guibert, J. Power Sources 8 (1982) 229-255.

[29] C. Delmas, C. Tessier, J. Mater. Chem. 7 (1997) 1439-1443.

[30] A. Szytula, A. Murasik, M. Balanda, Phys. Status Solidi B 43 (1971) 125-128.

[31] M. Terasaka, M. Kanbayashi, T. Shiojiri, Jpn. Patent H03-196588, 1993.

[32] M.C. Bernard, R. Cortes, M. Keddam, H. Takenouti, P. Bernard, S. Senyarich, J. Power Sources 63 (1996) 247-254.

[33] C. Tessier, P.H. Haumesser, P. Bernard, C. Delmas, J. Electrochem. Soc. 146 (1999) 2059-2067.

[34] M.M.J. Treacy, J.M. Newsam, M.W. Deem, Proc. R. Soc. A 433 (1991) 499-520.

[35] M. Casas-Cabanas, J. Rodriguez-Carvajal, M.R. Palacin, Z. Kristallogr. (2006) 243-248.

[36] M. Casas-Cabanas, M.R. Palacin, J. Rodriguez-Carvajal, Powder Diffraction 20 (2005) 334-344.

[37] M. Casas-Cabanas, J. Rodriguez-Carvajal, J. Canales-Vazquez, M.R. Palacin, J. Mater. Chem. 16 (2006) 2925-2939.

[38] M. Casas-Cabanas, J. Rodriguez-Carvajal, J. Canales-Vazquez, Y. Laligant, P. Lacorre, M.R. Palacin, J. Power Sources 174 (2007) 414-420.

[39] T.N. Ramesh, R.S. Jayashree, P.V. Kamath, Clays and Clay Minerals 51 (2003) 570-576.

[40] T.N. Ramesh, P.V. Kamath, C. Shivakumara, Acta Crystallogr. Sect. B-Struct. Sci. 62 (2006) 530-536.

[41] T.N. Ramesh, P.V. Kamath, Mater. Res. Bull. 43 (2008) 3227-3233.

[42] T.N. Ramesh, Mater. Chem. Phys. 114 (2009) 618-623.

[43] M.N. Tripathi, U.V. Waghmare, T.N. Ramesh, P.V. Kamath, J. Electrochem. Soc. 157 (2010) A280-A284.

[44] P. Hermet, L. Gourrier, J.-L. Bantignies, D. Ravot, T. Michel, S. Deabate, P. Boulet, F. Henn, Physical Review B 84 (2011) 235211.

[45] T.N. Ramesh, P.V. Kamath, J. Solid State Electrochem. 13 (2009) 763-771.

[46] M. Oshitani, K. Hasegawa, H. Yufu, U.S. Patent 4985318, 1991.

[47] M. Oshitani, H. Yufu, K. Takashima, S. Tsuji, Y. Matsumaru, J. Electrochem. Soc. 136 (1989) 1590-1593.

[48] X.Y. Wang, J. Yan, H.T. Yuan, Y.S. Zhang, D.Y. Song, International Journal of Hydrogen Energy 24 (1999) 973-980.

[49] J. Chen, D.H. Bradhurst, S.X. Dou, H.K. Liu, J. Electrochem. Soc. 146 (1999) 3606-3612.

[50] M. Casas-Cabanas, J.C. Hernandez, V. Gil, M.L. Soria, M.R. Palacin, J. Power Sources 134 (2004) 298-307.

[51] Z.R. Chang, G.G. Li, Y.J. Zhao, J.G. Chen, Y.C. Ding, J. Power Sources 74 (1998) 252-254.

[52] C. Liu, Y. Li, P. Li, C. Xing, Mater. Res. Bull. 45 (2010) 2001-2005.

[53] R.M. Martin, Electronic Structure: Basic Theory and Practical Methods, Cambridge University Press, 2004.

[54] F. Jensen, Introduction to Computational Chemistry, John Wiley & Sons, 2013.

[55] M. Born, R. Oppenheimer, Annalen der Physik 389 (1927) 457-484.

[56] P. Hohenberg, W. Kohn, Physical Review 136 (1964) B864.

[57] W. Kohn, L.J. Sham, Physical Review 140 (1965) A1133.

[58] P.H.T. Philipsen, E.J. Baerends, Physical Review B 54 (1996) 5326-5333.

[59] A.D. Becke, Physical Review A 38 (1988) 3098.

[60] J.P. Perdew, Y. Wang, Physical Review B 33 (1986) 8800-8802.

[61] J.P. Perdew, Electronic Structure of Solids' 91, Akademie Verlag, Berlin, 1991.

[62] J.P. Perdew, K. Burke, M. Ernzerhof, Physical Review Letters 77 (1996) 3865-3868.

[63] H.P. Klug, L.E. Alexander, X-ray Diffraction Procedures, John Wiley & Sons, Inc., New York, 1974.

[64] M.E. Orazem, B. Tribollet, Electrochemical Impedance Spectroscopy, John Wiley & Sons, Inc., New Jersey, 2008.

[65] P. Giannozzi, S. Baroni, N. Bonini, M. Calandra, R. Car, C. Cavazzoni, D. Ceresoli, G.L. Chiarotti, M. Cococcioni, I. Dabo, Journal of Physics: Condensed Matter 21 (2009) 395-502.

[66] A. Kokalj, Computational Materials Science 28 (2003) 155-168.

[67] K.F. Garrity, J.W. Bennett, K.M. Rabe, D. Vanderbilt, Computational Materials Science 81 (2014) 446-452.

[68] K. Young, J. Nei, D. Wong, L. Wang, International Journal of Hydrogen Energy 39 (2014) 21489-21499.

[69] K. Young, D. Wong, J. Nei, B. Reichman, J. Alloy. Compd. 643 (2015) 17-27.

[70] K. Young, D. Wong, S. Yasuoka, J. Ishida, J. Nei, J. Koch, J. Power Sources 251 (2014) 170-177.

[71] K. Young, T. Ouchi, L. Wang, D. Wong, J. Power Sources 279 (2015) 172-179.

[72] K. Young, D. Wong, L. Wang, J. Nei, T. Ouchi, S. Yasuoka, J. Power Sources 277 (2015) 426-432.

[73] K. Young, D. Wong, L. Wang, J. Alloy. Compd. 622 (2015) 885-893.

[74] G.W. Shannette, J.F. Smith, Journal of Applied Physics 42 (1971) 2799-2803.

[75] H. Klee, H. Witte, Z. Phys. Chem. Leipzig 202 (1954) 352-377.

[76] M.A. Fetcenko, S.R. Ovshinsky, K. Young, B. Reichman, C. Fierro, J. Koch, F. Martin, W. Mays, T. Ouchi, B. Sommers, A. Zallen, J. Alloys Compd. 330 (2002) 752-759.

[77] K. Young, M.A. Fetcenko, T. Ouchi, F. Li, J. Koch, J. Alloys Compd. 469 (2009) 406-416.

[78] W.J. Boettinger, D.E. Newbury, K. Wang, L.A. Bendersky, C. Chiu, U.R. Kattner, K. Young, B. Chao, Metall. Mater. Trans. A 41 (2010) 2033-2047.

[79] L.A. Bendersky, K. Wang, W.J. Boettinger, D.E. Newbury, K. Young, B. Chao, Metall. Mater. Trans. A 41 (2010) 1891-1906.

[80] K. Young, M. Young, T. Ouchi, B. Reichman, M.A. Fetcenko, J. Power Sources 215 (2012) 279-287.

[81] K. Young, T. Ouchi, B. Huang, B. Reichman, R. Blankenship, J. Alloys Compd. 575 (2013) 65-72.

[82] K. Young, D.F. Wong, S. Yasuoka, J. Ishida, J. Nei, J. Koch, J. Power Sources 251 (2014) 170-177.

[83] J.J.G. Willems, K.H.J. Buschow, J. Less-Comm. Met. 129 (1987) 13-30.

[84] T. Sakai, T. Hazama, H. Miyamura, N. Kuriyama, A. Kato, H. Ishikawa, J. Less-Comm. Met. 172 (1991) 1175-1184.

[85] P.H.L. Notten, R.E.F. Einerhand, J.L.C. Daams, J. Alloys Compd. 231 (1995) 604-610.

[86] J.J. Reilly, G.D. Adzic, J.R. Johnson, T. Vogt, S. Mukerjee, J. McBreen, J. Alloys Compd. 293 (1999) 569-582.

[87] T. Sakai, K. Oguro, H. Miyamura, N. Kuriyama, A. Kato, H. Ishikawa, C. Iwakura, J. Less-Comm. Met. 161 (1990) 193-202.

[88] Y. Osumi, H. Suzuki, A. Kato, K. Oguro, M. Nakane, Nippon Kagaku Kaishi (1981) 1493-1502.

[89] T. Sakai, H. Miyamura, N. Kuriyama, A. Kato, K. Oguro, H. Ishikawa, C. Iwakura, J. Less-Comm. Met. 159 (1990) 127-139.

[90] F. Meli, A. Züttel, L. Schlapbach, Journal of alloys and compounds 190 (1992) 17-24.

[91] T. Sakai, H. Miyamura, N. Kuriyama, A. Kato, K. Oguro, H. Ishikawa, Journal of the Electrochemical Society 137 (1990) 795-799.

[92] J.M. Joubert, M. Latroche, R. Cerny, A. Percheron-Guegan, K. Yvon, J. Alloys Compd. 330 (2002) 208-214.

[93] H.H. Cheng, H.G. Yang, S.L. Li, X.X. Deng, D.M. Chen, K. Yang, J. Alloys Compd. 453 (2008) 448-452.

[94] K. Suzuki, K. Ishikawa, K. Aoki, Mater. Trans., JIM 41 (2000) 581-584.

[95] S. Luo, T.B. Flanagan, R.C. Bowman, J. Alloys Compd. 330 (2002) 531-535.

[96] R.C. Bowman, C.H. Luo, C.C. Ahn, C.K. Witham, B. Fultz, J. Alloys Compd. 217 (1995) 185-192.

[97] E.M. Borzone, M.V. Blanco, A. Baruj, G.O. Meyer, Int. J. of Hydrogen Energy 39 (2014) 8791-8796.

[98] J. Matsuda, Y. Nakamura, E. Akiba, J. Alloys Compd. 509 (2011) 7498-7503.

[99] M. Mendelsohn, D. Gruen, A. Dwight, Inorg. Chem. 18 (1979) 3343-3345.

[100] E.A. Kumar, M.P. Maiya, S.S. Murthy, B. Viswanathan, J. Alloys Compd. 476 (2009) 92-97.

[101] Y. Osumi, H. Suzuki, A. Kato, K. Oguro, S. Kawai, M. Kaneko, J. Less-Comm. Met. 89 (1983) 287-292.

[102] Y. Osumi, Suiso Kyuzou Goukin, new ed., AGNE Gijutsu Center, Tokyo, Japan, 1999, p.218.

[103] K. Young, T. Ouchi, M.A. Fetcenko, J. Alloys Compd. 480 (2009) 428-433.

[104] K. Young, T. Ouchi, W. Mays, B. Reichman, M.A. Fetcenko, J. Alloys Compd. 480 (2009) 434-439.

[105] K. Young, T. Ouchi, M.A. Fetcenko, J. Alloy. Compd. 480 (2009) 440-448.

[106] L.G. Hector, J.F. Herbst, T.W. Capehart, J. Alloy. Compd. 353 (2003) 74-85.

[107] K. Tatsumi, I. Tanaka, H. Inui, K. Tanaka, M. Yamaguchi, H. Adachi, Phys. Rev. B 64 (2001) 184105.

[108] H. Nakamura, D. Nguyen-Manh, D.G. Pettifor, J. Alloy. Compd. 281 (1998) 81-91.

[109] M. Gupta, J. Less-Comm. Met. 130 (1987) 219-228.

[110] V. Paul-Boncour, M. Gupta, J.M. Joubert, A. Percheron-Guegan, P. Parent, C. Laffon, J. Mater. Chem. 10 (2000) 2741-2747.

[111] A. Tezuka, H. Wang, H. Ogawa, T. Ikeshoji, Phys. Rev. B 81 (2010) 134304.

[112] C. Lartigue, A. Lebail, A. Percheron-Guégan, J. Less-Comm. Met. 129 (1987) 65-76.

[113] N. Nagasako, A. Fukumoto, K. Miwa, Phys. Rev. B 66 (2002) 155106.

[114] X.Q. Chen, V.T. Witusiewicz, R. Podloucky, P. Rogl, F. Sommer, Acta Mater. 51 (2003) 1239-1247.

[115] Z.-S. Nong, J.-C. Zhu, Y. Cao, X.-W. Yang, Z.-H. Lai, Y. Liu, Physica B 419 (2013) 11-18.

[116] A. Percheron-Guégan, C. Lartigue, J.C. Achard, P. Germi, F. Tasset, J. Less-Comm. Met. 74 (1980) 1-12.

[117] T. Gamo, Y. Moriwaki, N. Yanagihara, T. Yamashita, T. Iwaki, Int. J. of Hydrogen Energy 10 (1985) 39-47.

[118] L. Wang, K. Young, J. Nei, D. Pawlik, K.Y.S. Ng, J. Alloys Compd. 616 (2014) 300-305.

[119] D. Fruchart, J.L. Soubeyroux, R. Hempelmann, J. Less-Comm. Met. 99 (1984) 307-319.

[120] K. Momma, F. Izumi, J. Appl. Crystallogr. 44 (2011) 1272-1276.

[121] P. Giannozzi, S. Baroni, N. Bonini, M. Calandra, R. Car, C. Cavazzoni, D. Ceresoli, G.L. Chiarotti, M. Cococcioni, I. Dabo, A. Dal Corso, S. de Gironcoli, S. Fabris, G. Fratesi, R. Gebauer, U. Gerstmann, C. Gougoussis, A. Kokalj, M. Lazzeri, L. Martin-Samos, N.

Marzari, F. Mauri, R. Mazzarello, S. Paolini, A. Pasquarello, L. Paulatto, C. Sbraccia, S. Scandolo, G. Sclauzero, A.P. Seitsonen, A. Smogunov, P. Umari, R.M. Wentzcovitch, J. Phys. Condens. Matter 21 (2009) 395502.

[122] K.F. Garrity, J.W. Bennett, K.M. Rabe, D. Vanderbilt, Comput. Mater. Sci. 81 (2014) 446-452.

[123] J.P. Perdew, J.A. Chevary, S.H. Vosko, K.A. Jackson, M.R. Pederson, D.J. Singh, C. Fiolhais, Phys. Rev. B 46 (1992) 6671-6687.

[124] H.H. Van Mal, K.H.J. Buschow, A.R. Miedema, Journal of the Less Common Metals 35 (1974) 65-76.

[125] H. Zhou, Q. Yao, S. Yuan, J. Liu, H. Deng, Journal of Alloys and Compounds 366 (2004) 161-164.

[126] M.L. Wasz, R.B. Schwarz, S. Srinivasan, M.S. Kumar, in: MRS Proceedings, Cambridge Univ Press, 1995, pp. 237.

[127] J.J. Murray, M.L. Post, J.B. Taylor, Journal of the Less Common Metals 80 (1981) 201-209.

[128] E. Akiba, K. Nomura, S. Ono, J. Less-Comm. Met. 129 (1987) 159-164.

[129] K.J. Gross, A. Züttel, L. Schlapbach, J. Alloys Compd. 274 (1998) 239-247.

[130] Y. Nakamura, K. Sato, S. Fujitani, K. Nishio, K. Oguro, I. Uehara, J. Alloys Compd. 267 (1998) 205-210.

[131] K. Tanaka, S. Okazaki, T. Ichitsubo, T. Yamamoto, H. Inui, M. Yamaguchi, M. Koiwa, Intermetallics 8 (2000) 613-618.

[132] K. Tatsumi, I. Tanaka, K. Tanaka, H. Inui, M. Yamaguchi, H. Adachi, M. Mizuno, J. Phys. Condens. Matter 15 (2003) 6549-6561.

[133] Z.-S. Nong, J.-C. Zhu, X.-W. Yang, Y. Cao, Z.-H. Lai, Y. Liu, W. Sun, Solid State Sci. 32 (2014) 1-7.

[134] X.Q. Chen, W. Wolf, R. Podloucky, P. Rogl, M. Marsman, Phys. Rev. B 72 (2005) 054440.

[135] X.Q. Chen, W. Wolf, R. Podloucky, R. Rogl, Phys. Rev. B 71 (2005) 174101.

[136] J. Cho, Y.J. Kim, T.J. Kim, B. Park, Angewandte Chemie-International Edition 40 (2001) 3367-3369.

[137] Y. Qi, L.G. Hector, Jr., C. James, K.J. Kim, Journal of the Electrochemical Society 161 (2014) F3010-F3018.

[138] K. Sakaki, E. Akiba, M. Mizuno, H. Araki, Y. Shirai, Journal of Alloys and Compounds 473 (2009) 87-93.

[139] B.-H. Liu, D.-M. Kim, K.-Y. Lee, J.-Y. Lee, J. Alloys Compd. 240 (1996) 214-218.

[140] K. Sakaki, H. Kim, H. Enoki, M. Hosono, S. Yoshimura, S. Ino, Y. Nakamura, J. Japan Inst. Met. Mater. 79 (2015) 257-264.

[141] G.H. Kim, S.G. Lee, K.Y. Lee, C.H. Chun, J.Y. Lee, Acta Metallurgica Et Materialia 43 (1995) 2233-2240.

[142] Y. Nakamura, K. Oguro, I. Uehara, E. Akiba, Int. J. of Hydrogen Energy 25 (2000) 531-537.

[143] Y. Nakamura, E. Akiba, J. Alloys Compd. 308 (2000) 309-318.

[144] P.H.L. Notten, J.L.C. Daams, R.E.F. Einerhand, J. Alloys Compd. 210 (1994) 233-241.

[145] T.N. Ramesh, P.V. Kamath, Mater. Res. Bull. 43 (2008) 2827-2832.

[146] K. Young, B. Reichman, M. Fetcenko, J. Alloy. Compd. 580 (2013) S349-S352.

[147] News available online. http://news.panasonic.com/press/news/official.data/data.dir/2014/02/en140213-3/en140213-3.html

[148] B. Pierozynski, International Journal of Electrochemical Science 6 (2011) 860-866.

[149] D. Fox, in an article “Power Struggle” available online. http://www.urbanfox.tv/articles/batteries/b1batteries.html

[150] K. Young, T. Ouchi, M.A. Fetcenko, US Patent 7,344,677 2008.

[151] M.A. Fetcenko, K. Young, S.R. Ovshinsky, T. Ouchi, US Patent 7,393,500, 2008.

[152] M.A. Fetcenko, S.R. Ovshinsky, B. Reichman, K. Young, C. Fierro, J. Koch, A. Zallen, W. Mays, T. Ouchi, J. Power Sources 165 (2007) 544-551.

[153] K. Young, T. Ouchi, B. Reichman, J. Koch, M. Fetcenko, J. Alloy. Compd. 509 (2011) 3995-4001.

[154] K. Young, T. Ouchi, B. Reichman, J. Koch, M. Fetcenko, J. Alloy. Compd. 509 (2011) 7611-7617.

[155] K. Young, T. Ouchi, B. Huang, B. Reichman, R. Blankenship, J. Alloy. Compd. 575 (2013) 65-72.

[156] K. Young, D. Wong, T. Ouchi, B. Huang, B. Reichman, Electrochimica Acta 174 (2015) 815-825.

[157] K. Young, M. Young, T. Ouchi, B. Reichman, M. Fetcenko, J. Power Sources 215 (2012) 279-287.

[158] D.F. Wong, K. Young, J. Nei, L. Wang, K.Y.S. Ng, J. Alloy. Compd. 647 (2015) 507-518.

ABSTRACT

COMPUTATIONAL MODELING OF HIGH-PERFORMANCE NICKEL-METAL HYDRIDE BATTERY MATERIALS

by

DIANA F. WONG

May 2016

Advisors: Dr. K.Y. Simon Ng & Dr. Kwo-Hsiung Young

Major: Chemical Engineering

Degree: Doctor of Philosophy

With 10 million hybrid electric vehicles on the road worldwide powered primarily by nickel-metal hydride (NiMH) batteries, research into this battery chemistry will improve the hybrid vehicle driving experience, extending electric-only driving ranges while reducing emissions and using less gasoline. The transfer, storage and transport of protons and electrons depend strongly on the structural and electrical features of the active material, including multiple phases, defects, and structural and compositional disorder. The contributions of such subtle defects and the difference with the bulk structure can be difficult to discern experimentally.

Ab initio calculations such as the ones based on density functional theory have been used to calculate properties and confirm ground state phase stability in AB_2 Laves phase alloys. First-principle DFT calculations confirmed a semi-empirical model for C14/C15 Laves phase structure determination for simple binary compounds, and extended the model for more ternary compounds, using the $Mg(Cu_{1-x}Zn_x)_2$ system, improving the resolution of the model.

Cycle stability of NiMH anode materials is strongly correlated to pressure-concentration-temperature isotherm hysteresis measurements, a measure of irreversible losses such as plastic

deformation upon hydrogenation and dehydrogenation, and alloy pulverization plays a key pathway for the degradation. First-principle DFT calculations modeled the initial hydrogenation of AB_5-type and AB_2-type alloys, yielding the initial lattice expansions upon hydrogenation, and correlating to the hysteresis trends, which can help guide the design of long-cycling materials.

X-ray diffraction patterns offer subtle but valuable markers that can be correlated to structure and electrochemical performance. Stacking faults direct interrupt (*h*0*l*) plane periodicity of nickel hydroxide materials, and through Rietveld refinement and DIFFaX modeling of the different types of stacking faults, the evolution of the stacking faults was tracked over precipitation time for different compositions. We determined which types of stacking faults have a stronger effect on the (101) peak, and the conditions that promote the formation of each type of stacking fault.

Electrochemical impedance spectroscopy coupled with equivalent circuit modeling probes the interactions that occur at the surface interfaces, yielding valuable electrical properties and electrochemical kinetics information. Low-temperature performance of NiMH batteries can be improved by dopants to AB_2 anode materials, and La and Nd are particularly promising additives that improve both the storage capacity and high-rate dischargeability. We determined the catalytic activity and the surface area contributions to the electrochemical reactions.

This study of defects, structural properties, and surface interfaces in battery materials can identify trends that contribute to higher capacity and higher power materials using computational and modeling methods. Understanding the trends provides better insight into how structural properties affect electrochemical processes and will help guide the design for better optimized battery materials.

AUTOBIOGRAPHICAL STATEMENT

EDUCATION

M.S., Chemical Engineering, Wayne State University, August 2015

B.S., Chemical Engineering, University of Michigan, May 2004

PUBLICATIONS

1. K. Young, J. Nei, **D. Wong**, L. Wang. “Structural, hydrogen storage, and electrochemical properties of Laves phase-related body-centered-cubic solid solution metal hydride alloys.” International Journal of Hydrogen Energy 39 (2014) 21489-21499.
2. K. Young, **D. Wong**, S. Yasuoka, J. Ishida, J. Nei, J. Koch. “Different failure modes for V-containing and V-free AB_2 metal hydride alloys.” J. Power Sources 251 (2014) 170-177.
3. **D. Wong**, K. Young, J. Nei, L. Wang, K. Ng. “Effects of Nd-addition on the structural, hydrogen storage, and electrochemical properties of C14 metal hydride alloys.” J. Alloy. Compd. 647 (2015) 507-518.
4. K. Young, T. Ouchi, L. Wang, **D. Wong**. “The effects of Al substitution on the phase abundance, structure and electrochemical performance of $La_{0.7}Mg_{0.3}Ni_{2.8}Co_{0.5-x}Al_x$ (x = 0, 0.1, 0.2) alloys.” J. Power Sources 279 (2015) 172-179.
5. K. Young, **D. Wong**, J. Nei, B. Reichman. “Electrochemical properties of hypo-stoichiometric Y-doped AB_2 metal hydride alloys at ultra-low temperature.” J. Alloy. Compd. 643 (2015) 17-27.
6. K. Young, **D. Wong**, T. Ouchi, B. Huang, B. Reichman. “Effects of La-addition to the structure, hydrogen storage, and electrochemical properties of C14 metal hydride alloys.” Electrochimica Acta 174 (2015) 815-825.
7. K. Young, **D. Wong**, L. Wang. “Effect of Ti/Cr content on the microstructures and hydrogen storage properties of Laves phase-related body-centered-cubic solid solution alloys.” J. Alloy. Compd. 622 (2015) 885-893.
8. K. Young, **D. Wong**, L. Wang, J. Nei, T. Ouchi, S. Yasuoka. “Mn in misch-metal based superlattice metal hydride alloy–Part 1 structural, hydrogen storage and electrochemical properties.” J. Power Sources 277 (2015) 426-432.
9. K. Young, **D. Wong**, J. Nei. “Effects of vanadium/nickel contents in Laves phase-related body-centered-cubic solid solution metal hydride alloys.” Batteries 1 (2015) 34-53.
10. **D. Wong**, K. Young, K. Ng. “First-principles study of structure, initial lattice expansion, and pressure-composition-temperature hysteresis for substituted $LaNi_5$ and $TiMn_2$ alloys.” Submitted to Comput. Mater. Sci.
11. **D. Wong**, K. Young, L. Wang, J. Nei, K. Ng. “Evolution of stacking faults in substituted nickel hydroxide spherical powders.” To be submitted to J. Power Sources.
12. **D. Wong**, K. Young, T. Ouchi, K. Ng. “First-principles point defect models for Zr_7Ni_{10} and Zr_2Ni_7 phases in nickel-metal hydride batteries.” To be submitted to Batteries.